

Antimicrobial Thin Films Via Aerosol Assisted Chemical Vapour Deposition

This thesis is submitted in partial fulfilment of the requirements for the Degree of Doctor of Engineering (Chemistry)



IMAN A. HASSAN

2016

Declaration

I, Iman Hassan confirm that the work presented in this thesis is my own. Where information has been derived from other sources, I confirm that this has been indicated in the thesis.

Abstract

This thesis focuses on the development of antimicrobial coatings through the use of aerosol assisted chemical vapour deposition (AACVD). The spread of nosocomial infections in healthcare settings can be attributed to contact between healthcare personnel and infected patients. Consequently, it can be proposed that the utilisation of antimicrobial surfaces may cause a decrease in hospital microbial contamination as well as enhancing infection-control.

Aerosol assisted chemical vapour deposition (AACVD) is used as the main deposition technique. It involves the formation of an aerosol through the dissolution of a precursor in a solvent and depends on solubility rather than the volatility of the precursors. A major advantage for AACVD is the ability to be an industrially scalable process and to deposit on a wide range of substrates including the commonly used materials on touch surfaces in hospitals such as stainless steel. This is an approach that offers a fast and easy route to the deposition of nanocomposite thin films.

Recently, much research has been invested into the preparation of these thin films, particularly for applications in antimicrobial coatings on surfaces. Moreover, it has been noted that the doping of metal oxide thin films with natural antimicrobial species can increase the antibacterial effectiveness.

During the course of this research project, the development of nanocomposite films based on copper, copper oxide, gallium oxide and zinc oxide was explored, with the aim of forming robust stable films with antimicrobial efficacy. The effectiveness of the antimicrobial films was investigated under lighting conditions found in hospital environments using serial dilution and viable colony counts. All experiments were carried out in duplicate and the number of survivors were determined by visible counting. Due to the high antimicrobial activity exhibited for copper, incorporating copper into metal oxides (gallium oxide and zinc oxide) were investigated in order to produce transparent films that will increased bactericidal activity.

The investigation examined the precursor delivery, effect of substrate temperature, solvent and additives on the CVD reactions. All of the films that were prepared were characterised using a number of techniques such as SEM/EDX, XRD, UV/Visible spectroscopy, XPS and XAS.

Acknowledgements

Firstly, I would like to thank my supervisor Prof. Claire J. Carmalt, for all of her encouragement, support and guidance over the years. I would like also to thank Dr. Sean Nair and Prof. Ivan Parkin for time taken to help and discuss this project.

I would like to take this opportunity to express my appreciation to everyone at UCL, Department of Chemistry and all of the members in the Carmalt and Parkin groups, past and present for the support, advice and many laughs. In particular: Davinder Bhachu, Ben Blackburn, Clair Chew, Tom Daley, Jared Henley, Caroline Knapp, Joe Manzi, Peter Marchand, Rushita Mehta, Sacha Noimark, Nuruzzaman Noor and Arnold Ratnasothy. I would like a special thanks to Sanjay Sathasivam for his support and being there whenever I needed help. Many thanks to Kevin Reeves for assistance with SEM imaging and Husn-Ubayda Islam for XAS measurements. I would like to thank all my colleagues at the Eastman Dental Institute, in particular, Annapaula Correia who trained me in microbiology and for her constant help.

I want to say a massive thank you to all my friends, in particular Maryam Alkizwini, Meetal Hirani, Anjum Khan, Joanna Korzeniewska, Bo Bo Liu, Leila Shariff and Vinitha Vijayakumar. Your support, encouragement and humour helped me through the highs and lows.

Extra special gratitude goes to my parents for their endless patience, love and encouragement. Thank you to my brothers and sisters for all your continuous support. This thesis would not have been possible without you.

Publications

List of publications associated with this thesis:

- 1) I. A. Hassan, I. P. Parkin, S. P. Nair, C. J. Carmalt, Antimicrobial activity of copper and copper(I) oxide thin films deposited *via* aerosol assisted CVD, *J. Mater. Chem. B*, **2014**, *2*, 2855-2860.
- 2) I. A. Hassan, A. Ratnasothy, D. S. Bhachu, S. Sathasivam C. J. Carmalt, 'The Effect of Solvent on the Morphology of Indium Oxide Deposited by Aerosol-assisted Chemical Vapour Deposition', *Aust. J. Chem.*, **2013**, *66*, *10*, 1274-1280.
- 3) P. Marchand, I. A. Hassan, I. P. Parkin, C. J. Carmalt, 'Aerosol – Assisted delivery of precursors for chemical vapour deposition: expanding the scope of CVD for materials fabrication, *Dalton Trans.*, **2013**, *42*, 9406 – 9422.

Contents

Declaration.....	ii
Abstract.....	iii
Acknowledgements.....	v
Publications.....	vi
Contents.....	vii
List of Figures.....	x
List of Tables.....	xiv
Abbreviations.....	xvi
Introduction.....	1
1.1 Nosocomial Infections.....	2
1.1.1 Types of HAI bacteria.....	4
1.2 Antibiotics.....	5
1.3 Spread of Infection.....	6
1.3.1 Levels of Contamination.....	9
1.3.2 Bacterial Adhesion.....	9
1.4 Antimicrobial surfaces.....	12
1.5 Project Aims.....	14
Experimental and Characterisation.....	15
2.1 Thin Film Deposition.....	16
2.2 Conventional CVD.....	17
2.3 Aerosol Assisted Chemical Vapour Deposition.....	19
2.4 Film Growth.....	23
2.4.1 Thin Film Growth models.....	24
2.4.2 Variations on CVD.....	25
2.4.3 Variations on AACVD.....	26

2. 5 Analytical Techniques	28
2.5.1 Powder X-ray Diffraction	28
2.5.2 Scanning Electron Microscopy	28
2.5.3 Cross-sectional SEM	29
2.5.4 Energy Dispersive X-ray	29
2.5.5 X-ray Photoelectron Spectroscopy	30
2.5.6 X-ray Absorption Spectroscopy	31
2.5.7 UV/Visible Spectroscopy	32
2.5.8 Band Gap Measurements	32
2.6 Microbiology Analysis	33
2.6.1 Viable Colony Counting Technique	33
2.6.2 Experimental Design	34
2.6.3 Microorganism Selection	35
2.6.4 Light Source	36
2.7 Antimicrobial Susceptibility Testing	37
2.7.1 Broth Dilution Test	37
2.8 Statistical Analysis	38
Copper and Copper(I) Oxide	39
3. Introduction	40
3.1 Copper vs Stainless Steel	40
3.1.1 Clinical Trials	41
3.1.2 Copper toxicity	43
3.1.3 Halo Effect	45
3.1.4 Copper Oxide	45
3.1.5 Deposition of copper	46
3.1.6 Susceptibility Testing of Copper Nanoparticles	48
3.2 Experimental	53
3.3 Results and Discussion	58
3.4 Antimicrobial Activity of Copper and Copper(I) Oxide	68
3.4.1 Results and Discussion	72
3.5 Conclusion	78

Indium Oxide and Gallium Oxide.....	79
4. Introduction.....	80
4.1 <i>Transparent Conducting Oxides</i>	80
4.1.1 <i>Band theory of solids</i>	81
4.1.2 <i>Indium oxide</i>	83
4.1.3 <i>In₂O₃ deposition</i>	83
4.1.4 <i>Gallium oxide</i>	83
4.1.5 <i>Ga₂O₃ deposition</i>	86
4.2 Experimental.....	88
4.3 Results and Discussion.....	95
4.4 Copper Gallium Oxide Thin Films.....	104
4.5 Antimicrobial activity of Ga ₂ O ₃ and Ga ₂ O ₃ -Cu ₂ O.....	112
4.6 Indium Oxide Thin Films.....	115
4.7 Conclusion.....	127
Zinc Oxide	128
5. Introduction.....	129
5.1 <i>Antimicrobial Activity of Zinc Oxide</i>	129
5.1.1 <i>Zinc Oxide Deposition</i>	130
5.2 Experimental.....	132
5.3 Results and Discussion.....	139
5.4 Antimicrobial Activity of ZnO and ZnO:Cu	163
5.5 Conclusion.....	166
Conclusion and Future Work	167
6. Conclusion	168
6.1 Future Work.....	171
References	172

List of Figures

Figure 1-1: Diagram illustrating the 5 moments where infections can be contracted.....	7
Figure 1-2: Diagram showing how infection can spread in a hospital.....	8
Figure 1-3: Diagram depicting the stages of biofilm growth.....	10
Figure 1-4: Flow chart showing how the spread of contamination can be reduced using antimicrobial surfaces.....	12
Figure 2-1: Schematic diagram of the CVD transportation and growth process...	18
Figure 2-2: Schematic diagram of the AACVD process.	20
Figure 2-3: Schematic diagram of the AACVD set up.....	21
Figure 2-4: Diagram of three film growth models that can be seen in thin films...	25
Figure 2-5: Example of the extrapolation of a Tauc plot to calculate the band gap measurements.	32
Figure 2-6: Diagram describing the steps involved in serial dilution.....	33
Figure 2-7: Diagram of the experimental set up of the humidity chamber.....	34
Figure 2-8: Diagram of the cell wall of gram positive and gram negative bacteria.	35
Figure 2-9: Spectra power distribution of general electric 28W Biax™ 2D lamp.	36
Figure 2-10: Diagram of the broth dilution set up using a micro-dilution dish for MIC and MBC detection.	37
Figure 3-1: Diagram illustrating the proposed events that occur during contact killing of copper against bacteria.....	45
Figure 3-2: Structural diagram of copper precursors a) $[Cu(hfac)_2]$, b) $[Cu(OCHCH_3CH_2NR_2)_2]$ and c) $[Cu\{(iPrN)_2CMe\}]_2$	46
Figure 3-3: Structural diagram of copper precursors investigated in this chapter a) $Cu(OAc)_2 \cdot H_2O$, b) $Cu(acac)_2$ and c) $Cu(NO_3)_2 \cdot 3H_2O$	47
Figure 3-4: Reaction scheme to show synthesis of tiopronin stabilised Cu NPs (From Ralph Leech's thesis).	49
Figure 3-5: Graph depicting the different stages in the growth cycle for bacteria.	51
Figure 3-6: Scheme diagram of reaction conditions using different precursors. ...	59
Figure 3-7: Powder XRD pattern of thin films deposited using copper acetate over a range of temperatures A) 350 °C, B) 400 °C, C) 450 °C in methanol and D) 400 °C in acetone with the Cu, Cu ₂ O and CuO XRD standards.....	60
Figure 3-8: Powder XRD of thin films deposited using $[Cu(acac)_2]$ in methanol at E) 350 °C, F) 400 °C, G) 450 °C and cooled under N ₂ and H) filmed cooled in air with the Cu, Cu ₂ O and CuO XRD standards.....	61
Figure 3-9: Powder XRD patterns of thin films deposited using $[Cu(NO_3)_2 \cdot 3H_2O]$ using I) methanol at 350 °C, J) ethanol at 350 °C and methanol at K) 400 °C and L)	

450 °C, M) methanol at 350 °C and cooled in air with the Cu, Cu ₂ O and CuO XRD standards.....	62
Figure 3-10: Thin films deposited using [Cu(NO ₃) ₂ .3H ₂ O] at 350 °C either cooled under N ₂ to form a) copper or cooled in air to form b) Cu ₂ O.....	64
Figure 3-11: Film growth model of a) Island growth and b) Particulate growth..	66
Figure 3-12: SEM micrograph of a) Cu film grown via AACVD of [Cu(NO ₃) ₂ .3H ₂ O] in methanol at 350 °C and cooled under N ₂ (Reaction I), b) Cu ₂ O film deposited from [Cu(NO ₃) ₂ .3H ₂ O] in methanol at 350 °C and cooled in air (Reaction M). Side-on SEM of the c) Cu film and d) Cu ₂ O film.....	67
Figure 3-13: Viable colony counts of bacteria after incubation on Cu thin films tested against a) E. coli, b) S. aureus and viable counts of bacteria of Cu ₂ O against c) E. coli and d) S. aureus.....	69
Figure 3-14: Viable counts of bacteria after incubation on Cu and Cu ₂ O thin films tested three times over 7 days. a) Cu and b) Cu ₂ O were tested against S. aureus (1 h incubation). c) Cu and d) Cu ₂ O against E. coli (30 min or 1 h incubation respectively). The glass control tested against e) E. coli and f) S. aureus (1 h incubation).....	71
Figure 3-15: Diagram showing the difference in growth between bacteriostatic and bactericidal antimicrobial agents.....	73
Figure 3-16: Growth curve of E. coli cells grown with differing concentrations of Cu NPs.....	76
Figure 3-17: Growth curve of S. aureus cells grown with differing concentrations of Cu NPs.....	77
Figure 4-1: Energy band theory for solids.....	82
Figure 4-2: Doping of n-type and p-type semiconductors.....	82
Figure 4-3: Structural diagram of a) M(CH ₃) ₃ , b) ethylene glycol and c) diethylene glycol.....	87
Figure 4-4: Aerosol-assisted CVD reactions to deposit gallium oxide films.....	96
Figure 4-5: XRD pattern of crystalline Ga ₂ O ₃ film (black) deposited using GaMe ₃ and MeOH at 450 °C and annealed with standard reference Ga ₂ O ₃ XRD pattern (red).....	99
Figure 4-6: SEM images of Ga ₂ O ₃ deposited using reactions:.....	101
Figure 4-7: Side-on SEM of amorphous Ga ₂ O ₃ thin films.....	102
Figure 4-8: XPS spectra of a) Ga 3d and b) Ga 2p peaks from the surface of the amorphous Ga ₂ O ₃ films.....	103
Figure 4-9: XRD pattern of crystalline copper gallium oxide film with standard patterns of Ga ₂ O ₃ and CuO.....	105
Figure 4-10: XPS spectra of a) Ga 3d, b) Ga 2p and c) Cu 2p peaks from the surface of the amorphous copper gallium oxide films.....	107
Figure 4-11: Normalised copper K-edge XANES spectra for Cu metal foil, Cu, Cu ₂ O and Ga ₂ O ₃ -Cu ₂ O thin film sample. b) K ³ -weighted χ(k) spectra Ga ₂ O ₃ -Cu ₂ O and theoretical fit. c) Fourier transform of EXAFS of the χ(k).....	110

Figure 4-12: SEM and side-on SEM images of amorphous Ga ₂ O ₃ -Cu ₂ O thin film.	111
Figure 4-13: Viable counts of bacteria after incubation on Ga ₂ O ₃ and Ga ₂ O ₃ -Cu ₂ O thin films tested against a) <i>E. coli</i> and b) <i>S. aureus</i> .	113
Figure 4-14: AACVD reaction to deposited indium oxide films.	116
Figure 4-15: XRD patterns obtained for In ₂ O ₃ films deposited by AACVD from the in situ reaction of InMe ₃ /HOCH ₂ CH ₂ OH in MeOH at temperatures between 400 – 500 °C.	116
Figure 4-16: XRD patterns obtained for In ₂ O ₃ films deposited by AACVD from the in situ reaction of InMe ₃ /HOCH ₂ CH ₂ NMe ₂ in MeOH at temperatures between 350 – 500 °C.	118
Figure 4-17: XRD patterns obtained for In ₂ O ₃ films deposited by AACVD from the in situ reaction of InMe ₃ /MeOH at temperatures between 350 – 500 °C.	119
Figure 4-18: SEM images of films grown from InMe ₃ /MeOH at a) 400 °C, b) 450 °C, and c) 500 °C, d) Film grown from InMe ₃ /HOCH ₂ CH ₂ OH in MeOH at 450 °C and e) film grown from InMe ₃ /HOCH ₂ CH ₂ NMe ₂ in MeOH at 450 °C.	121
Figure 4-19: Side-on SEM images of films grown at 450 °C from a) InMe ₃ /HOCH ₂ CH ₂ NMe ₂ in MeOH and b) InMe ₃ /MeOH.	122
Figure 5-1: Structural diagram of zinc precursors used in this investigation.	131
Figure 5-2: XRD patterns of thin films deposited from Zn(NO ₃) ₂ ·6H ₂ O at 450 °C with a) [Cu(NO ₃) ₂ ·3H ₂ O] and b) Cu(acac) ₂ .	141
Figure 5-3: XRD patterns of thin films deposited using [Zn(OAc) ₂ ·2H ₂ O] with either a) [Cu(NO ₃) ₂ ·3H ₂ O/MeOH], b) [Cu(acac) ₂ /acetone] and c) [Cu(acac) ₂ /MeOH].	142
Figure 5-4: XRD patterns of thin films deposited from Zn(OAc) ₂ /Cu(acac) ₂ with the addition of a) CTAB (low concentration), b) CTAB (high concentration) and c) HOCH ₂ CH ₂ OMe.	143
Figure 5-5: Diagram of dual source AACVD.	145
Figure 5-6: Schematic diagram of Dual Source AACVD used in this investigation.	146
Figure 5-7: XRD patterns obtained from AACVD at a) 350 °C, b) 450 °C and Dual source AACVD at c) 350 °C and d) 450 °C.	147
Figure 5-8: XRD patterns obtained from dual source AACVD depositions carried out at 350 °C for ZnO and 1 – 8 mol% ZnO:Cu.	148
Figure 5-9: Photos of ZnO:Cu thin films deposited using dual source AACVD at a) 350 °C, b) 400 °C and c) 450 °C.	149
Figure 5-10: XRD patterns obtained from dual source AACVD depositions carried out at 400 °C for ZnO and 1 – 4 mol% ZnO:Cu.	150
Figure 5-11: XRD patterns obtained from dual source AACVD depositions carried out at 450 °C for ZnO and 1 – 8 mol% ZnO:Cu.	152
Figure 5-12: XRD patterns obtained from dual source AACVD depositions carried out at 350 °C for 10 – 18 mol% Cu films.	153

Figure 5-13: a) Optical transmission spectrum taken against an air background showing ZnO and 1 – 18 mol% ZnO:Cu thin films, b) UV/Visible absorbance spectrum for ZnO and 1 - 18 mol% ZnO:Cu films.	155
Figure 5-14: SEM images of a) ZnO and ZnO:Cu films b) 1 mol% Cu, c) 2 mol% Cu, d) 4 mol% Cu, e) 8 mol% Cu and f) 10 mol% Cu.	157
Figure 5-15: XPS for ZnO:Cu thin films of Zn 2p and Cu 2p for a) 2 mol%, b) 4 mol% and c) 8 mol%.	160
Figure 5-16: Normalised copper K-edge XANES spectra for Cu, Cu ₂ O, CuO and the ZnO:Cu thin film sample.	162
Figure 5-17: Viable counts of bacteria after incubation on ZnO, ZnO:Cu thin films and glass control tested against <i>E. coli</i> for a) 3 hours, b) 6 hours and c) 18 hours. (L+ = illuminated and L- = not illuminated (in the dark)).	165

List of Tables

Table 2-1: List of bacterial strains used in this thesis and their cell wall type.	35
Table 2-2: Asterisks system to define the statistical significance.	38
Table 3-1: The results of using a variety of copper precursors, solvents, temperature and cooling gas.	58
Table 3-2: Lattice parameter calculations of Cu and Cu ₂ O.	66
Table 3-3: Results from copper and copper oxide against a range of activity from previous investigations.	70
Table 3-4: Minimum inhibitory and bactericidal concentrations for copper and copper oxide nanoparticles against gram positive and gram negative bacteria strains.	73
Table 3-5: Table of MBC values of copper and copper oxide NPs from previous investigations.	74
Table 3-6: Generation time calculated during the log phase for the E. coli growth curve.	76
Table 4-1: Experimental conditions and resultant films deposited.	95
Table 4-2: EDX measurements taken from the amorphous copper gallium oxide film.	105
Table 4-3: Linear combination analysis (LCA) of XANES fit for amorphous Ga ₂ O ₃ -Cu ₂ O film.	109
Table 4-4: Experimental conditions and resultant characterisation for In ₂ O ₃ films deposited.	119
Table 4-5: Texture coefficient intensity ratio for XRD peaks obtained from films deposited from InMe ₃ /MeOH.	123
Table 4-6: Texture coefficient intensity ratio for XRD peaks obtained from In ₂ O ₃ films deposited using a diol or donor functionalised alcohol at 450 °C.	124
Table 4-7: Electrical properties of films grown from InMe ₃ /HOCH ₂ CH ₂ NMe ₂ in MeOH and InMe ₃ /MeOH at 450 °C.	126
Table 5-1: The results of using a variety of zinc and copper precursors and solvents.	139
Table 5-2: Texture coefficient intensity ratio for XRD peaks obtained from films deposited from Zn(OAc) ₂ /Cu(acac) ₂ with a) CTAB (low conc), b) CTAB (high conc) and c) HOCH ₂ CH ₂ OMe.	144
Table 5-3: Texture coefficient intensity ratio for XRD peaks obtained from films deposited using dual source AACVD at 350 °C.	148
Table 5-4: Texture coefficient intensity ratio for XRD peaks obtained from films deposited using dual source AACVD at 400 °C.	150
Table 5-5: Texture coefficient intensity ratio for XRD peaks obtained from films deposited using dual source AACVD at 450 °C.	151
Table 5-6: Band gap measurements calculated using a Tauc plot.	155

Table 5-7: EDX measurements taken from the ZnO:Cu thin films.....158
Table 6-1: Antimicrobial activity results of thin films deposited discussed in this
thesis.....169

Abbreviations

AACVD	Aerosol Assisted Chemical Vapour Deposition
ALD	Atomic Layer Deposition
CDC	Centers for Disease Control and Prevention
CFU	Colony Forming Units
CVD	Chemical Vapour Deposition
DNA	Deoxyribonucleic acid
EDX	Energy Dispersive X-ray Spectroscopy
FDA	Food and Drug Administration
HAI	Hospital Acquired Infections
ICU	Intensive Care Units
IV	Intravenous
MBC	Minimum Bacterial Concentration
MDR	Multi-Drug Resistant
MIC	Minimum Inhibitory Concentration
MRSA	Methicillin Resistant Staphylococcus Aureus
NP	Nanoparticle
PBS	Phosphate Buffered Saline
PVD	Physical Vapour Deposition
ROS	Reactive Oxygen Species
SEM	Scanning Electron Microscopy
UTI	Urinary Tract Infections
UV/Visible	Ultraviolet-Visible Spectroscopy
WHO	World Health Organization
XANES	X-ray Absorption Near Edge Structure
XAS	X-ray Absorption Spectroscopy
XPS	X-ray Photoelectron Spectroscopy
XRD	X-ray Diffraction

1

Introduction

The following is an introductory chapter to the thesis. This will provide the reader with background into the aim of this investigation and the contribution of touch surfaces to the spread of infections in a hospital environments as well as the impact of multi-drug resistant bacteria.

1.1 Nosocomial Infections

There is a great interest in the epidemiology of Hospital Acquired Infections (HAI), which has become a major problem for hospitals and healthcare institutions worldwide. HAI are also known as nosocomial infections that are described as infections acquired during hospital care, which were not present at the time of admission. Infections that occur 48 hours after being discharged (up to 4 weeks) are also included.^{1,2}

Nosocomial infections can also be considered endemic or epidemic, where endemic infections are more frequent. Epidemic infections are described as the unusual increase of specific infections and usually occur during an outbreak.¹ Many different variables facilitate the spread of nosocomial infections including patient care practise and the hospital environment.

Statistics have shown that 1 in 10 patients who are admitted to a UK hospital contract a HAI, which accounts for 300, 000 cases a year and costs the NHS approximately £1 billion annually.³ Similar figures are also seen in the United States where nosocomial infections were reported as one of the top ten leading causes of death. An estimated that 2 million infections contributes to 100, 000 deaths annually.⁴ The Centers for Disease Control and Prevention (CDC) has estimated that 1 in 20 hospitalised patients contract nosocomial infections costing US hospitals over \$30 billion.⁵

The rise of HAI has become a progressively more important issue globally due to the increase in mortality rates, medical costs and length of stay. The World Health Organization (WHO) carried out a survey that involved 55 countries and indicated that approximately 8.7% of patients contract an HAI meaning that over 1.4 million people in the world suffer from these infections.^{6,7}

HAI are on the rise and cause major complication for hospitals due to the infections associated with increasing invasive surgeries and medical devices. Nosocomial infections also present a heavy financial and resource burden for hospitals and healthcare institutions, resulting in prolonged hospital duration, patient discomfort, and in some cases death.

There is a large distribution of the different types of nosocomial infection sites.

The most common nosocomial infections sites are:

- Surgical site infections – described as any kind of discharge or abscess at the surgical site within a month after the operation. During the process of wound dressing, cross contamination can occur by either contaminated hands or instruments. Infection rates can range between 0.5 – 15% depending on the type of surgery.⁸
- Urinary tract infections (UTI) – occurs due to the cross contamination of microbes. This is the most common type of infection accounting for 40% of HAIs. Approximately 80% of UTIs are associated with catheters. Infections are usually identified with urine culture being taken, with or without symptoms showing.⁹⁻¹¹
- Respiratory pneumonia – commonly occurs to patients in the intensive care unit (ICU) with a rate of 3% per day. Patients placed on ventilation are prone to infection due to cross contamination when handling and maintaining the ventilator instruments and associated devices.^{4,12,13}
- Bloodstream infections – the second most common type of infection causing the failure of the immune system. It has been reported that 35% of mortalities associated with nosocomial infections are attributed to bloodstream infections. These also increase hospital duration to 24 days that leads to an economic loss of approximately \$40, 000 per patient.¹⁴⁻¹⁶

There are two major causes of nosocomial infections:

- Long term, irrational and irresponsible use of antimicrobial agents leading to the development of resistant bacterial strains.
- The quality and maintenance of sterile conditions in the hospital.

1.1.1 Types of HAI bacteria

There are many different types of nosocomial infecting bacteria that someone can contract at a hospital. The CDC described *S. aureus* and *E. coli* as two of the most common bacteria that cause HAI and these are the two types of microorganisms that are used in this investigation.

- *Staphylococcus aureus (S. aureus)*

S. aureus is a gram positive bacterium that appears under a microscope as spherical organisms grouped together and is commonly found in the anterior nostrils of around one-third of the population.^{17,18} It can also have the ability to spread to other areas causing infections in wounds and the bloodstream (septicaemia), which could cause disseminated diseases.¹⁹

In the 1950s, antibiotic Methicillin was developed and was effective against *S. aureus* however by the 1960s, *S. aureus* strains were seen to be resistant to methicillin.²⁰ *Methicillin resistant staphylococcus aureus* (MRSA) is resistant to the β -Lactam group found in antibiotics that greatly reduces the antibiotics available for treatment.^{21,22} MRSA is found to be commonly transmitted between patients and healthcare workers. This can lead to spread of infections via contaminated hands that can spread and colonise on the floor, bedframe, and lockers.

- *Escherichia coli (E. coli)*

E. coli is a gram negative bacterium that appears rod shaped under a microscope. It is one of the most commonly studied microorganisms in microbiology. *E. coli* is one of the leading causes of bloodstream infections in the USA. *E. coli* accounts for approximately 22% of mortality rate for HAIs and can frequently be found in the gastrointestinal tract of humans and many animals.^{23,24}

1.2 Antibiotics

Antibiotics are a substance that kills or inhibits the growth of microorganisms and have been described as a 'miracle drug' that revolutionised the medical field. The first antibiotic, Penicillin was discovered accidentally in the late 1920s.^{25,26} As time went on, an increase in knowledge saw new antibiotics develop at a fast rate. The next big discovery was Streptomycin in 1943²⁷ and with improvement in hospital hygiene it was thought to be the end of infectious diseases as the mortality rates decreased. Alexander Fleming predicted in his Nobel lecture in 1945 that the misuse of antibiotics will lead to antibiotic resistance. However, at that moment, the rate of antibiotic development was faster than bacterial resistance.^{28,29}

The rate of antibiotic resistance bacteria has become untreatable and uncontrollable. There is also a lack of antibiotics development with the majority of antibiotics discovered decades ago and the last antibiotics developed were in 1987. This is creating worrying situation which could potentially see a return to the pre-antibiotic era.³⁰⁻³²

The rise of multi-drug resistance (MDR) bacteria strains, such as MRSA and the reliance on antibiotics has led to the survival and maintenance of MDR and is seen as an integral part of the nosocomial infection problem.

The emergence and rise in bacterial drug-resistance and lack of development in novel antimicrobial agents, threatens the effectiveness of medical treatments. This is a global problem that requires actions to be taken across all governments and societies.³³

MDR strains of bacteria occur due to the natural evolutionary concepts. This phenomenon occurs when microorganisms duplicate erroneously or possess resistant genes that can be exchanged consequently, allowing these resistant microorganisms to grow and replicate, transferring their resistant genes to a larger population resulting in an increase in MDR bacteria strains.^{34,35}

A new report released at the end of 2014, looking at the future of antimicrobial resistance predicted what would happen between now and 2050 if nothing is

done. It predicts a bleak future resulting in over 100 million premature deaths globally by 2050. One of the reasons the report stated was the massive underinvestment into antibiotic research.^{36,37}

1.3 Spread of Infection

Surfaces surrounding patients are frequently saturated with bacterial microorganisms. A commonly touched item can act as significant reservoirs of microbes. Semmelweis in 1846 described the importance of clean hands in the prevention of infections. He noticed a higher mortality rate of women when physicians delivered their children when compared to deliveries carried out by midwives. The difference was observed to be due to the physicians studying autopsies before attending to patients and not washing their hands, which allowed the transfer of infection to the women in labour. Semmelweis proposed that all examiners should clean their hands with carboxylic acid before treating patients. This reduced the childhood mortality rate from 11.4 to 1.8% in 2 years. Frequently touched surfaces in the hospital environment are referred to as 'hand-touch surfaces' such as bed-frames, door handles, toilet seats, bedside tables, and toilet rails.³⁸⁻⁴¹

In 2004, the NHS National Patient Safety Agency launched a nationwide the 'cleanyourhands' campaign in order to improve hand hygiene to reduce the incidences of HAIs. The aim of the campaign was to educate, prompt, and enable healthcare workers to clean their hands at the right time, while treating patients with the use of soap and water or alcohol hand rub.^{42,43} It is recommended by the WHO that healthcare workers should decontaminate their hands before and after treating a patient, after any exposure to bodily fluids, and before any aseptic procedures (Fig. 1-1).^{44,45}



Figure 1-1: Diagram illustrating the 5 moments where infections can be contracted.

The process of cleaning reduces the microbial loads and any nutrients that microorganisms can feed on to grow. The cleaning can assist in the breakdown of the cycle of infection transmission in the healthcare institution. Statistics have shown that regular cleaning of hospital surfaces with detergent can reduce transmission of nosocomial infections by 40% but out sourcing of contracts and budget limitations has caused some decrease in cleaning frequency.^{46,47}

The management of healthcare related waste is an important part of maintaining the hospital hygiene and controlling infections. Like surfaces, hospital waste can be considered a reservoir of infectious bacterial organisms. If this waste is inadequately disposed of, it can contribute to the spread of infections. The main sources of infections are healthcare workers, the patients, and the hospital environment.^{48,49}

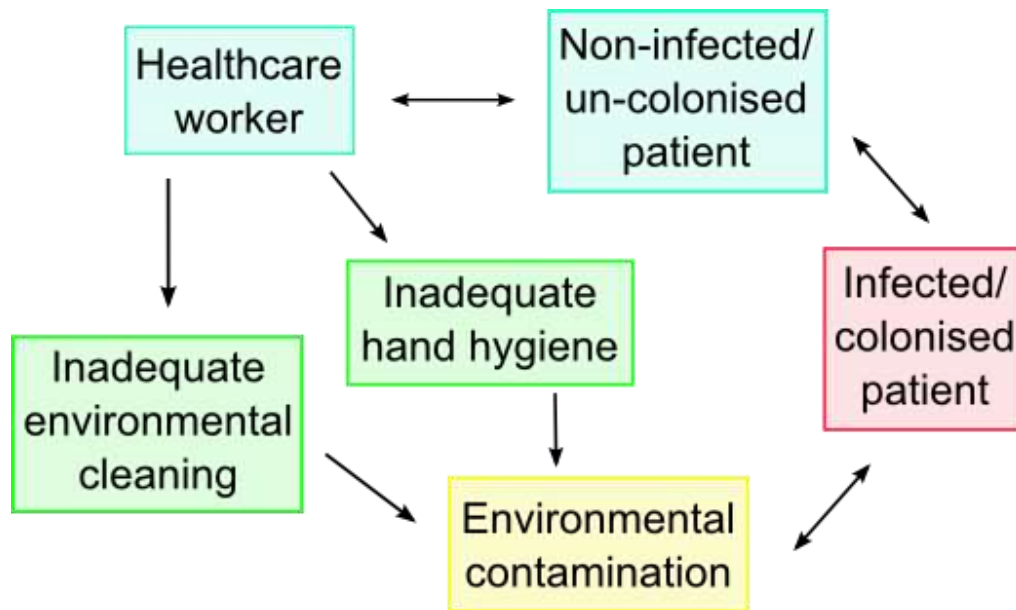


Figure 1-2: Diagram showing how infection can spread in a hospital.

The healthcare environment can be contaminated with pathogens that can cause an outbreak without proper cleaning procedures. Hospital workers can be colonised or infected and can become a symptomless carrier. This can lead to infecting patients and contaminating other hospital environments. The source that contributes most to hospital epidemics is infected patients. Colonised patients contaminate their surrounding environment, which can lead to contamination of other patients and healthcare workers.⁵⁰⁻⁵² Fig. 1-2 shows the flow diagram of how infections can spread.

Organised and frequent cleaning can efficiently remove bacterial contamination from hospital surfaces. Research has shown that hospital surfaces are not adequately cleaned and are re-contaminated very quickly. One of the most effective ways of preventing the spread of infections is the basic maintenance of hygiene in the hospital environment. The effect cleaning has is mechanical whereby the microorganisms are removed from the surface by being suspended in cleaning fluid. This can remove approximately 90% of microorganisms.^{1,53}

1.3.1 Levels of Contamination

It is difficult to quantify and measure the minimum level of contamination needed on a surface to initially colonise a patient that can lead to an infection. Nosocomial infecting bacteria has the ability to survive for days to months on hospital surfaces even with cleaning procedures in place to reduce the level of microbial burden. Some research has suggested that the level of contamination of surfaces should be below 250 cfu per 100 cm² to minimise the transmission of infections and within the limits that are safe for patient care. However, the rapid re-contamination of pathogens on these touch-surfaces in the hospital after cleaning is of major concern.

The best results observed have been a routine that involves cleaning and disinfecting the hospital environment at regular intervals. This will increase the already full work load for understaffed healthcare workers.⁵⁴

1.3.2 Bacterial Adhesion

Bacteria can exist as planktonic where they drift in great number in a solution or part of biofilm community. Biofilms are a vital structure for microorganisms composed of various biomolecules such as proteins, lipids and water.⁵⁵ The microorganism self-assembles the microbial structure and is capable of optimising the conditions. Surfaces can act as a microbial habitat due to their ability to adsorb nutrients and provide a surface for microbes to be attached. Biofilms act as functional communities where the matrix can trap nutrients for microbial growth and help prevent detachment of cells from the surface.⁵⁶

Biofilm development is a major problem for healthcare institutions due to the contamination of medical devices. Biofilms can also be a problem for water supply and oil extraction where the pipes can be damaged, corroded or contaminated.⁵⁷⁻

60

In 1847, Antoine van Leeuwenhoek used effective but primitive microscope observation of aggregation of 'animalcules' (little animals) that were scraped from the surface of a human tooth.⁶¹ This would be the first documentation of biofilms. As technology and investigations developed, researchers have observed that bacteria grow differently once adhered to a surface.⁶²

Planktonic microbial cells are transported in solution and are attached to a particular surface. If the environmental factors (available energy, orientation, temperature, pressure) are favourable the bacteria can attach to the surface either by attractive and repulsive forces such as electrostatics and/or Van der Waal's forces that are described in the DVLO (Derjaguin, Verwey, Landau and Overbeek) theory.⁶³⁻⁶⁵ At this stage, the attachment of the bacteria is irreversible due to the process of cell adhesion. Colonisation, growth and division of the bacteria occur and can take hours to days. The biofilm matures and grows consisting of attached islands of bacteria with water channels running through it, Fig. 1-3.

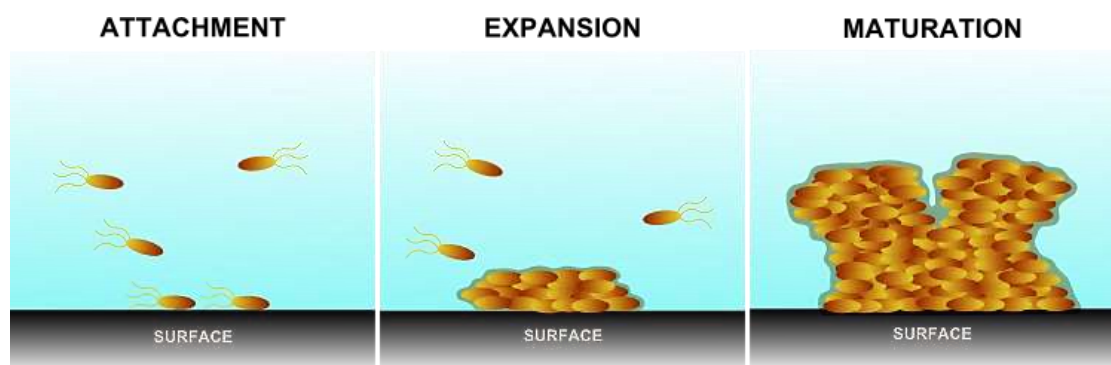


Figure 1-3: *Diagram depicting the stages of biofilm growth.*

The formation of biofilms on various industrial and biomedical surfaces is a problem. Mature biofilms are persistent and can develop a tolerance to cleaning products such as disinfectants. Controlling the bacterial adhesion and stopping the initial stages of biofilm formation can control the development of biofilm.

There are many advantages for microbes to attach and form biofilms, which include:

- Enhanced resistance to antibiotics and a variety of antimicrobial agents. The resistance can be from the polymeric matrix enclosing the community of microorganism which hinders the penetration of any antibacterial agents. The biofilm can provide a protective matrix that is mainly made up of polysaccharides, which allows the structure to be kept in place and not be swept away. The matrix can also prevent toxic molecules such as antibiotics and disinfectants due to its ability to an ion exchanger.⁶⁶
- Development of the matrix allows for optimised conditions for growth. The microorganisms have the nutrients and moisture to grow making it advantageous for newly attached planktonic bacteria to become a part of the community. The biofilm structure consists of pores, which act as water channels that allows for the transport of nutrients.⁶⁶
- A genetic factor can also increase the resistance due to the cell-to-cell signalling and communication that can lead to the production of vital genes that favour the maintenance of the microorganisms. Biofilms have the enhanced ability to adapt to hostile conditions and environments due to their structure. The bacterial cells are in close proximity to each other, which allows for opportunities to exchange genetic material. This cell-to-cell communication (quorum sensing) can allow for further resistance to antibacterial agents.⁶⁶⁻⁶⁸

There are two types of strategies for combating the formation of biofilms. One approach is the antimicrobial surface that prevents microbes adhering to the surface for example superhydrophobic films^{69,70} or the development of other surfaces that kill approaching microbes.^{9,71}

1.4 Antimicrobial surfaces

Hospitals are undergoing stewardship programmes to manage the over-prescription and mishandling of antibiotics. With the rapid increase of MDR bacterial strains and the lack of new antibiotics, there is a need to preserve the availability of existing antibiotics. Different approaches are needed to tackle this problem.

Cleaning procedures can help reduce the spread of infection, however there is a need to remove the surface, which acts as a microbial reservoir. Most strategies focus on the transfer of microbes, which is important, or development of antibiotics that can treat HAI. There is a need to remove the bacterial reservoirs. A preventable approach to reduce bacterial infections involves the use of self-cleaning surfaces. Figure 1-4 shows how antimicrobial surfaces can break the cycle in the spread of infections.⁷²

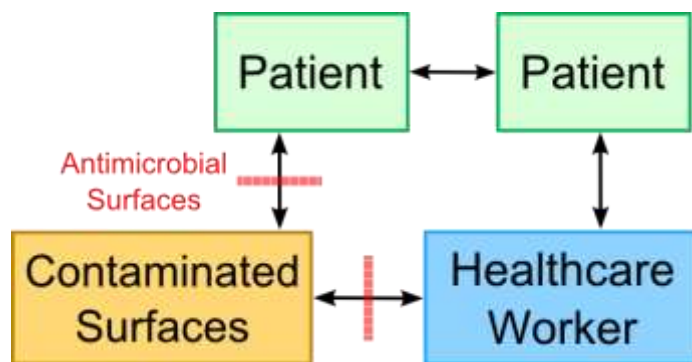


Figure 1-4: Flow chart showing how the spread of contamination can be reduced using antimicrobial surfaces.

The longer a nosocomial pathogen persists on a surface, the longer it may be a source for transmission to a susceptible patient or healthcare worker. Frequently touch surfaces such as doorknobs, push plates, bed rails and poles have been identified as reservoirs for the spread of pathogens microbes which can easily contaminate hands and equipment of healthcare workers, who, in turn can transmit these pathogens to patients during routine care. Coating these touch surfaces with antimicrobial agents can potentially reduce infection rates.

Due to bacterial infections on medical devices and surfaces, there are a number of strategies employed to reduce this problem in order to prevent the formation of biofilms on the surface.⁷³ The topological and chemical characteristic of the surface can play a role in how well microbes can attach to the surface. There are different ways antimicrobial coatings can prevent the formation of biofilms. An antiadhesive coating that can be applied to act as a repellent to contaminations that are usually in the form of physiological fluids. This can prevent electrostatic interactions described in the DLVO theory. This can be obtained by chemically modifying surfaces or building nanostructure on that surface.⁷⁴

The use of bioactive compounds with natural antimicrobial properties are often used. These material do not need any modification to exhibit antibacterial action. Copper and silver are known antibacterial agents used throughout history.⁷⁵ Their effectiveness as compounds and dissolved ions have been investigated⁷⁶⁻⁷⁸. Coatings or devices containing these metals/nanoparticles are prominent.⁷⁹ In this thesis, copper is investigated and is discussed further in chapter 3. Other metals discussed in this thesis are gallium (chapter 4) and zinc (chapter 5).

1.5 Project Aims

The purpose of this work is to study metal oxide antimicrobial thin films deposited by aerosol assisted chemical vapour deposition. The properties will be assessed for their potential as antimicrobial surface coatings. The ultimate goal is to produce materials which exhibit antimicrobial effectiveness for the use in reducing the spread of nosocomial infections in a hospital environment.

2

Experimental and Characterisation

The chapter describes the experimental methods used to deposit coatings by Aerosol Assisted Chemical Vapour Deposition and the theory behind the analytical techniques used to characterise the films. The main analytical techniques this chapter concentrates on are X-ray diffraction (XRD), scanning electron microscopy (SEM) and X-ray photoelectron spectroscopy (XPS). The microbiological analysis carried out (serial dilution and susceptibility testing) on the film is also discussed.

2.1 Thin Film Deposition

Thin films can be described as a solid layer of material deposited on a substrate that give an enhanced representation of the bulk material. Thin films can vary in thickness and can give heightened surface properties. There are a wide range of methods of forming thin films. Some of the most popular are Chemical Vapour Deposition (CVD), Physical Vapour Deposition (PVD) and Atomic Layer Deposition (ALD). Choosing a deposition technique depends on the properties that the thin film is required to possess and the availability of precursors.

CVD is a versatile technique used for depositing gas phase reactants (precursors) onto a solid substrate creating thin films. CVD can be used to deposit films on to large areas, for example glass/steel and small scale coatings.^{80,81}

PVD is a technique that involves deposition via atoms/ions in a gas phase. This process involves sputtering and evaporation. It is known as a line of sight technique which causes the coating to appear only where the atomic beam can 'see' it, causing minimal surface reactions. The atoms will cover the top of the substrate but not the side of the walls. This does not produce conformal coverage and can come at a high cost. The difference between CVD and PVD is how the precursors are delivered. In CVD thin films grow by using gas phase precursors that adhere to the substrate. However, PVD grows thin films by using sputtered or evaporated atoms usually under high vacuum conditions. CVD is the opposite of PVD whereby it is not a line of sight method therefore it can produce films that have conformal coverage. During a CVD process the atoms have the ability to move freely across the substrate, which results in uniform coverage that follows surface contours.⁸²

ALD is similar to CVD as it forms uniform and conformal thin films however, ALD is based on films being built up by layer-by-layer growth. At first the surface is exposed to gaseous reactants which are chemisorbed to the surface until it is saturated. The excess precursor vapour is purged and a second precursor is allowed to react with the surface, then the excess gas is pumped away. The

sequence can be repeated so as to increase the thickness of the film. It can have very slow growth rate (monolayer growth).⁸³

Even though ALD is a variation on CVD, there are some major differences. The precursors are much more reactive in ALD when compared to CVD. Precursors in ALD react separately with the substrate, whereas in CVD the precursors can react together in the gas phase and on the surface. Precursor concentration is not needed in ALD as it is dependent on the surface type.

2.2 Conventional CVD

Chemical Vapour Deposition (CVD) involves the formation of a thin solid of material on a substrate created by a chemical reaction using volatile precursors transported in a carrier gas.

The first type of CVD process recorded was by John Howarth who produced a pigment called 'carbon black'.⁸⁴ Around the 1800s industries saw CVD processes as being economically viable for extraction. However, in the past 40 years, there has been a strong interest in its fundamental understanding. There was increased effort into discovering the scientific and technological process behind CVD and incorporating that into a wide range of applications. This was due to the change of focus on extraction to deposition allowing CVD to become a more important technique.⁸⁰

The CVD process involves a sequence of reactions that can occur in the gas phase or on the surface. It involves a chemical reaction of gaseous atoms with an activated environment that can initiate the reaction. This can be heat, light or plasma conditions. There is an inert carrier gas such as nitrogen that allows for easy transport of the precursor to the substrate. This is followed by the formation of a stable solid material, within the reaction chamber.

The deposition process involves a heterogeneous reaction in the gas phase near the heated substrate. The process starts by the transport of precursors into the

reactor, which allows for weak physisorption of precursors on to the surface (Fig. 2-1). Decomposition occurs and it generates atoms and unwanted by-products onto the surface. There is a mass transport of atoms across the surface allowing for adsorption of atoms. The nucleation of the atoms leads to film growth. There is desorption and migration of the remaining fragments.

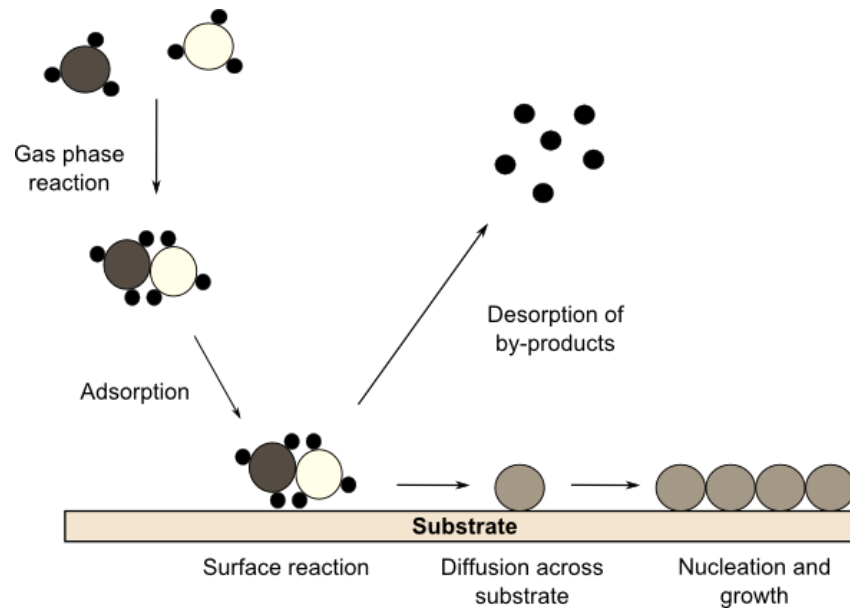


Figure 2-1: Schematic diagram of the CVD transportation and growth process.

The fabrication of thin films by CVD allows highly reproducible uniform films and composition control with excellent conformal coverage. This technique is able to deposit films that are highly pure and dense as well as being adherent and inexpensive. The CVD technique has the capability to control crystal structure, surface morphology and orientation by adjusting the CVD process parameters such as deposition rates and temperatures. Moreover, the rate of deposition can be tuned, allowing for a finer control over the thickness of the film produced.

There are also a number of drawbacks that can hinder the applications of CVD. This includes chemical and safety hazards that can be encountered when using toxic, flammable or corrosive precursor gases. There can also be a challenge in

forming multicomponent materials when using multi-source precursors as it can be difficult to control the stoichiometry of the resultant thin film. Therefore there are concerns when utilizing the CVD technique when it comes to the selection of the precursors, as it can have an effect on the growth rate, electrical properties, and transparency of the film.

2.3 Aerosol Assisted Chemical Vapour Deposition

Aerosol assisted chemical vapour deposition (AACVD) is a variation on the conventional CVD process. This method involves the precursor being dissolved in a solvent in order to form an aerosol. The formation of an aerosol is generated by ultrasonic humidifier (nebulizer) forming aerosol droplets creating a precursor mist (Fig. 2-2). This mist is transported to the CVD reactor via a carrier gas. This mist evaporates once it enters the chamber due to the increase in temperature causing the precursor to be in its gaseous state, where decomposition occurs. There is a need for the carrier gas to have enough pressure to be able to transport the aerosol to the CVD reactor. As a result, the optimal flow rate for the system has to be established allowing a high deposition rate due to the high mass transport of precursor to the substrate. There is a need for high vapour pressure at room temperature, which is created by the nebulizer.^{80,85}

There are many advantages in using AACVD over conventional CVD. AACVD uses a nebulizer to form the aerosol droplets of precursor so that it does not rely on the evaporation of precursor solution and overcomes the need for precursors to be volatile when a carrier gas passes over it. This simplifies the delivery and vaporisation of the precursors, which would reduce the cost as well as overcoming the restriction in the range of precursors that can be investigated. AACVD allows a reduction in the synthesis of multicomponent products while still having stoichiometric control. This creates more dynamic surroundings that can allow AACVD processes to be carried out at low pressure and even in open air.

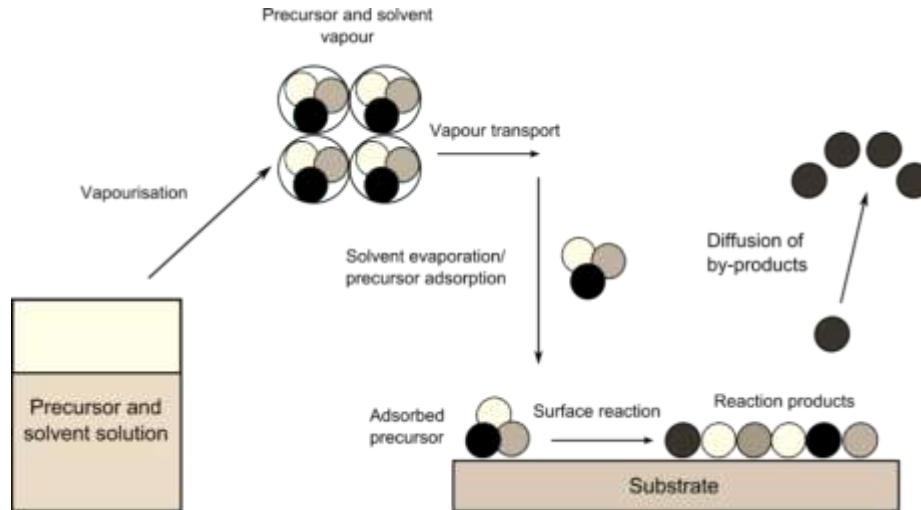


Figure 2-2: Schematic diagram of the AACVD process.

The AACVD reactor consists of a cylindrical quartz tube that is 60 mm in diameter and 160 mm in length. Within the quartz tube there is a carbon block that holds a cartridge heater and two thermocouples. On either end of the quartz tube there are stainless steel end plates at both ends. Gas is allowed to enter the reactor through a brass baffle attached to one end of the stainless steel plates and the gas is allowed to exit through the exhaust on the opposite end.

The substrate is cleaned with copious amounts of isopropanol/acetone and dried. Then the substrate is placed on top of the carbon block and SiO₂ coated float glass (supplied by NSG) is placed 10 mm above acting as a top plate. The top and bottom plates are loaded into the reactor, and it is sealed and the substrate is directly heated. The experimental set-up is known as cold-walled CVD since the bottom plate substrate is the only part that is heated.

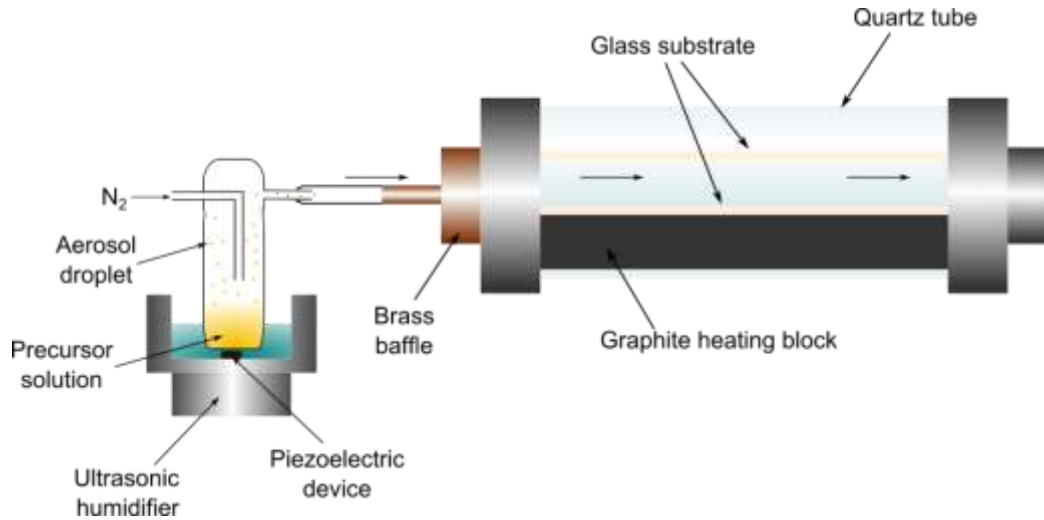


Figure 2-3: Schematic diagram of the AACVD set up.

The precursor solution was loaded into a glass flask with a thinned base, which allows for a more effective transfer of power from the piezoelectric device (attached to the humidifier) to allow for an easier generation of aerosol mist (Fig. 2-3). Aerosol droplets can be generated from liquid surfaces with the application of high-frequency sound waves in a process known as ultrasonic generation. The size of the aerosol droplet is related to Lang's equation (2.1).^{86,87} The equation states that the aerosol droplets size (d , diameter) is related to the liquid density (ρ) and surface tension (γ) of the solvent as well as the frequency (f) of the sound waves.

$$d = \left(\frac{2\pi\gamma}{\rho f^2} \right)^{1/3} \quad (2.1)$$

The size of the aerosol droplet decreases as the ultrasonic vibration frequency increases. Usually, the finer the droplet, a higher quality film is produced due to more efficient evaporation of the solvent and vaporisation of the precursor. In this piezoelectric humidifier used in our labs had an operational frequency of 20 kHz and methanol (the main solvent used throughout this project), the diameter of the droplets was 45 nm at 25 °C.

The aerosol droplets were carried into the reactor through the brass baffle through a laminar flow. Once the reaction was complete, the substrate was allowed to cool down under the flow of nitrogen until it has reached room temperature. The films were handled in air and stored in plastic wallets.

During AACVD, the morphology of the films can often change depending on a range of factors such as, temperature, solvent or substrate used. Scanning electron microscopy (SEM) was used to analyse the thin films to see if their morphology were different when using different temperatures, solvents or precursor concentration.

a) Precursors

With the use of different precursors AACVD has been shown to produce different thin film microstructure. Difference in morphology can cause an enhancement in the thin film properties. Concentration of the precursor can also affect the quality of film deposited.⁸⁸

b) Temperature

Temperature is another variable that affects the microstructure of films grown via AACVD. Temperature can also affect the coverage of the deposited thin films on the substrate. For example, different microstructure has been exhibited when $[\text{PbS}_2\text{CNR}'']_2$ (where R, R' = Me, benzyl, heptyl, octadecyl, dioctyl, Hex, Et or ⁿPr) was used to deposit thin films of lead sulfide. Thin film deposited at 350 °C formed particles on the substrate that had a dense granular microstructure whereas for depositions at 425 °C, the films consisted of non-uniform particles. Increasing the deposition temperature to 450 °C changed the morphology to a mixture of acicular platelets and non-uniform particles.^{89,90}

c) Solvent

Solvent can cause a major difference in the morphology of the film due to the change in how the aerosol mist evaporates in the AACVD chamber. The effect of solvent on crystallographic phase has also been recently reported in the

deposition of TiO₂ on steel substrates using titanium(IV) isopropoxide with a variety of solvents.⁹¹ Depositions using ethanol, hexane, dichloromethane and isopropanol produced exclusively anatase films, whereas employing methanol under identical conditions yielded exclusively rutile phase TiO₂. Solvents not only influence the morphology but can affect the compositions of the thin film. Solvents such as toluene can cause carbon contamination within the thin film, which can affect the transparency. Decolourisation of the films can be achieved by annealing in air.^{92, 93}

2.4 Film Growth

AACVD is a solution based technique that therefore leads to a number of different ways of film growth. This can be controlled which is unavailable for other techniques. Different factors and deposition conditions can influence the morphology of the thin film deposited via AACVD. These factors include precursors, temperature, solvent, growth period, and additives.

When thin films are grown, they can either be amorphous or crystalline. Crystalline thin films can be divided into epitaxial or polycrystalline films. Films are epitaxial when the lattice planes in the substrate match up with the planes in the film. This shows that the substrate and the film have very similar crystal structure and unit cells. To grow films of this type, there needs to be a low growth rate which allows for surface deposition of the atoms to be fast when compared to the arrival of new atoms. This causes the precursors to be absorbed on growth step sites that form a layer that is a replica of the substrate. High temperatures (>700 °C) are required for the formation of epitaxial films because it increases the rate of impurities being desorbed as well as increasing the mobility of precursors on the surface.

Polycrystalline is its opposite, whereby the lattice planes do not match up. This is caused by having an intermediate temperature and growth rate. This type of film occurs due to growth at different surface sites that form 'islands'. These 'islands' combine and form a layer.

On the other hand, amorphous films have no crystallinity and this kind of film growth is encouraged by low temperatures and high growth rate. These conditions cause the rate at which the precursors arrive to be faster than the surface diffusion.

2.4.1 Thin Film Growth models

The Volmer Weber or island growth model occurs when the atoms/molecules deposited have a much stronger bond to the growing surface than to the substrate (Fig. 2-4). Small clusters are nucleated directly on the substrate surface and then grow into islands of the condensed phase. Low precursor concentration and low decomposition temperatures encourage an island growth formation to occur.⁹⁴

The Frank-van der Merwe or Layer growth model is the opposite of island growth whereby the atoms/molecules are much more strongly bound to the substrate (Fig. 2-4). This is caused by the initial atoms depositing to form a layer on the surface, which is then covered by another second layer that is not as tightly bound.

The Stranski-Krastanov or intermediate growth model is a combination of island and layer growth models. In general, the first few monolayers adhere to the substrate, after that layer growth becomes unfavourable and island growth occurs.

All three of these growth models produce films that are adhesive. However, when gas phase reaction predominates, it gives rise to films that have weak interparticle interactions and tend not to be adhesive. This is known as particulate film growth.

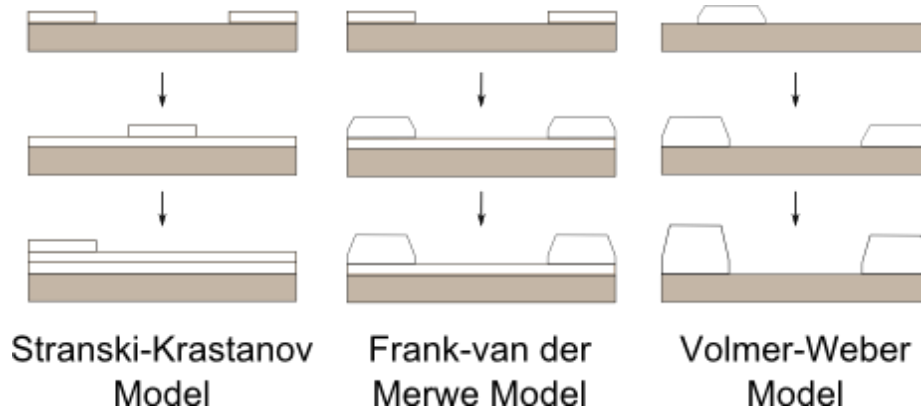


Figure 2-4: Diagram of three film growth models that can be seen in thin films.

2.4.2 Variations on CVD

The type of CVD technique selected is down to the type of film needed and the reactants available. Some variations on CVD are listed below:

- *Metal – Organic CVD (MOCVD)*; this is a process that uses metal organic precursors in the CVD process. This is usually used in the formation of films with semiconducting properties.^{95,96}
- *Plasma Enhanced CVD (PECVD)*; this CVD process uses electrical energy instead of thermal energy allowing for depositions to occur at very low temperatures. This enable the use of temperature sensitive substrates.^{81,97}
- *Low Pressure CVD (LPCVD)*; depositions take place at low pressure which will result in the reduction of unwanted by-products increasing the quality of the film. The pressures used are typically between $10^{-3} - 10^{-10}$ atm.⁹⁸
- *Atmospheric Pressure CVD (APCVD)*; this process is widely used in industry and uses pressure between $1 - 10^{-3}$ atm, which can deposit adhesive films.⁹⁹
- *Laser Assisted CVD (LACVD)*; a deposition technique that uses either atmospheric or low pressure or the use of a laser to heat the precursor or substrate.⁸¹

- *Liquid Injection CVD*; a CVD process involving the injection of the precursor within a gas system.⁸¹
- *Combinatorial CVD*; this technique can be carried out in atmospheric pressure and low pressure. It involves the use of a number of different precursors to form gradient composition films. A modified reactor is used to create a compositional spreads that can be mapped to represent the optimised properties.¹⁰⁰

2.4.3 Variations on AACVD

There are many variations on AACVD offering additional control over film microstructure and potential to overcome problems associated with precursor delivery. These variations on the technique can further increase its versatility towards materials fabrication and control of film growth and morphology.⁸⁵ Some such variants are listed below:

- *Aerosol assisted combustion CVD (AACCVD)*: Like AACVD, a precursor aerosol is generated by nebulization of a solution of precursor. Precursor aerosol droplets are then transported by a carrier gas through a flame where combustion occurs. This can offer higher deposition rates but problems can arise due to difficulties in controlling the flame temperature and the production of poor film coverage.^{85,101}
- *Electrostatic spray assisted vapour deposition (ESAVD)*: this technique involves the atomization of a liquid precursor followed by charging of the droplets by corona or induction charging. The charged droplets are then directed towards a heated substrate by an electric field where deposition occurs. Good quality thin films with high purity can be produced with this ESAVD.⁸⁵
- *Electrostatic aerosol assisted jet deposition (EAAJD)*: there is a formation of charged aerosol droplets in the same way as in ESAVD, however EAAJD incorporates a carrier gas for transport of the droplets in an electric field towards the heated substrate where the film is deposited.⁸⁵

- *Electric field assisted aerosol (EFAA) CVD*: involves an application of a potential difference between electrodes on a deposition substrate creating an electric field, which has been found to influence film microstructure.⁸⁵

2. 5 Analytical Techniques

2.5.1 Powder X-ray Diffraction

Powder X-ray Diffraction (XRD) is a technique performed on polycrystalline material such as films and gives information on the crystallinity, phase identity and crystallite size. X-ray beams interact with the sample and are diffracted off a set of periodic planes according to the Bragg's equation.

$$n\lambda=2d\sin\theta \quad (2.2)$$

Constructive interference between incident and diffracted X-rays only occur with a monochromatic X-ray beam of a particular wavelength. Diffraction peaks are only arising at diffraction angles that meet Bragg's Law.

Nearly all crystalline materials have distinct diffraction peaks, which are determined by atomic distances and different lattice spacing even though some materials may share the same unit cell type. Therefore materials can be characterised by comparing against referenced patterns of known compounds as well as calculating lattice parameters and unit cell.

In this thesis, the XRD was carried out using a Bruker D8 general area diffraction detector system (GADDS). The samples are usually analysed at low angles of incidence with an incident beam angle of 5°. The diffractometer uses a monochromatic Cu X-ray source with a major component CuK α_1 radiation of wavelength 0.154056 nm (CuK α_2 at 0.154439 nm is also present, which is not filtered), a voltage of 40 kV and current of 40 mA.

2.5.2 Scanning Electron Microscopy

Scanning Electron Microscopy (SEM) is an electron imaging technique used to record high resolution images of samples. A focused high-energy electron beam is used to interact with the sample causing emission of two types of electrons; backscattered electrons and secondary electrons.

Secondary electrons are ejected from the sample by high energy incident electrons. These electrons are usually much lower in kinetic energy than backscattered electrons therefore, can only escape from the sample and be detected if they are created near the surface of the sample. Secondary electrons are heavily influenced by the morphology of the sample. The electrons are more readily created near the peaks rather than the troughs.

SEM images were taken on a JEOL JSM-6301F Field Emission instrument with acceleration voltage ranging from 3 to 10 kV. The probe current range was 6 to 8 μ m. The images were captured using SEMAfore software. Sample preparation involved cutting the films down to coupons 1 cm x 1 cm or less and adhered to stainless steel holders using conductive carbon tape. Contacts from the top of the film to the carbon tape were made using a solution of silver paint. Once dried the samples were coated with a fine layer of carbon or gold to avoid charging.

2.5.3 Cross-sectional SEM

SEM is not only used to examine the microstructure of the thin film but the film thickness as well. The film is rotated to be perpendicular to the electron beam. In order to measure the thickness from the image taken, the film and glass substrate need to be distinguishable.

2.5.4 Energy Dispersive X-ray

Energy Dispersive X-ray (EDX) uses high energy beam that dislodges an inner-shell electron that leaves a vacancy. An electron in a higher shell falls to fill that vacancy. This fall emits radiation which is a characteristic X-rays that is specific to an element. The energy at which this occurs is measured and from the energy of the X-ray and the intensity, it is possible estimate the amount and nature of elements present in the system.

EDX in this thesis was carried out using JEOL JSM-6301F Field Emission instrument with acceleration voltage ranging from 20 kV. Sample preparation involved cutting the films down to coupons 10 mm x 10 mm or less and adhered

to stainless steel holders using conductive carbon tape. Contacts from the top of the film to the carbon tape were made using a solution of silver paint. Once dried the samples were coated with a fine layer of carbon to avoid charging.

2.5.5 X-ray Photoelectron Spectroscopy

X-ray photoelectron spectroscopy (XPS) is a surface sensitive technique based on the photoelectric effect that measures the kinetic energy of photoelectrons released. A sample is irradiated by a fixed wavelength ($h\nu$) to excite the photoelectrons. The ejected photoelectron has kinetic energy that can be related to:

$$K.E. = h\nu - B.E. - \phi \quad (2.3)$$

B.E. = Electron Binding Energy, K.E. = Electron Kinetic Energy, Φ = Spectrometer Work Function

XPS is a technique that can obtain the oxidation state, chemical environment, and concentration of an element in a sample. Each element has a characteristic binding energy for the electrons core atomic orbitals that influences the position of the photoelectron peak on the XP spectrum whereas the intensity of the peak relates to amount of the particular element.

X-ray photoelectron spectroscopy (XPS) was performed using a Thermo Scientific K-alpha photoelectron spectrometer using monochromatic $Al_{K\alpha}$ radiation. Samples were earthed using copper tape. Higher resolution scans were recorded for the principal peaks of Cu(2p), Ga(3d, 2p), Zn (2p), O(1s) and C(1s) at a pass energy of 50 eV. The peaks were modelled using CasaXPS software with binding energies adjusted to adventitious carbon (284.5 eV) for charge correction.

2.5.6 X-ray Absorption Spectroscopy

X-ray absorption spectroscopy (XAS) describes how X-rays are absorbed by atoms at energies near and above the core-level binding energies. This technique is sensitive to the oxidation state, coordination chemistry, and bond distances of the atom of interest. This technique requires a tuneable X-ray source and therefore is carried out using a synchrotron radiation; XAS was carried out by Dr. Husn-Ubayda Islam.

X-rays are absorbed by the atom and the energy of the X-ray is transferred to the core electrons that is ejected to an unoccupied or partially occupied energy levels. As energy increases, the absorption dramatically increases that gives rise to an absorption edge. This region with the dramatic raise in absorption is known as the XANES region. As the photoelectron leaves the excited atom, a backscattered waves are caused by the interaction with neighbouring atoms. The incoming and outgoing wave interferes leading to a constructive and destructive interference which appears as maxima and minima on the spectrum. This region is called extended X-ray absorption fine structure (EXAFS). Therefore, two features that can be identified on a XAS spectrum are X-ray Absorption Near Edge Structure (XANES) and Extended X-ray Absorption Fine Structure (EXAFS). The EXAFS region occurs at high energy caused by the scattering of neighbouring atoms occur.

XAS measurements were performed on the Dutch-Belgian EXAFS beamline (BM26A) at the ESRF in Grenoble. Monochromatic radiation was produced by a double Si(111) crystal monochromator, and fluorescence was measured using a 9 element germanium solid state detector. XAS data of the films was acquired in fluorescence mode. Measurements of the thin film and pelletized copper standards were taken on the copper K-edge (8987eV). XAS data were processed and XANES analysis was performed using Horae Athena software, and detailed EXAFS analysis was performed on Excurve version 9.273.

2.5.7 UV/Visible Spectroscopy

UV/Visible spectra were recorded in the range 190 – 1100 nm using a Helios double beam instrument. Reflectance and transmission spectra were recorded between 300 – 2300 nm by a Zeiss miniature spectrometer. Reflectance measurement were standardised relative to a rhodium mirror and transmission relative to air.

2.5.8 Band Gap Measurements

Band gap measurements were calculated using the UV/Vis measurements. This involves using Tauc plot calculations plotting $(\alpha h\nu)^{1/2}$ against $h\nu$ (eV), where α is the absorbance coefficient of the thin film ($\alpha = -\log T/T_0$, where T is the sample optical transmission and T_0 is the substrate optical transmission) and $h\nu$ is the incident photon energy. The plot is linear when approaching the absorption band energy and an extrapolation of this region is taken where the extrapolation linear line crosses the y axis, this is the band gap value for the thin film (Fig. 2-5).¹⁰²

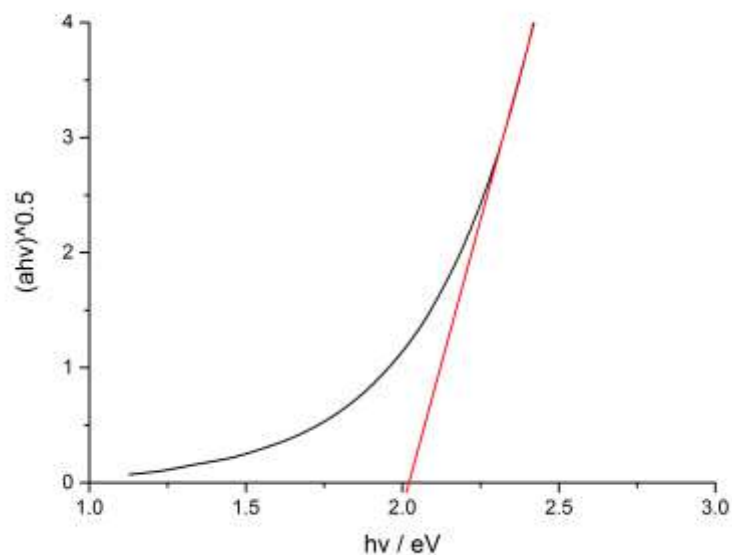


Figure 2-5: Example of the extrapolation of a Tauc plot to calculate the band gap measurements.

2.6 Microbiology Analysis

2.6.1 Viable Colony Counting Technique

In all microbiological experiments described analysis of microbes was performed using serial dilutions (Fig. 2-6) and viable colony counting technique on agar medium, which is a standard technique used in microbiology. Overnight inoculum of bacterial cell culture has a concentration of approximately 10^6 colony forming units (cfu).

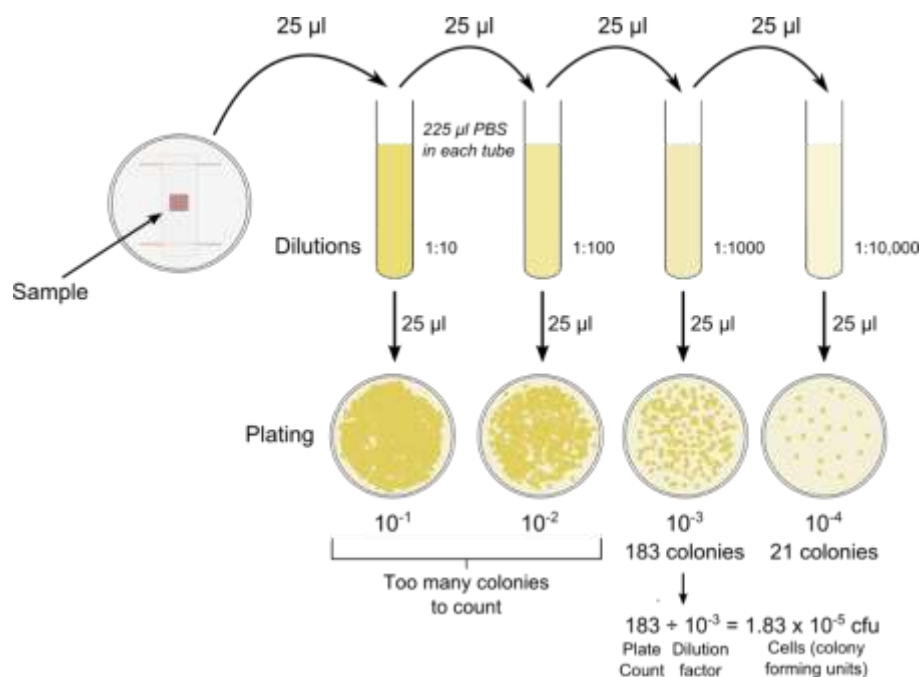


Figure 2-6: Diagram describing the steps involved in serial dilution.

Incubation of an agar plate with this concentration will cause a confluent amount of growth resulting in individual colonies being indistinguishable from one another rendering the plates uncountable. It is important that the number of colonies developing on the plate is not too many or too few. A crowded plate causes some colonies not to form and others may fuse together. However, if the numbers of colonies are too small this causes the statistical significance of the calculated colony number to be low. In order to avoid this, it is necessary to dilute the overnight inoculum to allow fewer colonies to grow. This is commonly achieved by carrying out 10-fold dilutions of the sample solution using a suitable

medium. Each successive dilution is 10 times more dilute than the previous solution (Fig. 2-6). These dilutions are then plated and incubated. After 24 hours of incubation, there should be at least one plate with a countable number of colonies with suitable counts (10 - 400). The colony count number is then multiplied by the dilution fraction in order to find the colony count in the initial sample. Data is often expressed as the number of colony-forming units (cfu) obtained rather than the actual number of viable cells because cfu may contain one or more cells.¹⁰³

2.6.2 Experimental Design

The method of microbiology analysis involved the use of an individual moisture chamber that consists of a petri dish with filter paper at the base, which has been moistened with sterilised distilled water. Sterilised wooden sticks cut to size were placed on top of the filter paper and a microscope slide was placed on top of the sticks. The thin film samples deposited on microscope slides cut to 1x1 cm in size are placed on top of the microscope slide and a lid was placed to cover the testing samples (Fig. 2-7).

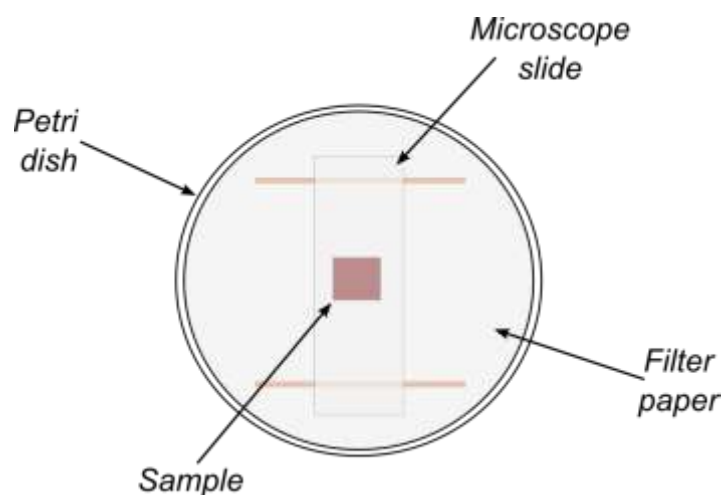


Figure 2-7: Diagram of the experimental set up of the humidity chamber.

2.6.3 Microorganism Selection

The microorganism selections for this study represent both gram positive and gram negative type bacteria (Table 2-1). The difference between the two types depends on their cell wall morphology (Fig. 2-8). The cell wall of the bacteria can govern the organism's behaviour.

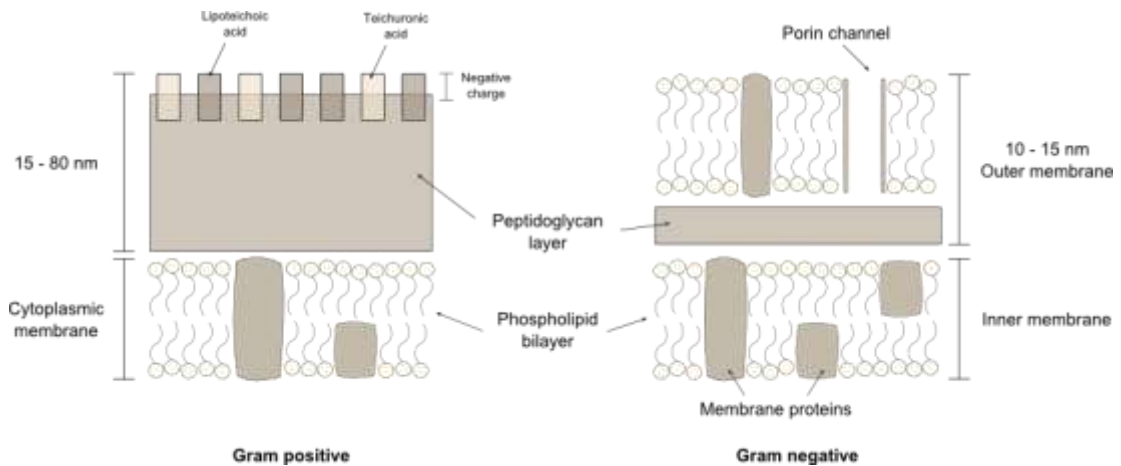


Figure 2-8: Diagram of the cell wall of gram positive and gram negative bacteria.

Table 2-1: List of bacterial strains used in this thesis and their cell wall type.

Bacterial Strain	Gram positive or negative
<i>Escherichia coli</i> (NCTC 25522)	Gram negative
<i>Staphylococcus aureus</i> (E1162)	Gram positive
<i>Pseudomonas aeruginosa</i> (PA01)	Gram negative
<i>Enterococcus faecium</i> (E1162)	Gram positive

Gram positive bacteria have a cell envelope consisting of an inner cytoplasmic membrane and an outer membrane separated by peptidoglycan containing periplasm. The outer layer acts as a barrier against its environment. Within the outer layer, there are several proteins where some act as passages and are composed of a thick peptidoglycan layer, which is porous, enveloping the cytoplasmic membrane. Gram negative bacteria have a cell envelope consisting of

an inner cytoplasmic membrane and an outer membrane separated by peptidoglycan-containing periplasm. This outer layer acts as a barrier against its environment. Within the outer layer, there are several proteins where some act as passages to allow nutrients, while other proteins act as enzymes.^{104,66}

2.6.4 Light Source

For light photocatalysis experiments, a General Electric 28W Biax 2D compact fluorescent lamp (GE Lighting Ltd., Enfield, UK) was used. This lamp emits light across the visible spectrum, as shown in Fig. 2-9 and is commonly found in UK hospitals. During the experiments, the lamp was affixed inside an incubator where the temperature is maintained at a constant of 21 ± 2 °C. The light intensity was measured using a lux meter (LX101 Lux meter, Lutron Electronic Enterprise Co. Ltd., Taiwan).

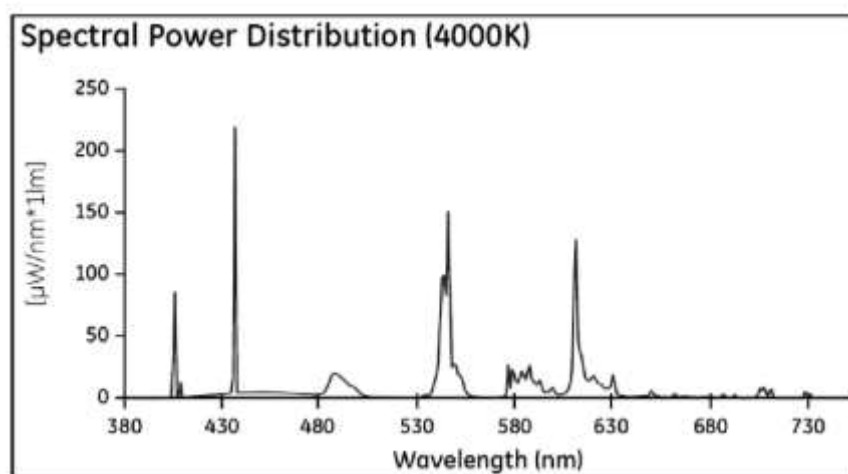


Figure 2-9: Spectra power distribution of general electric 28W Biax™ 2D lamp.

2.7 Antimicrobial Susceptibility Testing

Susceptibility testing is commonly used in microbiology laboratory to test the performance of antibiotics. The most widely used testing methods are disk diffusion and broth dilution tests. In this thesis, broth dilution tests were used to produce quantitative results. The purpose of these tests was to measure the minimum inhibitory concentration (MIC) and minimum bactericidal concentration (MBC).

2.7.1 Broth Dilution Test

One of the easiest methods for testing susceptibility is using micro broth or tube-dilution. In this thesis, broth micro dilution was used to test the MIC and MBC as shown in Fig. 2-10. MIC is the measurement of the smallest amount of antimicrobial agent that can inhibit visible growth of the bacteria and MBC is the smallest amount of agent needed to kill the test bacterium. This procedure involved two-fold dilution of the antimicrobial agent in a liquid growth medium. In this case, Müller-Hinton broth was used and dispensed into the wells of the micro-dilution dish. The wells containing the antimicrobial agent were inoculated with approximately 10^6 cfu ml⁻¹ and the dish was placed overnight in an incubator set at 37 °C. The bacterial growth was examined by observing the turbidity to determine MIC and MBC. The main advantage of this technique is the generation of quantitative results which can be easily reproduced.^{105,106}

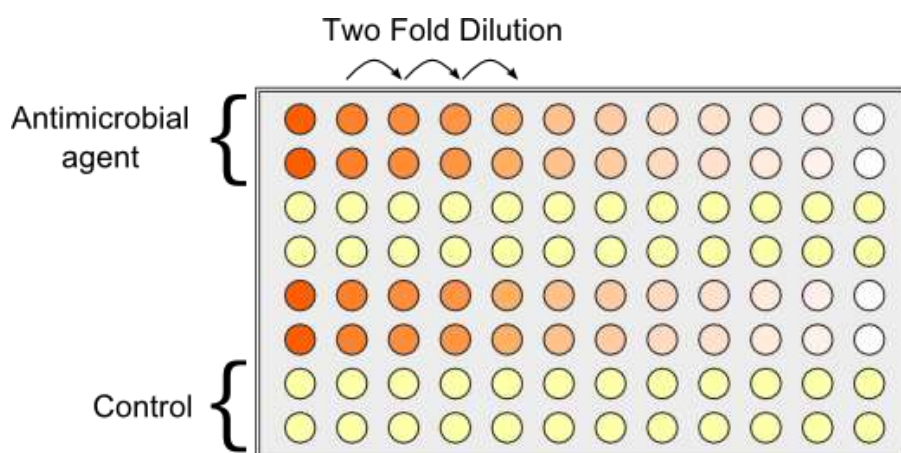


Figure 2-10: Diagram of the broth dilution set up using a micro-dilution dish for MIC and MBC detection.

2.8 Statistical Analysis

Experimental data is subjected to statistical analysis in order to determine the significance of the decrease in colony forming units (cfu) observed. The statistical analysis used is a non-parametric test known as Mann Whitney U test. This test is used to compare two different sets of independent data. Non-parametric test was chosen due to the assumption that the data is not normally distributed.

The null hypothesis is:

H_0 ; "There is no difference between the antimicrobial activity (colony counts) of the thin films and the control samples."

The alternative hypothesis:

H_1 ; "There is a difference between the antimicrobial activity (colony counts) of the thin films and the control samples."

Data was analysed using SPSS (version 16.0, SPSS, Inc. Chicago, IL, USA) statistical software package. The output from the analysis from this software includes a range of different data but the data point of interest to this thesis is the P value. The P value is needed to test the null hypothesis against the significance level. The statistical significance of the data will be represented by asterisks (Table 2-2).¹⁰⁷

Table 2-2: Asterisks system to define the statistical significance.

P Value	Asterisk	Level of Significant
P < 0.05	*	<i>Significant</i>
P < 0.01	**	<i>Very Significant</i>
P < 0.001	***	<i>Highly Significant</i>

3

Copper and Copper(I) Oxide

The following chapter presents the results obtained from an investigation into the use of copper and copper oxide thin films for antimicrobial applications deposited via aerosol assisted chemical vapour deposition. The thin films were fully characterised and tested for their antimicrobial properties using serial dilution and viable colony counts on to agar plates. A description of copper nanoparticle susceptibility towards a range of bacteria was investigated using Agar and Broth dilution methods and will also be discussed.

3. Introduction

Copper is a well-known antimicrobial agent that has been used throughout history. The oldest recorded documentation of copper's antimicrobial ability is contained in an Egyptian medical text dating between 2200 and 2600 BC, describing the use of copper for the disinfection of water and treatment of wounds.^{108,109} In many living organisms copper is an essential trace element and there are many copper-containing proteins, where copper acts as an electron donor/acceptor due to its ability to switch between oxidation states.¹¹⁰ Copper is an essential metal needed for many functions in organisms although in large concentration it can be toxic.¹¹¹ The development of antibiotic resistance, and the increase of HAI require a new approach to deal with infections (Chapter 1). An alternative system proposed is the use of copper surfaces for hygiene sensitive areas, such as hospitals.¹¹²

3.1 Copper vs Stainless Steel

In vitro experiments carried out to test the antibacterial properties of copper materials were first conducted over 30 years ago when it was noted that stainless steel doorknobs and stainless steels strips did not have antimicrobial activity while brass and copper strips did exhibit activity.¹¹³ More recent studies have also shown that copper has antimicrobial activity against a wide range of bacteria including *Staphylococcus aureus* (*S. aureus*)¹⁰⁹ and *Escherichia coli* (*E. coli*).¹¹⁴

Recently studies have investigated the length of time *E. coli* O157:H7 can survive on copper based touch surfaces for 2 hours and compared it to stainless steel. The antimicrobial copper was very effective as a touch surface material, killing greater than 99.9 % of the *E. coli* strain within 2 hours, whereas there was no significant reduction in the cfu counts for stainless steel. This indicates that stainless steel may not be the ideal choice as a touch surface in hospitals.

In *in situ* investigations in a busy ward of a UK hospital, frequently touched fixtures and fittings were replaced with copper and copper alloys containing a

minimum of 60% copper. This ten week study found that all copper containing items on average had between 90 and 100% lower microbial contamination when compared to control fixtures and fittings.^{115,116}

Touch surfaces are described as door handles, bed railings, call buttons and toilet seats. Studies have shown that microbes can survive on these touch surfaces and hence they can be seen as a microbial reservoir. Touch surfaces are predominately made from stainless steel due to the clean appearance and its resistances to corrosion. However, stainless steel does not possess any antimicrobial properties.¹¹⁷

The use of copper instead of stainless steel has the potential to reduce infections rates due to the intrinsic self-sanitising properties. There have been hospital trials worldwide indicating how copper can provide protection from the spread of infections.

3.1.1 Clinical Trials

- Birmingham, UK

A clinical trial took place at Selly Oak Hospital located in Birmingham, UK in a general medical ward containing copper touch surfaces as well as standard components. This method was chosen to demonstrate the ability of copper to reduce the bacterial burden on the surrounding environment. A 10 week trial were carried out where the copper and control surfaces were interchanged after 5 weeks. Over the trial period, all copper fixtures had 90 – 100% less microbe contamination when compared to their controls made from chrome-plated brass, aluminium and plastic.¹¹⁵

- United States

Three institutions, (the Medical University of South Carolina, Charleston (MUSC), The Ralph H Johnson Veterans Administration Medical Centre, Charleston, South Carolina and the Memorial Sloan Kettering Cancer Centre, New York City), replaced frequently touched surfaces and objects made from stainless steel, aluminium and plastic with copper. These studies were carried out over 43 months and the microbial burden was analysed for six objects.

Results showed that the introduction of copper touch surfaces significantly reduced the microbial burden by 83% on average and gave a reduction on a continuous basis. These trials also examined the recontamination of newly installed copper surfaces compared with control plastic surfaces. Copper was found to consistently limit surface bacterial burden before and after cleaning and gave a continuous antimicrobial effectiveness to the copper surfaces and the surrounding items. The use of copper touch surfaces inside the intensive care unit (ICU) led to a 58% reduction in nosocomial infections.¹¹⁸

- *Hospital de Cobre, Chile*

Approximately 70, 000 people contract a nosocomial infection annually in Chile. A clinical trial at Hospital del Cobre, Calama, inside the ICU took place for 30 weeks. Six types of surfaces (bed rails, bed levers, tray tables, chair arms, monitor pens, and IV poles) were replaced with copper resulting in over 900 surfaces being replaced in 90 rooms. This was compared against the equivalent number of rooms and surfaces to act as a control.

The results from this study revealed that the copper surfaces produced a 90% reduction in microorganism contamination and the copper demonstrated continuous antibacterial activity throughout the trial. The bacterial burden on the six surfaces studied showed a significant reduction when compared to the rooms without the copper surfaces with bed rails having the highest reduction (91%) and monitor pens having the least (49%).^{119,120}

- South Africa

A controlled study was carried out in a busy walk-in healthcare clinic located in a rural region of the western cape of South Africa. The trial involved two similar consulting rooms and was carried out over 6 months. One room was fitted with copper surfaces on the areas that are frequently touched by staff and patients, whereas the second room remained the same to act as a control. To monitor the effectiveness of the copper, no disinfectants were used in these environments. The study was carried over the winter, spring and summer to examine the effect of climate and temperature. The study showed that it made no significant difference to the antimicrobial activity of the copper touch surfaces. On average the copper touch surface exhibited a 71% reduction when compared to the control surfaces.¹²¹

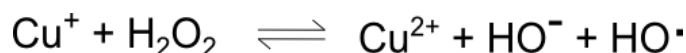
3.1.2 Copper toxicity

Although the exact mechanism of the antimicrobial activity of copper is not known, many investigations have pointed to reactive oxygen species (ROS) produced through Fenton-type reactions leading to DNA damage.¹²² The release of copper ions causing inactivation of enzymes has also been attributed to its toxicity.¹²³ Much research has looked into the antimicrobial mechanism of copper and there have been suggestions that activities take place in many different ways both inside and out of the bacteria cell.^{109,124}

The redox properties of copper can be exploited in order to cause cell damage. It has been suggested that copper toxicity was attributed to copper ions participating in a Fenton-type reaction. The creation of radicals caused by UV light promotes the formation of hydrogen peroxide (H₂O₂). A Fenton-type reaction occurs in many biochemical reactions that can lead to the formation of H₂O₂ and superoxide radicals leading to multiple redox reactions at specific sites causing 'multi-hit' damage. The simplest form of Fenton-like reaction involves ferrous iron behaving as a catalyst to form hydroxyl radicals from hydrogen peroxide:



HOO· is the protonated form of superoxide. Other transition metals such as copper can also be involved in a process like this leading to a damaging effect on DNA, lipids and proteins that eventually lead to the bacterial cell death. In the case of copper, Cu(I) undergoes an oxidation reaction with H₂O₂ to form hydroxyl radicals. These hydroxyl radicals are extremely reactive and can undergo a wide range of reactions that can damage cell wall of bacterium by disrupting the lipid bilayer and denaturing proteins.^{111,125}



The concentration of H₂O₂ is very low inside bacteria cells suggesting that this Fenton type reaction may not be the main source for copper toxicity. Research has shown that copper has a strong affinity for bonding to sulphur, nitrogen and oxygen containing groups which can cause disruptions in protein structures.^{123,126}

Investigations have described copper toxicity occurring due to damage to DNA and contact killing, which damages the membrane. A mechanism of copper toxicity has been proposed which involves dissolved copper ions damaging the cell membrane and bacteria (Fig. 3-1a). This leads to cell rupture (Fig. 3-1b) leading to secondary reactions of the formation of ROS (Fig. 3-1c), which in turn causes further damage to the cells. This leads to the eventual degrading of DNA (Fig 3-1d).¹¹⁰ The mechanism suggested for contact kill are very similar to silver where the mechanism of action of silver is linked with its interaction with thiol group compounds found in the respiratory enzymes of bacterial cells. Silver binds to the bacterial cell wall and cell membrane and inhibits the respiration process.¹²⁷

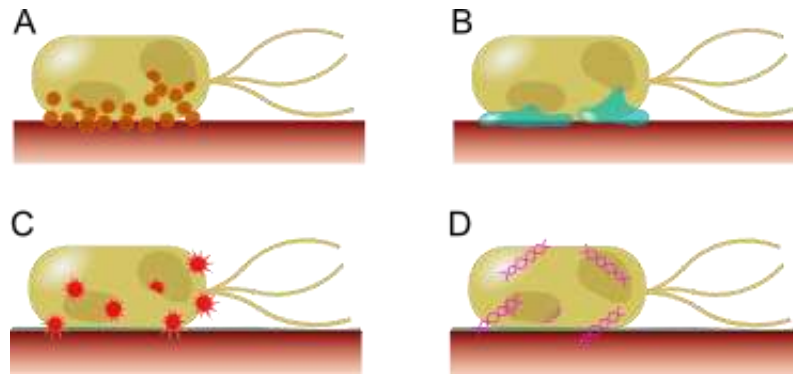


Figure 3-1: Diagram illustrating the proposed events that occur during contact killing of copper against bacteria.

3.1.3 Halo Effect

Copper surfaces also experiences a 'halo effect' whereby, the antimicrobial activity of copper spreads to other non-copper materials nearby. This helps prevent the spread of infection and enhances the effect of the copper touch surfaces.¹¹⁸

3.1.4 Copper Oxide

It has been reported that the antimicrobial activity of silver occurs when silver is ionised. As a result, copper oxide will be investigated to see if there is enhanced efficacy. There has been some investigation in to cupric Oxide (CuO) nanoparticle which previously has been shown to be effective in killing bacteria involved in HAI. It has been suggested that the high surface area and unusual crystal morphology causes the antibacterial effect. A local change in pH and conductivity, suggests that there is a release of Cu^{2+} ions into the solution. The ions are small enough to enter the cell and disrupt enzymes, which can lead to the death of pathogens.¹²⁸

3.1.5 Deposition of copper

Due to the antimicrobial properties of copper, it may be appropriate to use copper for hospital touch surfaces instead of stainless steel to reduce microbial contamination. In this chapter, the antimicrobial activity of copper and copper oxide deposited via aerosol assisted chemical vapour deposition (AACVD) will be described. Copper films have been previously deposited using different variations of CVD, Metal–Organic (MO) CVD, using $[\text{Cu}(\text{hfac})_2]$ or $[\text{Cu}(\text{hfac})\text{L}]$ (where hfac = hexafluoroacetylacetonate and L = neutral soft donor).^{129,130} However, these precursors have a low thermal stability which causes them to have a short shelf-life. Improvements on copper precursors have been investigated¹³¹ and copper alkoxides, such as $[\text{Cu}(\text{OCHCH}_3\text{CH}_2\text{NR}_2)_2]$ (where R = Et or Me) have been used to deposit copper successfully and have the potential for low budget synthesis. Copper(I) amidinate $[\text{Cu}\{(\text{iPrN})_2\text{CMe}\}]_2$ has also been used to deposit copper on to a range of substrates.¹³¹⁻¹³³ A disadvantage of this is the relatively high temperatures needed for depositions resulting in the formation of copper oxide. The structure of these precursors are shown in Fig. 3-2.

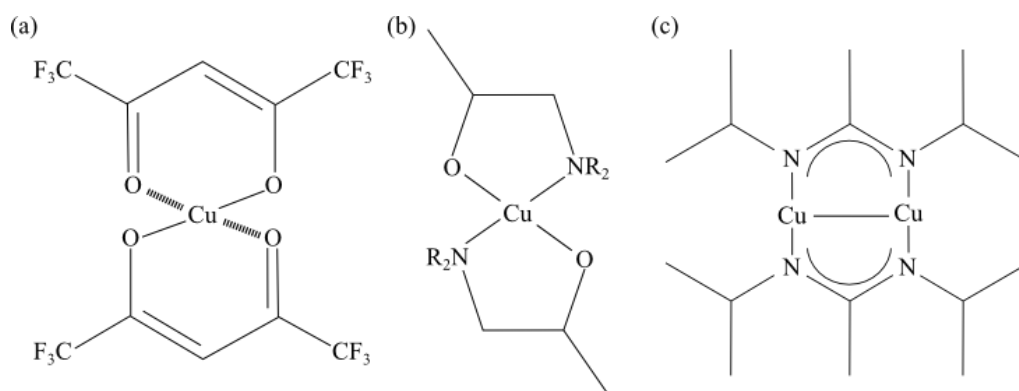


Figure 3-2: Structural diagram of copper precursors a) $[\text{Cu}(\text{hfac})_2]$, b) $[\text{Cu}(\text{OCHCH}_3\text{CH}_2\text{NR}_2)_2]$ and c) $[\text{Cu}\{(\text{iPrN})_2\text{CMe}\}]_2$.

This investigation describes the deposition of copper metal and cuprous oxide via a single step AACVD, and assessment of the antimicrobial activity of the resulting films. The copper precursors (Fig. 3-3) that were investigated are copper acetate monohydrate ($\text{Cu}(\text{OOCCH}_3)_2 \cdot \text{H}_2\text{O}$ or $\text{Cu}(\text{OAc})_2 \cdot \text{H}_2\text{O}$) and copper(II) acetylacetonate ($\text{Cu}(\text{O}_2\text{C}_5\text{H}_7)_2$ or $\text{Cu}(\text{acac})_2$) and copper nitrate trihydrate ($\text{Cu}(\text{NO}_3)_2 \cdot 3\text{H}_2\text{O}$). Copper oxide thin film was also investigated in order to see if the antimicrobial activity increases or decreases. Previous investigations have shown that the efficacy of copper oxide approaches that of pure copper.¹³⁴ AACVD is a simple and industrially scalable process that has low maintenance and set up costs involved in scaling up the process. The AACVD process is able to deposit films onto a large variety of substrates for different applications including antimicrobial surfaces.

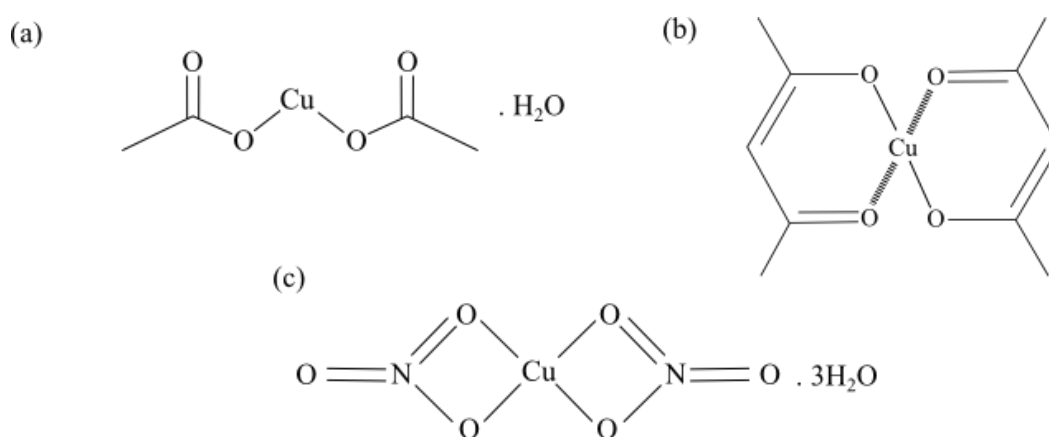


Figure 3-3: Structural diagram of copper precursors investigated in this chapter a) $\text{Cu}(\text{OAc})_2 \cdot \text{H}_2\text{O}$, b) $\text{Cu}(\text{acac})_2$ and c) $\text{Cu}(\text{NO}_3)_2 \cdot 3\text{H}_2\text{O}$.

3.1.6 Susceptibility Testing of Copper Nanoparticles

As described in Chapter 1 there are many methods for preventing the spread of microbes in hospitals before they can cause infection to develop. Some approaches include using photoactive agents such as TiO₂, however this chapter describes the antimicrobial properties of metal nanoparticles such as copper.

Recent research in the field of nanotechnology has been of interest since producing nanoparticles (NPs) can offer an alternative strategy to tackle nosocomial infections that are resistant to multiples of antibiotics. NPs can generally be described as particles that have one dimensional measurement ranging from 1 - 100 nm. These dimensions give the NPs unique chemical, optical and biological properties that can be manipulated to fit your desired application. Whereas, bulk materials possess relatively constant physical properties regardless of their size. The size of the NPs allow them to have a greater surface area to volume ratio giving NPs chemical properties observed.^{135,136}

NPs maximise the interaction between the metal and bacteria due to the increase surface area improving ion release. For smaller size particles, there is a rise in surface area which increases the probability of more interactions with bacteria cell membranes. The large surface area of the NPs enhances the interaction with the microbes.¹³⁷

Metal NPs that exhibit antimicrobial activity have been embedded or coated on the surface of materials that can be used in applications for medical devices, food processing and packaging.^{77,138} There is a need for the development of biologically compatible material at a nanoscale that can be used in medicine. The antimicrobial properties of copper and copper(II) oxide thin films were previously described. In this section, the antimicrobial properties of copper and copper oxide NPs is discussed.

In this work, Dr Ralph Leech synthesised water-soluble copper NPs using tiopronin as a capping agent and copper nitrate (Fig. 3-4). This produced bright

orange copper NPs that were stable in air for up to a week. However, in oxygenated water, the NPs would oxidise to form a green solution.

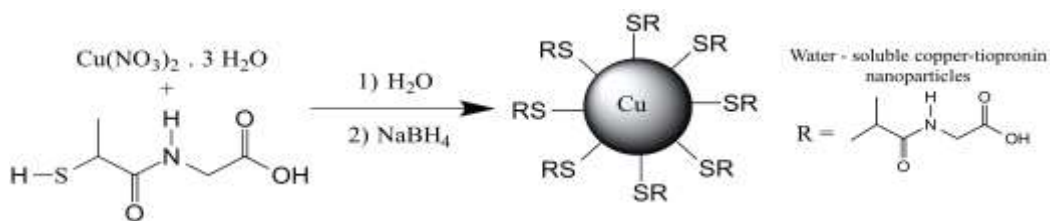


Figure 3-4: Reaction scheme to show synthesis of tiopronin stabilised Cu NPs (From Ralph Leech's thesis).

Antimicrobial Activity of Nanoparticles

Factors that can influence the NP toxicity can be attributed to size, shape, surface charge, concentration, coating on NP, and stability. It can also be attributed to reactive oxygen species and membrane disruption. NPs are generally smaller in size than bacterial pores, and they will have the unique ability of crossing the cell membrane. It has been reported that the smaller the particle size, the better antimicrobial activity. Cu ions released by the NPs may attach to the negatively charged bacterial cell wall and rupture it leading to denaturising of proteins and cell death. Crossing of NPs from the bacteria cell membrane can then damage the vital enzymes of bacteria.¹³⁷

The antimicrobial activity of the Cu NPs and oxidised Cu NPs was investigated. The Cu NPs and oxidised copper NPs were shown to have antimicrobial activity against *Escherichia coli* (*E. coli*), *Staphylococcus aureus* (*S. aureus*), *Pseudomonas aeruginosa* (*P. aeruginosa*) and *Enterococcus faecium* (*E. faecium*).

As a way of measuring antimicrobial activity, the minimum inhibitory concentration (MIC) and minimum bactericidal concentration (MBC) were investigated. The MIC of an antimicrobial agent is the measurement of the smallest amount of the agent that is needed to inhibit the growth of the test organism, whereas the MBC is the lowest concentration of the agent required to kill the test organism.⁶⁶ To determine the MIC and MBC, the tube dilution

techniques were performed. This involved a series of culture tubes with differing concentrations of the antimicrobial agent, with the same volume of microbial concentration. After incubation, the tubes were checked visibly to see if there is any growth (turbidity). The MIC is the lowest concentration of the agent that remains clear (no growth). The MBC is observed by planting the concentrations that inhibited the growth of the test organism onto the agar. The lowest concentration where no growth on the agar, is seen is the MBC.

The microbial growth with varying concentration of the antimicrobial agent was also investigated to detect the number of cells observed by recording the optical density.

Phases of Bacterial Growth

When a culture is allowed to grow in a closed tube/flask, a batch culture is created. A typical growth curve for the population of the organism's cells can be plotted, which can describe the entire growth cycle (Fig. 3-5). This growth cycle can be broken down into four distinctive phases; lag phase, log phase, stationary phase and death phase.⁶⁶

There are many different ways to measure bacteria growth; viable counts, dilution and measuring turbidity. In the investigation, the turbidity of the cell suspensions was recorded. A spectrophotometer is used to measure the turbidity of the cell suspensions due to presence of cells causing a scattering of light. The more cells present, the more light scatters causing the suspension to appear cloudy. Optical density is recorded which indicates that the scattering is proportional to the cell density up to high concentrated cultures.

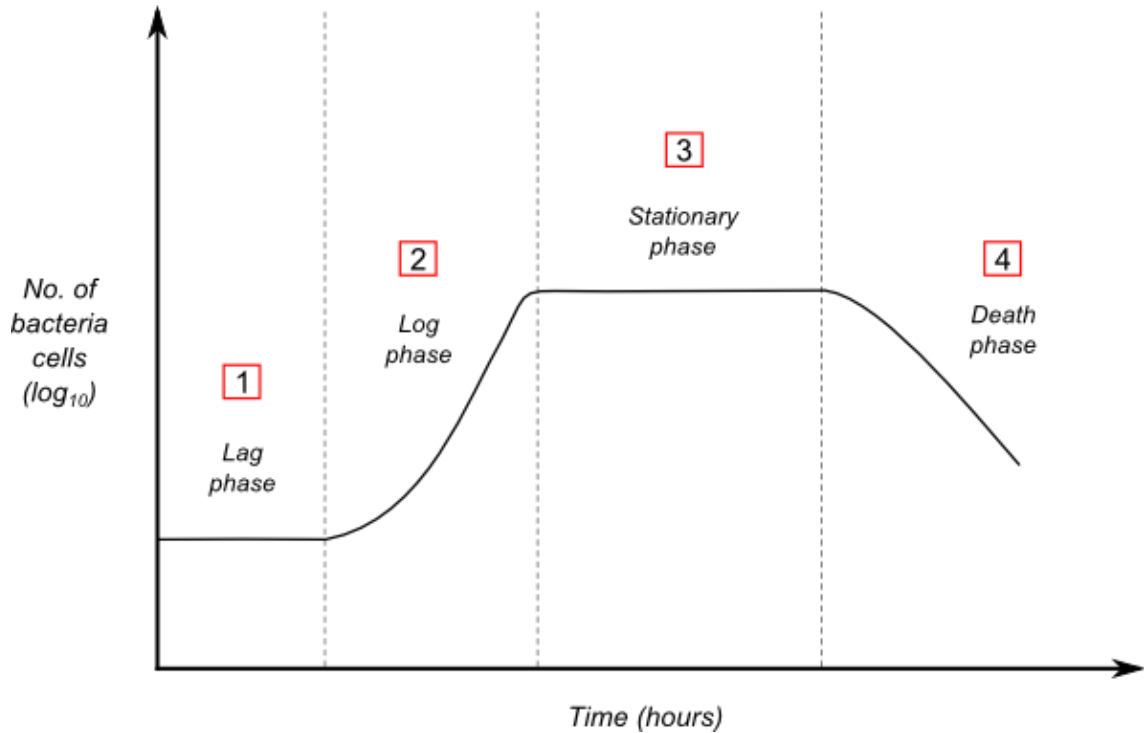


Figure 3-5: Graph depicting the different stages in the growth cycle for bacteria.

1) Lag phase

This phase describes the time where the microbial population increases in size and cell mass but the organisms do not replicate. Immediately after inoculation, the cells are adapting to fresh medium causing the bacteria population to remain constant. The lag phase is the most difficult in which to predict the growth. Many factors influence this stage due to the change in nutrition, physical environment, and temperature. The prediction of this phase is important for food industry in order to determine the shelf life of products.^{139,140}

2) Exponential or Logarithmic (log) phase

This is the period where the growth of organism occurs due to the division of two or more cells, which in turn divides into two more or cells. Multiplication of cells occurs at a rapid rate. The length of this phase depends on the resources available. There is a linear relationship between time and logarithm of the number of

bacteria cells. This rapid cell multiplication increases the mass exponentially. This growth rate is constant and can be expressed as the generation time (the time it takes for bacterial cell population to double).¹³⁹

3) Stationary phase

The stationary phase is due to growth being carried out in a closed system (batch culture) leading to limiting the multiplication of bacteria population limiting due to decrease of available nutrients, accumulation of toxic waste material and the lack of space. During this stage, the number of cell division is equal to the number of cell deaths causing the overall population growth to remain constant. If given fresh medium, exponential growth would resume.⁶⁶

4) Decline or Death phase

As the resources decrease and the toxic waste material increase, the microbial population enters the death phase of the cycle. The number of dead cell begins to outnumber the number of live cells reducing the population numbers.⁶⁶

3.2 Experimental

All chemicals used in this report were purchased from Sigma-Aldrich Chemical Co. Nitrogen (99.99%) was obtained from BOC and was used as supplied. Deposition was on microscope slides or 150 × 45 × 45 mm SiO₂ coated float-glass (the SiO₂ acts as a barrier layer preventing diffusion of ions from within the glass into the deposition film) which has been supplied by Pilkington NSG. Prior to use the glass substrate were cleaned with acetone and isopropanol and was monitored using a Pt–Rh thermocouple.

Nitrogen was passed through a two-way tap, which was used to divert the nitrogen carrier gas through a glass bubbler. All deposition experiments were conducted by heating the cold-wall horizontal-bed reactor to the required temperature before diverting the nitrogen line through the aerosol into the reactor. The aerosol was carried into the reactor in a stream of nitrogen gas through a brass baffle to obtain a laminar flow. The gas flow was continued until all of the precursor mix had passed through the reactor, typically 1 h. The glass substrate was allowed to cool with the graphite block under a flow of nitrogen until it reached room temperature before it was removed.

3.2.1 AACVD of [Cu(OAc)₂.H₂O] with MeOH

Copper acetate, [Cu(OAc)₂.H₂O, 2.5 mmol] was added to 40 mL of methanol. An aerosol was generated at room temperature using a humidifier with the graphite heating block under the glass substrate heating the CVD reactor to 350 - 550 °C. The film was allowed to cool under a flow of N₂ until room temperature.

3.2.2 AACVD of [Cu(acac)₂] with MeOH

Copper(II) acetylacetonate, [(Cu(acac)₂), 1.91 mmol] was added to 40 mL of methanol. An aerosol was generated at room temperature using a humidifier with the graphite heating block under the glass substrate heating the CVD reactor to 350 - 550 °C. Not all of the [Cu(acac)₂] was able to dissolve in the methanol and some of the precursor was left behind the AACVD bubbler. The film was allowed to cool under a flow of N₂ until room temperature.

3.2.3 AACVD of $[Cu(NO_3)_2 \cdot 3H_2O]$ with MeOH

Copper nitrate trihydrate ($[Cu(NO_3)_2 \cdot 3H_2O]$, 2.07 mmol) was added to 40 mL of methanol solvent. After addition the solid was allowed to dissolve and used immediately for AACVD deposition. An aerosol was generated at room temperature using a PIFCO ultrasonic humidifier. A graphite heating block under the glass substrate heated the CVD reactor to 350 °C. Once all the aerosol had passed through and had finished, the films were allowed to cool under nitrogen to form copper films. To form copper oxide films the experimental procedure was the same as for the AACVD reaction to form copper but the film was allowed to cool in air instead of nitrogen.

3.2.4 Characterisation

The resulting copper and copper oxide films were handled and stored in air. The coated glass substrates were used for powder X-ray diffraction (XRD) and then were cut into 1 cm × 1 cm squares for subsequent analysis by Scanning Electron Microscopy (SEM), on a JEOL 6301 filament scanning electron microscope. A Perkin-Elmer Lambda 25 UV-Vis Spectrometer was used to measure the UV-Vis absorption spectra of copper(I) oxide samples.

3.2.5 Antimicrobial activity

E. coli strain (ATCC 25922) and *S. aureus* (8325-4) were maintained by weekly subculture on Brain Heart Infusion (BHI) agar (Oxoid, Basingstoke, UK). One bacterial colony of either *E. coli* or *S. aureus* was used to inoculate 10 mL of sterile BHI broth (Oxoid, Basingstoke, UK) and incubated aerobically at 37 °C for 24 hours. Bacteria from the overnight culture were harvested by centrifugation at 13000 × g for 1 minute. Bacteria were then re-suspended in phosphate-buffered saline (PBS) (Oxoid, Basingstoke, UK) and again centrifuged at 13,000 × g for 1 minute. Finally the bacterial pellet was re-suspended in PBS before use. The turbidity of the bacterial cell suspension was measured at 600 nm using a

spectrophotometer and was adjusted to an optical density which corresponded to approximately 10^6 colony forming units (cfu) per 25 μ L aliquot.

Prior to use, the copper and copper(I) oxide slides were cut into 1×1 cm sections. A humidity chamber was created to ensure that the suspensions did not dry out. For each exposure time, triplicate samples were analysed and uncoated glass microscope slides were used as a control. Each exposure time was also repeated on three separate occasions. A 25 μ L aliquot of the bacterial cell suspension was spread evenly on the surface of each slide and incubated at room temperature (21 ± 2 °C) for the allocated exposure time. After incubation the slides were aseptically transferred to 225 μ L PBS and vortexed for 30 seconds to release the bacteria into the solution. Serial dilutions of the resulting bacterial suspensions were prepared in PBS and 25 μ L from each dilution was spread on to MacConkey Agar (Oxoid, Basingstoke, UK) for *E. coli* and BHI agar (Oxoid, Basingstoke, UK) for *S. aureus*. Plates were incubated aerobically at 37 °C for 24 hours. After incubation, any bacterial colonies were counted and viable counts of bacteria were calculated. Mann-Whitney U test was used to determine the significance of the activity of copper or copper(I) oxide slides compared to the control glass slide.

The longevity of the copper and copper(I) oxide was investigated over 7 days. The experiments were repeated, as described above, however the samples were kept and not placed into the 225 μ L PBS and were not vortexed. Instead only the aliquots placed on the sections were vortexed. Serial dilutions of the resulting bacterial suspensions were prepared in PBS and 25 μ L from each dilution was spread on to MacConkey Agar (Oxoid, Basingstoke, UK) for *E. coli* and BHI agar (Oxoid, Basingstoke, UK) for *S. aureus*. Plates were incubated aerobically at 37 °C for 24 hours. The sections of copper and copper(I) oxide were cleaned with alcohol (70%) and repeated on day 4 and day 7. Each test was done in triplicate, duplicated and compared to glass controls.

3.2.6 Bactericidal Assays

The minimum inhibitory concentration (MIC) was determined using the broth dilution method to achieve doubling concentrations of copper nanoparticles dispersed in phosphate-buffered saline solution. *E. coli* (NCTC 25522), *S. aureus* (8325-4), *P. aeruginosa* (PA01) and *E. faecium* (E1162) were maintained by weekly subculture on Brain Heart Infusion (BHI) agar (Oxoid, Basingstoke, UK). One bacterial colony of each of the bacteria mentioned was used to inoculate 10 mL of sterile BHI broth (Oxoid, Basingstoke, UK) and incubated aerobically at 37 °C for 24 hours. Bacteria from the overnight culture were harvested by centrifugation at 13,000 xg for 1 minute. Bacteria were then re-suspended in phosphate-buffered saline (PBS) (Oxoid, Basingstoke, UK) and again centrifuged at 13, 000 xg for 1 minute. Finally the bacterial pellet was re-suspended in PBS before use. The turbidity of the bacterial cell suspension was measured at 600 nm using a spectrophotometer and was adjusted to an optical density which corresponded to approximately 10⁶ colony forming units (cfu) per mL aliquot.

Assays were performed with initial nanoparticle solutions of concentration 8 mg ml⁻¹ and were performed in triplicate. 100 µl of double-strength Müller-Hinton (MH) broth (Oxoid, Basingstoke, UK) was pipetted into columns of a microtitre plate. 200 µl of nanoparticle solution was placed in column 1 before 100 µl was removed and mixed with the MH broth in column 2. 100 µl was removed and added to column 3 and mixed. The process was repeated until column 11, at which point the nanoparticle-containing aliquot was discarded so to give both a positive and negative control. The microtitre plate was incubated for 24 hours at 37 °C before the turbidity of the solution was observed by eye. The lowest concentration that prevented bacterial growth (clear solution) was recorded as the MIC. The minimum bactericidal concentration (MBC) was determined by plating the broth solutions from the MIC test onto nutrient agar (Oxoid Ltd) and incubating at 37 °C in air overnight. The MBC was defined as the lowest concentration of nanoparticles that prevented bacterial growth on the agar surface.

To examine the bacterial growth rate and to determine the growth curve of *E. coli* (NCTC 25522) and *S. aureus* (8325-4) in the presence of the copper NPs. *E. coli*

and *S. aureus* was given in 100 μ l of BHI broth supplemented with 2, 1, 0.5, and 0.25 mg ml⁻¹. The growth rates were determined by measuring the optical density (OD) to 600 nm each 30 minutes for 10 hours. OD values were plotted against time to produce the growth curve.

3.3 Results and Discussion

Initially a range of single-source copper precursors were investigated to study which precursors deposited copper thin films reproducibly and with good coverage. Copper(II) acetylacetonate, $[\text{Cu}(\text{acac})_2]$, copper acetate, $[\text{Cu}(\text{OAc})_2 \cdot \text{H}_2\text{O}]$, and copper nitrate trihydrate $[\text{Cu}(\text{NO}_3)_2 \cdot 3\text{H}_2\text{O}]$ are readily available copper precursors for a single-source deposition of copper thin films and hence AACVD using these precursors under a range of conditions was investigated (Table 3-1).

Table 3-1: The results of using a variety of copper precursors, solvents, temperature and cooling gas.

	Copper Precursor	Solvent	Temp / °C	Cooling Gas	Film	Film Colour
A	<i>Copper Acetate,</i> $[\text{Cu}(\text{OAc})_2 \cdot \text{H}_2\text{O}]$	MeOH	350	N ₂	CuO/Cu ₂ O	Red, orange, black
B		MeOH	400	N ₂	CuO/Cu ₂ O	
C		MeOH	450	N ₂	CuO/Cu ₂ O	
D		Acetone	400	N ₂	Cu/Cu ₂ O	
E	<i>Copper(II) acetylacetonate,</i> $[\text{Cu}(\text{acac})_2]$	MeOH	350	N ₂	Cu	Metallic red/brown
F		MeOH	400	N ₂	Cu	
G		MeOH	450	N ₂	Cu	
H		MeOH	350	Air	Cu/Cu ₂ O	Orange/yellow
I	<i>Copper Nitrate,</i> $[\text{Cu}(\text{NO}_3)_2 \cdot 3\text{H}_2\text{O}]$	MeOH	350	N₂	Cu	Metallic red/brown
J		EtOH	350	N ₂	CuO/Cu ₂ O	Red/brown, yellow, black
K		MeOH	400	N ₂	Cu/Cu ₂ O	
L		MeOH	450	N ₂	Cu/Cu ₂ O	
M		MeOH	350	Air	Cu₂O	Yellow

A number of depositions were investigated (Fig. 3-6) with a change of precursor, solvent, temperature and cooling gas. All these factors can have an influence on the purity, coverage and reproducibility of the desired thin films.

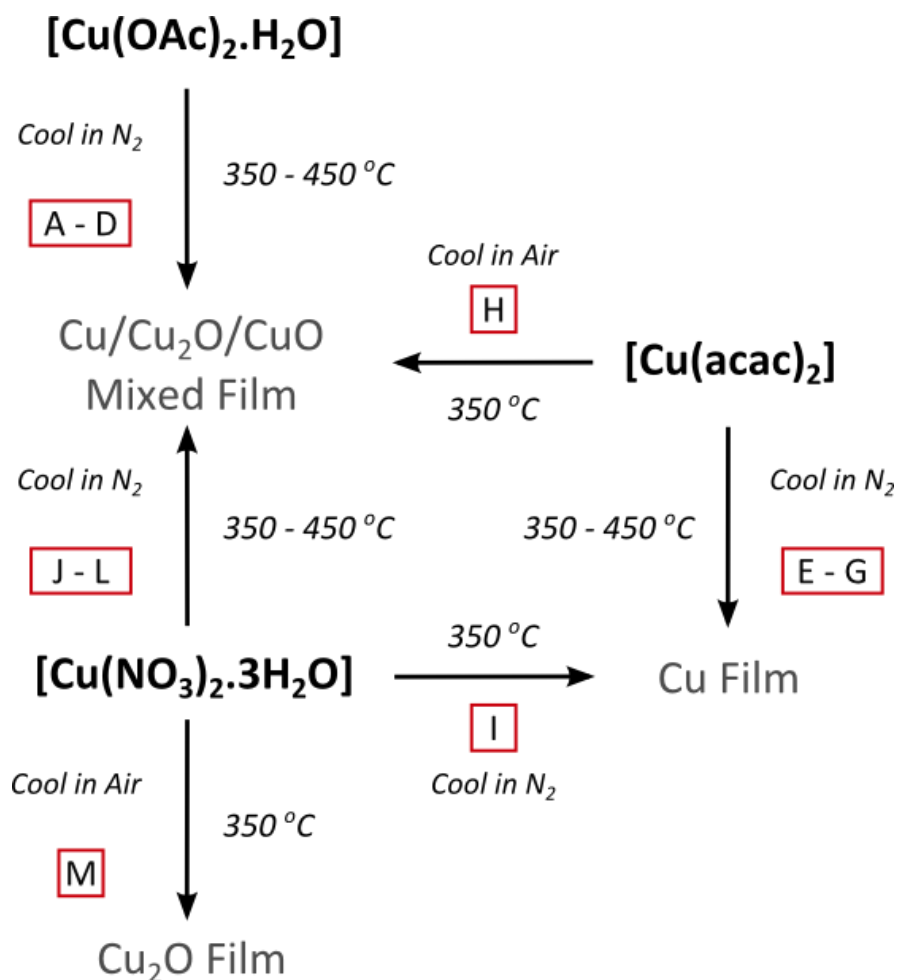


Figure 3-6: Scheme diagram of reaction conditions using different precursors.

Copper acetate, [Cu(OAc)₂.H₂O] was found to be soluble in both MeOH and acetone. AACVD of copper acetate in MeOH was carried out at over a range of temperatures (350 – 450 °C) and the substrate was allowed to cool to room temperature under nitrogen to produce a film. For all the temperatures investigated, a non-adhesive powdery film was produced consisting of red/brown, yellow and black areas. Powder x-ray diffraction (XRD) data identified that a mixture of Cu, CuO and Cu₂O formed (Fig. 3-7). The solvent was changed to acetone and similar results were seen. A non-adhesive mixture of Cu/Cu₂O was deposited.

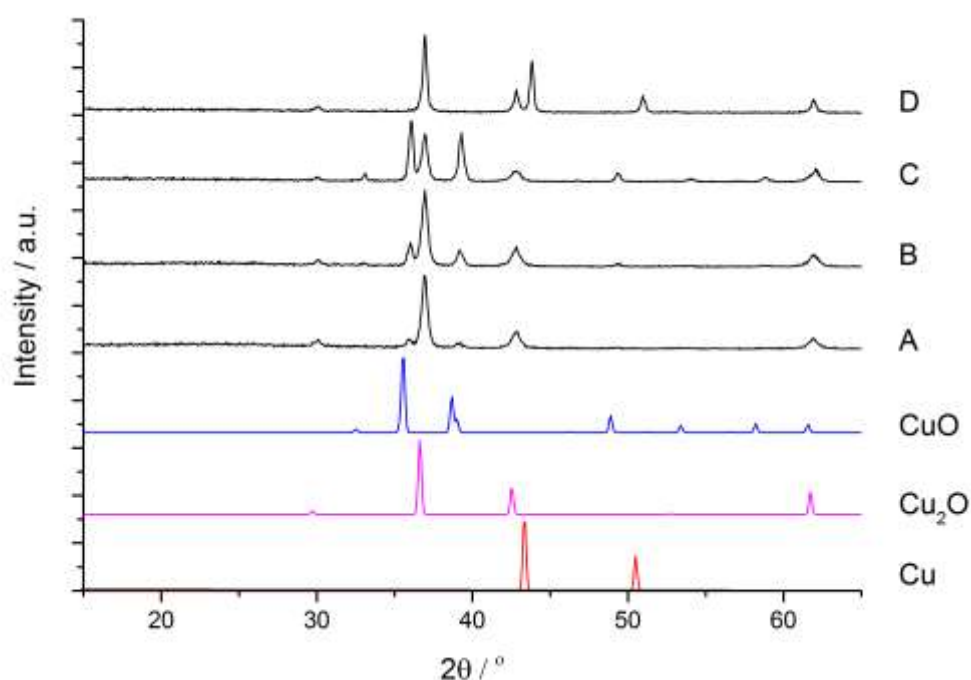


Figure 3-7: Powder XRD pattern of thin films deposited using copper acetate over a range of temperatures A) 350 °C, B) 400 °C, C) 450 °C in methanol and D) 400 °C in acetone with the Cu, Cu₂O and CuO XRD standards.

In order to attempt to overcome the formation of mixtures, an alternative copper precursor was investigated. Copper(II) acetylacetonate, [Cu(acac)₂] was added to a number of different solvents including methanol, ethanol, isopropanol and acetone. Methanol was chosen as the solvent for the AACVD experiment due to the copper precursor being more soluble in methanol compared to the other solvents. However, even after prolonged mixing in a sonicator, all of the [Cu(acac)₂] in MeOH did not dissolve in the solution. AACVD of [Cu(acac)₂] in MeOH was carried out at 350 – 450 °C and the substrate was allowed to cool to room temperature under nitrogen in an attempt to produce an adhesive copper film. Powder XRD data was used to verify that polycrystalline copper films were deposited at 350 and 450 °C. However, the highest temperature (450 °C) identified the presence of Cu and Cu₂O (Fig. 3-8). As the temperature increased, the film coverage decreased with the lowest temperature having the most coverage on the substrate. The deposition was repeated at 350 °C but the film was allowed to cool in air. This resulted in a film that was shown by powder XRD to be mixture of Cu and Cu₂O.

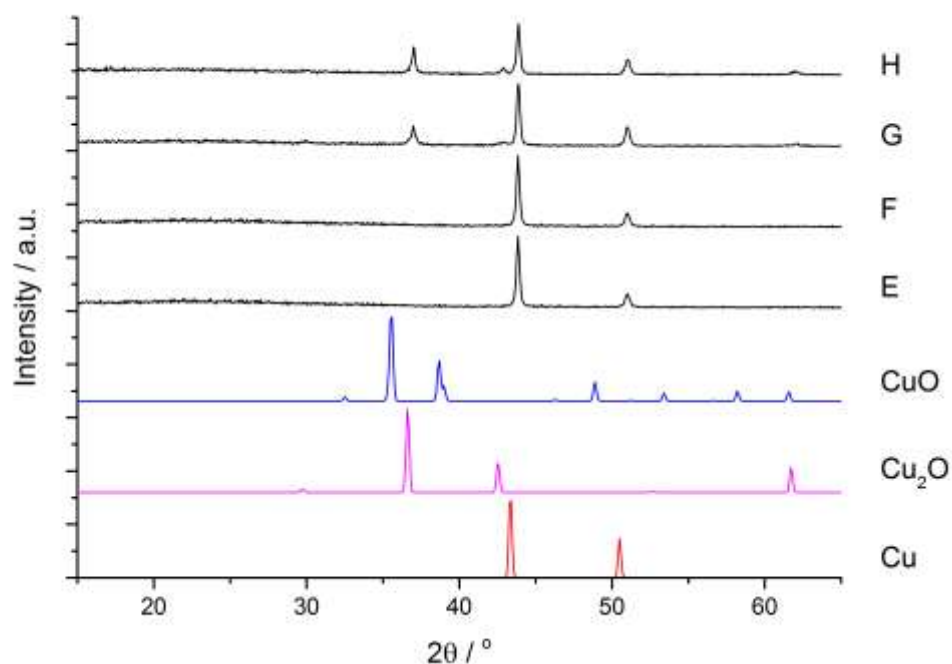


Figure 3-8: Powder XRD of thin films deposited using $[\text{Cu}(\text{acac})_2]$ in methanol at E) 350 °C, F) 400 °C, G) 450 °C and cooled under N_2 and H) filmed cooled in air with the Cu, Cu_2O and CuO XRD standards.

$[\text{Cu}(\text{acac})_2]$ as a copper precursor was not suitable because there were solubility problems, undissolved precursor remained in the AACVD bubbler at the end of the deposition. However, copper thin films were able to be deposited. Attempts at depositing Cu_2O films resulted in a mixture. Therefore, a further copper precursor was investigated in an attempt to deposit both Cu and Cu_2O without precursor waste. AACVD of copper nitrate, $[\text{Cu}(\text{NO}_3)_2 \cdot 3\text{H}_2\text{O}]$, dissolved in methanol was investigated under a range of conditions. The temperature of deposition was varied from 350 – 450 °C and a range of substrates were used to obtain the optimum parameters (Fig. 3-9).

AACVD of $[\text{Cu}(\text{NO}_3)_2 \cdot 3\text{H}_2\text{O}]$ in methanol resulted in the deposition of copper at 350 °C. At the end of the deposition, the film was relatively unstable and was readily oxidised. Therefore, in order to deposit pure Cu thin films, it was necessary to cool to room temperature under nitrogen. The film formed after cooling under nitrogen had a uniform coverage and was free from pin-hole defects. The film appeared to have a red/brown metallic colour. XRD measurements were performed which identified the presence of polycrystalline copper (Fig. 3-9). Using the same

conditions as previously described but allowing the as-deposited films to cool in air led to the formation of Cu_2O . The film deposited was uniform, yellow and transparent. The formation of cuprous oxide was confirmed by powder XRD, which showed the presence of polycrystalline Cu_2O .

AACVD of $[\text{Cu}(\text{NO}_3)_2 \cdot 3\text{H}_2\text{O}]$ in methanol at $400\text{ }^\circ\text{C}$ followed by cooling under nitrogen, resulted in a mix $\text{Cu}_2\text{O}/\text{Cu}$ film with good coverage. Powder XRD indicated that a mixture of copper and cuprous oxide had formed as shown in Fig. 3-9. In contrast, AACVD of $[\text{Cu}(\text{NO}_3)_2 \cdot 3\text{H}_2\text{O}]$ in methanol at higher temperature of $450\text{ }^\circ\text{C}$ resulting $\text{Cu}_2\text{O}/\text{CuO}$ film (Fig. 3-9L) and was confirmed by XRD. Elevated temperatures typically results in oxide formation ($\text{Cu}_2\text{O}/\text{CuO}$) with metallic copper films usually forming at lower temperatures. Using a different solvent, ethanol, resulted in a film with poor coverage and a mixture of copper oxides (Fig 3-9J).

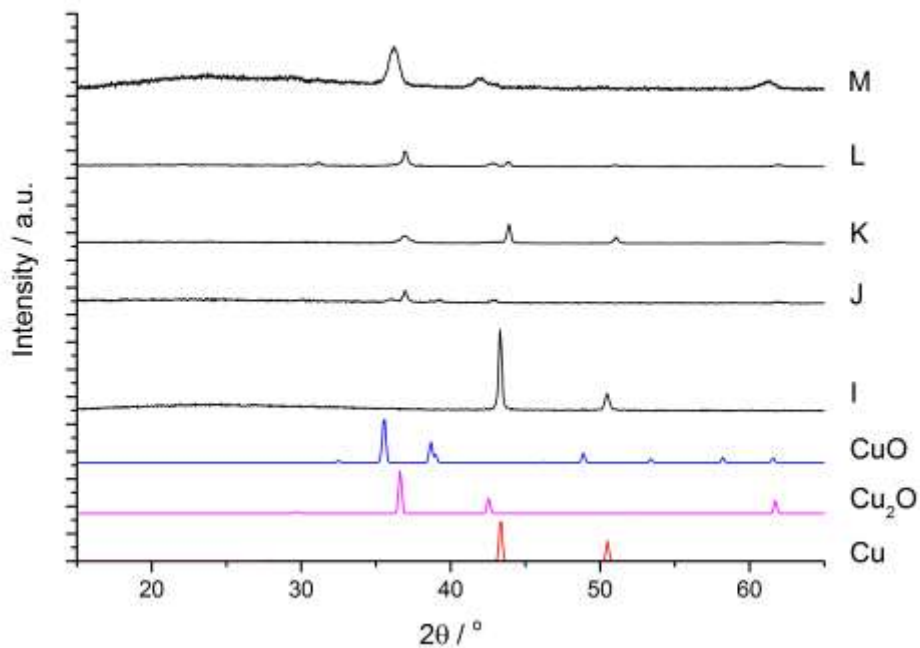


Figure 3-9: Powder XRD patterns of thin films deposited using $[\text{Cu}(\text{NO}_3)_2 \cdot 3\text{H}_2\text{O}]$ using I) methanol at $350\text{ }^\circ\text{C}$, J) ethanol at $350\text{ }^\circ\text{C}$ and methanol at K) $400\text{ }^\circ\text{C}$ and L) $450\text{ }^\circ\text{C}$, M) methanol at $350\text{ }^\circ\text{C}$ and cooled in air with the Cu, Cu_2O and CuO XRD standards.

The optimum parameters that were reproducible were reactions (I) and (M). All of the films were deposited onto float glass. However, for microbiology analysis copper needs to be deposited onto microscope slides. This brought up challenges whereby there were difficulties in successfully depositing copper onto slides with good coverage and free of pin-hole defects. Once the float glass was replaced with the microscope slides, the film had a tendency to oxidise. If copper did deposit onto the slide, it was not easily reproducible or the coverage was poor. This may be due to the AACVD rig not being completely air tight although, this did not affect the deposition when float glass was used as a substrate.

It has been suggested that the formation of the Cu and Cu₂O films in the AACVD reactor occurs in a reducing environment whereby the thermodynamic decomposition of [Cu(NO₃)₂.3H₂O] would produce Cu_xO.¹⁴¹

The most reproducible pure copper films were deposited at 350 °C. This suggests that there is a reducing environment since it has been reported that hydrogen is formed due to decomposition of methanol over a copper catalyst. The production of copper films using methanol was unexpected since it is used as an oxygen source to deposit metal oxide thin films. Copper films deposited using ethanol instead of methanol (reaction J) at 350 °C did not produce pure films. It has been shown that the formation of hydrogen from the decomposition of ethanol is less effective. Therefore methanol and substrate temperature of 350 °C is required for the deposition of pure copper films using [Cu(NO₃)₂.3H₂O].

Many attempts were made to deposit Cu onto microscope slides with good coverage. It was found that having the slides directly on the graphite heating block resulted in the best depositions when compared to depositions where slides were placed on top of float glass. This could be due to the aerosol mist not being disrupted and having a streamlined flow. However, the results were not always reproducible and oxidation could still occur even if there was good coverage.

The problem with the deposition can be attributed to surface reactions occurring. Glass is based on SiO₂ but it also contains many other oxides of elements such as B, Ca, Mg or S. There are major differences between the bulk and surface composition

of the glass. There tends to be a higher concentration of cations near the surface with the surface itself being made up with hydroxyl terminals. During the deposition, the hydroxyls form Si-OH bonds through the reaction of the surface SiO₂ with atmospheric water. The OH groups formed promote formation of hydrogen bonds between itself and water/organic liquid causing the surface to become wet. This could cause reactions between the water and the cation present near the surface leading to a migration of ions to the surface, which could damage the property of the films. To prevent diffusion of ions from the glass, float glass has a layer of SiO₂ applied to the surface, which acts as a barrier layer. The microscope slides do not have this barrier layer and therefore cause the problem of oxidation that has been seen. However, it was found that increasing the concentration of the solution enabled the as-deposited films to possess much better uniform coverage, and the deposition was reproducible.^{142,143} Therefore, 1g of [Cu(NO₃)₂·3H₂O] in 40 ml MeOH rather than 0.5 g used in the previously described depositions was used.

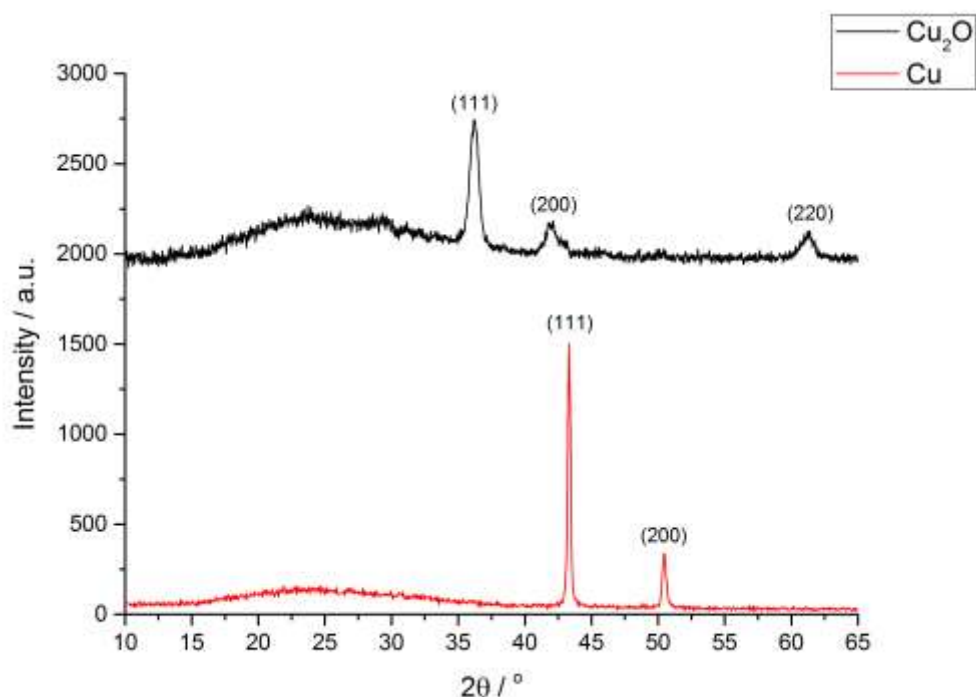


Figure 3-10: Thin films deposited using [Cu(NO₃)₂·3H₂O] at 350 °C either cooled under N₂ to form a) copper or cooled in air to form b) Cu₂O.

XRD patterns for the Cu and Cu₂O films deposited onto microscope slides from [Cu(NO₃)₂.3H₂O] produced uniform coverage. Powder XRD confirmed the presence of polycrystalline Cu peaks (Fig. 3-10) correspond to (111) and (200) planes whereas polycrystalline Cu₂O reflections correspond to the (111), (200) and (220) planes. The XRD measurements collected not only can be used for unit cell refinement to yield lattice parameters but a qualitative analysis of preferred orientation can take place. The Cu XRD (Fig. 3-10) showed an enhancement of the (111) plane whereas Cu₂O exhibit an enhancement in the (200) plane which may be related to some preferred orientation.

All films were uniformly deposited on the microscope glass substrate and all were well adhered to the substrate. The films remained attached after the use of Scotch™ tape, with damage only observed after scratching with a scalpel. The stability of the Cu and Cu₂O thin films were tested using different solvents. Both films were left unchanged and adhered to the substrate when wiped using water and acetone. However, when wiped using nitric acid, the films visibly looked damaged and began to remove from the substrate.

Powder XRD data was used to calculate the lattice parameters. The fitting process used the Le Bail model where refinement is limited to (HKL) lines defined by the cell and space group. General Structure Analysis System (GSAS) with EXPGUI, a graphical user interface editor was performed to control the progression of equally weighted fitting to obtain unit cell parameters. Lattice parameters, *a*, were calculated for Cu and Cu₂O films and compared with the literature values (Table 3-2). There is no significant difference between the refined and literature values of copper. However, there is a slight difference seen for the Cu₂O value. This suggests that there is an increase in the lattice parameters, which can be due to oxygen. The expansion has been observed previously for metal oxide thin films deposited on glass and can be caused by the interaction between the amorphous substrate and the crystalline film or by restricted particle size.¹⁴⁴

Table 3-2: Lattice parameter calculations of Cu and Cu₂O.

Film	Cu	Cu ₂ O
Lattice Parameter, a (Å)	3.62(6)	4.29(6)
Fitted wRp	0.067	0.0976
Literature Value	3.61 ¹⁴⁵	4.26(9) ¹⁴⁶

The morphology of the films was investigated using scanning electron microscopy (SEM), as shown in Fig. 3-10. There are many different ways a film can grow on the substrate during the AACVD process and the microstructure can have a major impact on the properties of the film.⁸¹ The SEM images of the copper films deposited onto microscope slides are shown in Fig. 3-12a and b. The microstructure consists of large particles ranging from 300–600 nm. This is consistent with a Volmer–Weber or Island Growth model (Fig. 3-11a).⁹⁴ This type of growth occurs when atoms experience stronger bonding interaction between themselves than with the substrate. Copper oxide films deposited onto microscope slides appear rougher with different particle sizes ranging from 100–600 nm. The SEM image corresponds to particulate growth where the particles have a stronger interaction with the substrate rather than to themselves (Fig. 3-11b).

Cross-sectional SEM was used to directly measure the film thickness of the deposited Cu and Cu₂O on microscope slides. (Fig. 3-12c and d). The copper and copper oxide films produced were relatively thick. The copper films range from 200–300 nm whereas the copper oxide film is much thicker with a larger range of 0.4–1 μm. Both films have a structure composed of particles ranging in sizes which can be related to the microstructure of the films.



Figure 3-11: Film growth model of a) Island growth and b) Particulate growth.

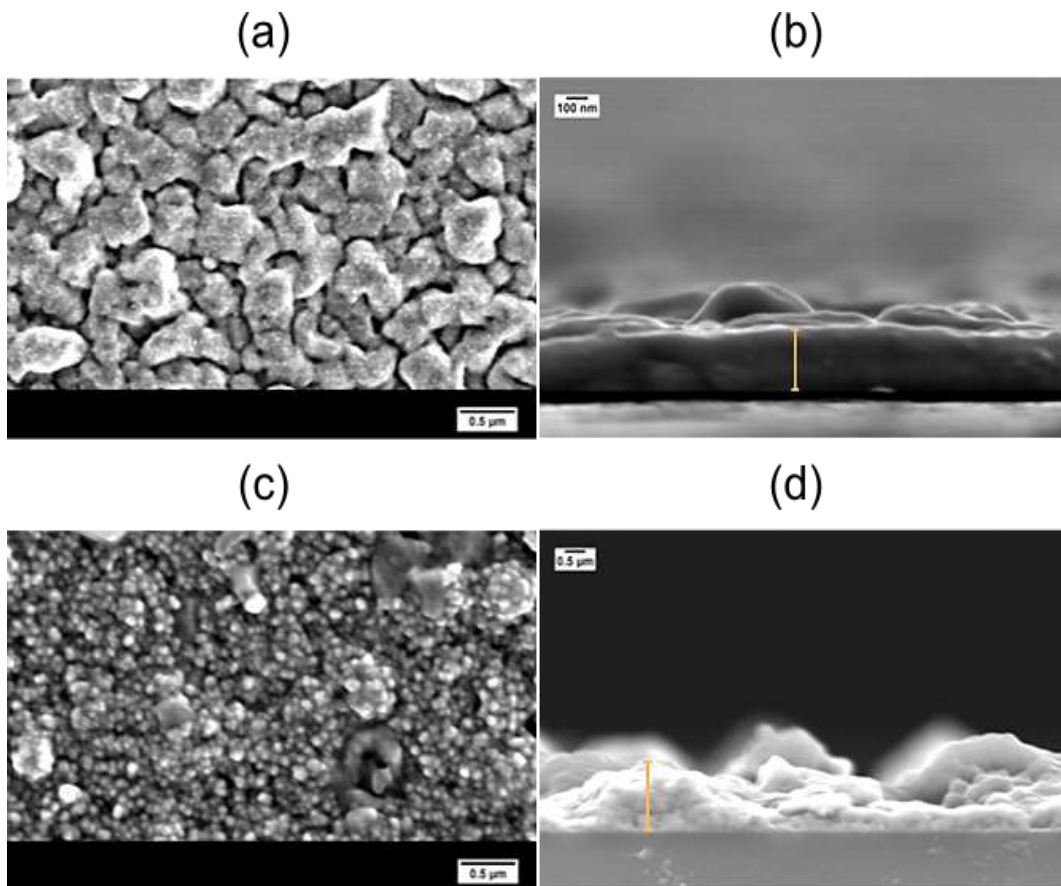


Figure 3-12: SEM micrograph of a) Cu film grown via AACVD of $[\text{Cu}(\text{NO}_3)_2 \cdot 3\text{H}_2\text{O}]$ in methanol at 350 °C and cooled under N_2 (Reaction I), b) Cu_2O film deposited from $[\text{Cu}(\text{NO}_3)_2 \cdot 3\text{H}_2\text{O}]$ in methanol at 350 °C and cooled in air (Reaction M). Side-on SEM of the c) Cu film and d) Cu_2O film.

3.4 Antimicrobial Activity of Copper and Copper(I) Oxide

The antimicrobial properties of the copper and copper oxide films, deposited from $[\text{Cu}(\text{NO}_2)_3 \cdot 3\text{H}_2\text{O}]$ via AACVD, against *E. coli* and *S. aureus* were investigated. Films were deposited onto microscope slides and cut in 1×1 cm sample sections. These sections were covered with 25 μL of bacterial cell suspension containing approximately 10^6 cfu. Serial dilution and spreading of the bacterial cell suspensions on to agar plate (MacConKey agar for *E. coli* and BHI agar for *S. aureus*) and subsequently incubated overnight at 37 °C. This resulted in viable counts of bacteria for each sample that was counted and recorded over a variety of exposure times. Mann Whitney U test were performed on the results of the antimicrobial testing, which showed that all the reduction in bacteria cell viability were highly significant ($P < 0.001$) for all exposure times.

The results for the copper films, shown in Fig. 3-13, demonstrated that the films have antimicrobial activity against *E. coli* and *S. aureus*. For *E. coli*, a 2.1- \log_{10} reduction in viable bacteria was observed after 15 minutes and 4- \log_{10} reduction was obtained after 30 minutes, as shown in Fig. 3-13a. In the case of *S. aureus*, a 2.7- \log_{10} reduction in viable bacteria was achieved after 30 minutes and 4- \log_{10} reduction was observed after 1 hour (Fig. 3-13b). For both bacteria, the copper films produced highly significant reduction of the bacterial cells when compared to the glass controls. These copper thin films deposited via AACVD have shown similar antimicrobial activity to previous research into copper coupons.^{147,148} Fig. 3-13c shows the antimicrobial activity of copper oxide against *E. coli* and *S. aureus*. The copper oxide samples tested against *S. aureus* gave a 2.7- \log_{10} reduction in viable bacteria after 45 minutes and a 4.7- \log_{10} reduction after 1 hour. In the case of *E. coli* the copper oxide films were less active giving a 1.2- \log_{10} reduction in viable count after 45 minutes and a 2.7- \log_{10} reduction after 1 hour.

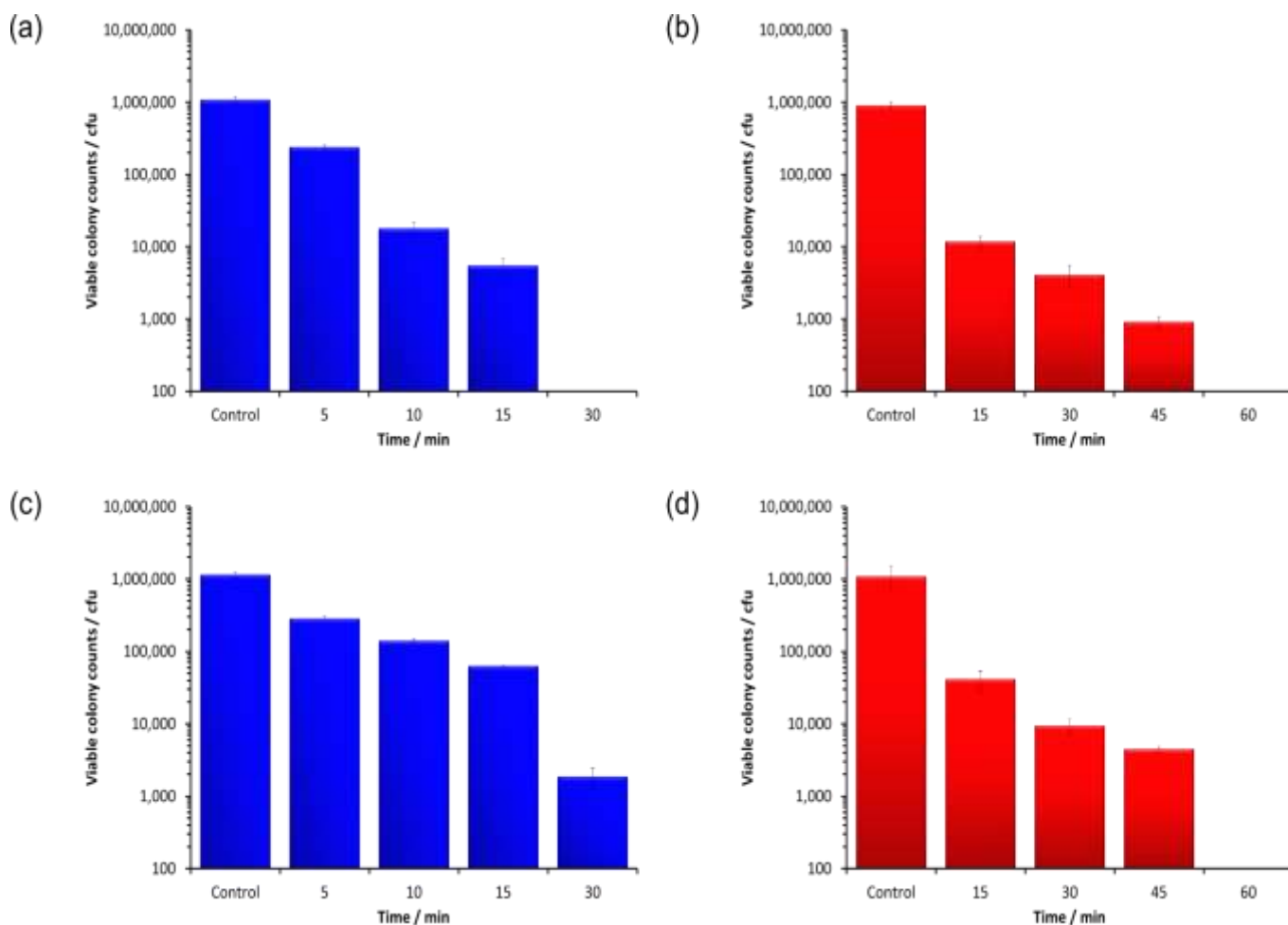


Figure 3-13: Viable colony counts of bacteria after incubation on Cu thin films tested against a) *E. coli*, b) *S. aureus* and viable counts of bacteria of Cu₂O against c) *E. coli* and d) *S. aureus*.

In the work described, the antimicrobial activity of copper was compared to copper(I) oxide in order to see if the oxidation would increase the antimicrobial effectiveness. Both samples were tested against *E. coli* and *S. aureus*. The results show that the two types of film have different antimicrobial efficacies against *E. coli* (gram negative) and *S. aureus* (gram positive). From the results presented, *E. coli* had lower bacterial cell counts when exposed to copper than to copper oxide, whereas with *S. aureus* similar levels of bacterial activity were observed with copper and copper(I) oxide films. The toxicity of the samples can be attributed to the release of copper ions under wet conditions. Studies have shown that copper ions play an important role in the toxicity of copper containing materials.⁷⁶ Some research has shown that particular strains of bacteria are more vulnerable to different copper

ions.¹⁴⁸ Previous reports have shown that the antimicrobial efficacy of Cu₂O approaches that of copper which is thought to be due to the fact that localised corrosion could lead to the release of Cu(I) ions.¹²⁷ Therefore, oxide formation on copper objects should not greatly impair the antimicrobial efficiency. The mechanism for copper materials toxicity are not fully understood currently but the results presented herein demonstrate the high antimicrobial activity of both copper and copper(I) oxide films deposited via AACVD.

A comparison of the results obtained in this study to other antimicrobial copper and copper oxide investigations is given in Table 3-3. The table indicates the results from this investigation were comparable to previous studies with similar inoculum concentration used. The antimicrobial effectiveness was either similar or better than previous investigations. The previous studies also show how oxidation of copper does not affect the antimicrobial activity.

Table 3-3: Results from copper and copper oxide against a range of activity from previous investigations.

Sample	Species	Time / min	Inoculum	Reference
Cu	<i>E. coli</i>	40 – 60	2 x 10 ⁷ cfu	S. W. J. Gould et al. ¹²⁴
	<i>S. aureus</i>	60		
Cu	MRSA	75	2 x 10 ⁷ cfu	H. T. Michels et al. ¹⁴⁹
Cu	<i>E. coli</i>	65	2 x 10 ⁷ cfu	J. O. Noyce et al. ¹¹⁷
Cu _x O	<i>E. coli</i>	80	10 ⁸ cfu/ml	H. M. Yates et al. ¹⁵⁰
	<i>S. epidermidis</i>	80		
Cu	<i>E. coli</i>	65	10 ⁷ cfu	S. A. Wilks et al. ¹¹⁴
Cu	<i>E. hirae</i>	300	10 ⁸ cfu	M. Hans et al. ¹³⁴
Cu ₂ O	<i>E. hirae</i>	300		
Cu	<i>E. coli</i>	30	10 ⁶ cfu	Our results
	<i>S. aureus</i>	60		
Cu ₂ O	<i>E. coli</i>	60		
	<i>S. aureus</i>	>60		

In order to investigate the films potential suitability for use in a healthcare setting, the antimicrobial longevity after cleaning was tested. The exposure times chosen were the longest times recorded that exhibited the highest bacterial reduction (one hour or 30 minutes). On the first day after serial dilution and plating was carried out, the samples were cleaned with alcohol (70%) and left to dry. This was repeated a further two times over a week. These results showed that the reduction in viable bacteria counts was maintained over the seven day testing period and the antimicrobial activity of the films did not significantly change when they were repeatedly cleaned and retested used. After the initial testing on day one, the reduction of *E. coli* and *S. aureus* was affected and there was a reduction in the rate. However, the bacterial efficacy still remained highly significant, as shown in Fig. 3-14. HAI bacteria, such as *E. coli* and *S. aureus*, can potentially survive on touch surfaces for days even though cleaning procedures are used by healthcare workers'. The Cu and Cu₂O thin films, however, have demonstrated the ability to maintain the reduction in bacterial cell viability over a seven day period.

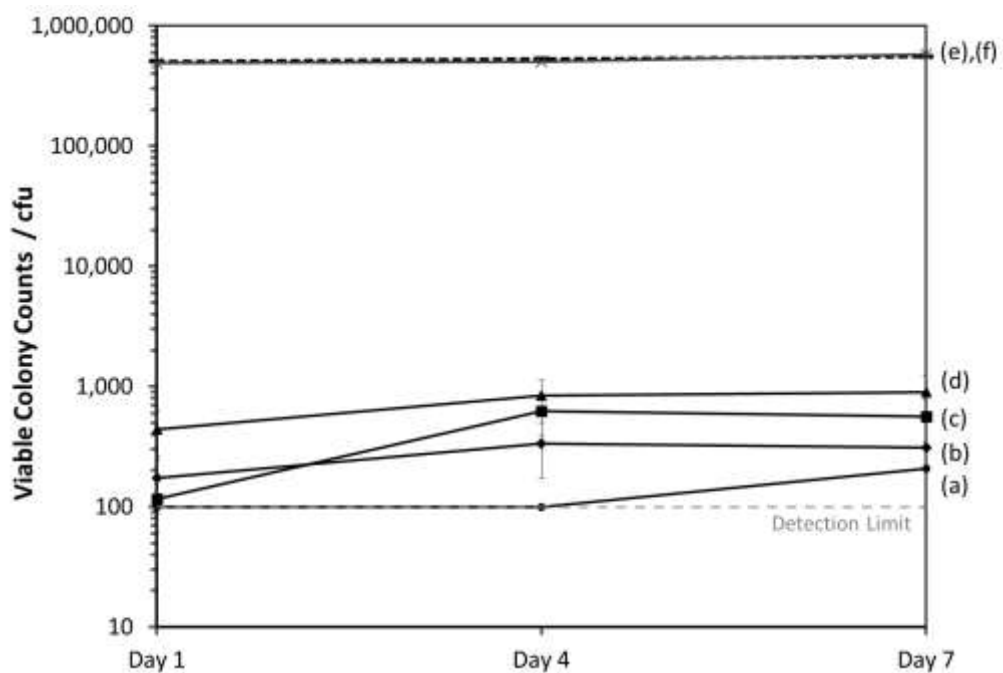


Figure 3-14: Viable counts of bacteria after incubation on Cu and Cu₂O thin films tested three times over 7 days. a) Cu and b) Cu₂O were tested against *S. aureus* (1 h incubation). c) Cu and d) Cu₂O against *E. coli* (30 min or 1 h incubation respectively). The glass control tested against e) *E. coli* and f) *S. aureus* (1 h incubation).

3.4.1 Results and Discussion

The antimicrobial activity of the nanoparticles dispersed in cultures of *E. coli* (NCTC 25522), *S. aureus* (8325-4), *P. aeruginosa* (PA01) and *E. faecium* (E1162) was investigated by determining the minimum inhibitory concentration (MIC) and minimum bactericidal concentration (MBC). These are defined as the minimum concentration of material that inhibits the growth of bacteria and the lowest concentration of bactericidal agent that kills 99.9% of bacteria.

In order to determine the MIC, the NPs were dispersed into bacterium suspended in PBS solution to a broth concentration of 10^6 cfu ml⁻¹. The concentration of the copper and the oxidised copper NPs range between 0.5 – 2 mg ml⁻¹. This was determined by serial dilution (see chapter 2) in a microtitre plate. The NPs were tested against gram negative (*E. coli* and *P. aeruginosa*) and gram positive (*S. aureus* and *E. faecium*). Ranges of NP concentration were achieved through serial dilution and incubation of the microtitre plate for 24 hours at 37 °C. Inhibition of bacterial growth will result in clear suspension. However, bacterial growth will cause the solution to be cloudy. The turbidity of the solution was recorded. The lowest concentration of the NPs that maintain the clear suspension is the MIC.

There are different ways the Cu NPs, the antimicrobial agents, can affect the bacterial growth. The NPs can be described as bacteriostatic or bactericidal. Antimicrobial agent can be cidal, which will kill all the microbes whereas static means they inhibit growth of microbes but do not kill the existing cells. Figure 3-15 shows how viable colony counts can be affected with bacteriostatic or bactericidal antimicrobial agents. With the addition of bacteriostatic agent, the number of viable bacteria cell remains constant. However, the addition of bactericidal agent causes the viable bacterial cells to drop rapidly as the antimicrobial agent kills the microbial cells.¹⁵¹

A range of concentrations of NPs was achieved through the serial dilution of an initial solution until there was no inhibition on bacterial growth. The MIC of the Cu NPs for both *S. aureus* and *E. faecium* was observed to be 0.5 mg ml⁻¹. Whereas, the MIC for *E. coli* and *P. aeruginosa* was 1 mg ml⁻¹. For all, samples the MBC was the

same as the MIC except for *E. faecium*. This suggests that the nanoparticles may act in a bactericidal manner where the bacteria would be killed in the presence of copper NPs rather than just having their growth inhibited (Table 3-4).

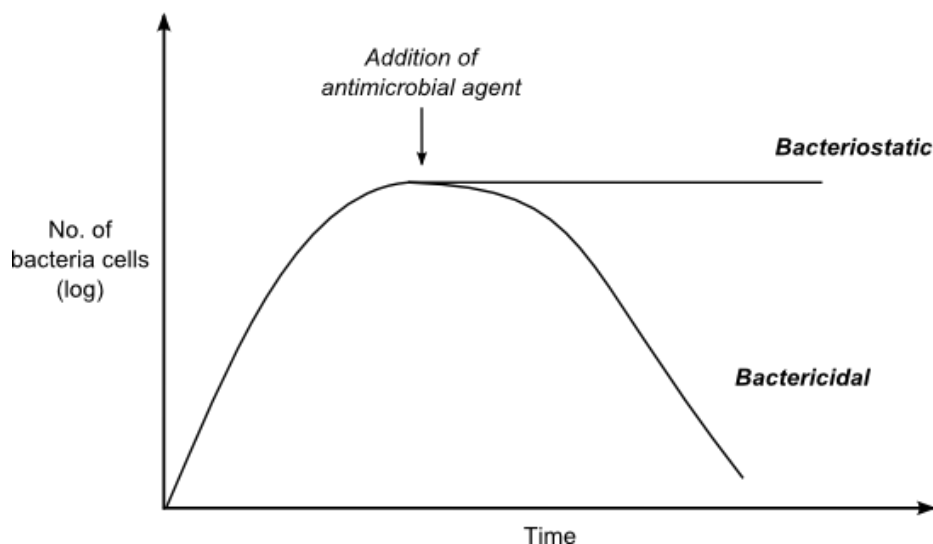


Figure 3-15: Diagram showing the difference in growth between bacteriostatic and bactericidal antimicrobial agents.

Table 3-4: Minimum inhibitory and bactericidal concentrations for copper and copper oxide nanoparticles against gram positive and gram negative bacteria strains.

	MIC ($\mu\text{g ml}^{-1}$)		MBC ($\mu\text{g ml}^{-1}$)	
	Cu NPs	Cu _x O NPs	Cu NPs	Cu _x O NPs
<i>E. coli</i> (NCTC 25522)	1000	1000	1000	1000
<i>P. aeruginosa</i> (PA01)	1000	1000	1000	1000
<i>S. aureus</i> (8325-4)	500	500	500	1000
<i>E. faecium</i> (E1162)	500	1000	1000	1000

The concentrations required to show an inhibitory and bactericidal effect on the bacteria found in these experiments are higher than in much of the reported work. Samples of copper NPs of a similar diameter to those produced in this work were shown to exhibit an MIC and MBC of 0.140 - 0.28 mg ml⁻¹ and 0.16 – 0.30 mg ml⁻¹ respectively, depending on the strain of *E. coli* used. However, this work used particles without stabilisation and initial bacterial concentrations of 10³-10⁴ cfu ml⁻¹ whereas in our experiments, initial concentrations of bacteria were higher at 10⁶ cfu ml⁻¹.

Table 3-5: Table of MBC values of copper and copper oxide NPs from previous investigations.

Nanoparticle	Bacterial Strain	MBC (µg ml ⁻¹)	Inoculum (cfu ml ⁻¹)	Reference
Cu	<i>E. coli</i>	250	5 x 10 ⁷	G. Ren et al. 128
	<i>S. aureus</i>	1000		
	<i>P. aeruginosa</i>	2500		
Cu_xO	<i>E. coli</i>	250 – 500		
	<i>S. aureus</i>	2500		
	<i>P. aeruginosa</i>	2500 - 5000		
Cu	<i>E. coli</i>	160 - 300	10 ³ - 10 ⁴	J. P. Ruparelia et al. 152
	<i>S. aureus</i>	160		
CuO	<i>E. coli</i>	103	10 ⁵ - 10 ⁶	V. V. T. Padil et al. 153
	<i>S. aureus</i>	120		
Cu	<i>E. coli</i>	30 - 95	10 ⁶	A. Azam et al. 154
	<i>S. aureus</i>	32 - 100		
	<i>P. aeruginosa</i>	35 - 85		

The MIC of the copper NPs may be affected by the oxidation process that occurs over the course of the experiment. It has been seen that copper oxide NPs need a higher concentration to achieve bactericidal effect when compared to copper NPs. The

results in this investigation have shown that the Cu_xO nanoparticles had similar MIC and MBC to the Cu NPs suggesting that the oxidation has little effect on these NPs.

The most likely explanation for the higher concentrations of the NPs required to achieve a bactericidal effect in this work is the much higher concentration of bacteria used in our work.

In further experiments, strains of gram negative (*E. coli*) and gram positive (*S. aureus*) bacteria were incubated in Müller-Hinton broth media supplemented with copper NPs. The growth rate of the bacteria were monitored up to 10 hours to investigate how the presence of NPs can affect the different stages of bacterial growth. There are different phases of growth of bacteria in a liquid medium; lag phase, log phase, stationary phase and death phase (see Fig. 3-14).

This inhibition of the growth of the bacteria is expected for concentrations on or below the MIC. Concentration on or above the MBC, complete kill of bacteria cells was observed in the growth curves. This inhibition in growth from antimicrobial agents has been seen previously. The initial lag phase occurs during the first two hours where the *E. coli* bacteria are adapting to the environment. This is followed by the log phase, which is a period of rapid duplication of bacteria leading to exponential growth. The third period is the stationary phase where the graph starts to plateau due to the rate of multiplication being equal to the rate of death. Similar growth curve was also seen for *S. aureus*.

The initial lag phase for the bacteria grown in the presence of NPs is seen to cause a delay in the initial lag phase when compared to the control. An inhibition of growth and reproduction of bacteria cells was observed. The NPs have caused a delay in the cells adapting to the new environment and allowing cells to prepare for exponential growth. For *E. coli* (Fig. 3-16), the Cu NPs have an additional 90 minutes delay (inhibition) to start the lag phase when compared to the control curve. Whereas, the growth of *S. aureus* in the presence of NPs (Fig. 3-17) has a delay at the start of the lag phase for 210 minutes when compared to the control. This inhibition in growth of bacteria has been seen previously.^{128,152}

For *E. coli*, with Cu NPS concentrations above the MIC (0.5 and 0.25 mg ml⁻¹) bacteria were able to grow (Fig. 3-16). The Cu NPs were able to inhibit their growth for four hours. However, for *S. aureus* only Cu NP concentration, of 0.25mg ml⁻¹ were they able to grow (Fig. 3-17). The Cu NPs were able to inhibit the growth for a longer period of time of over 6 hours

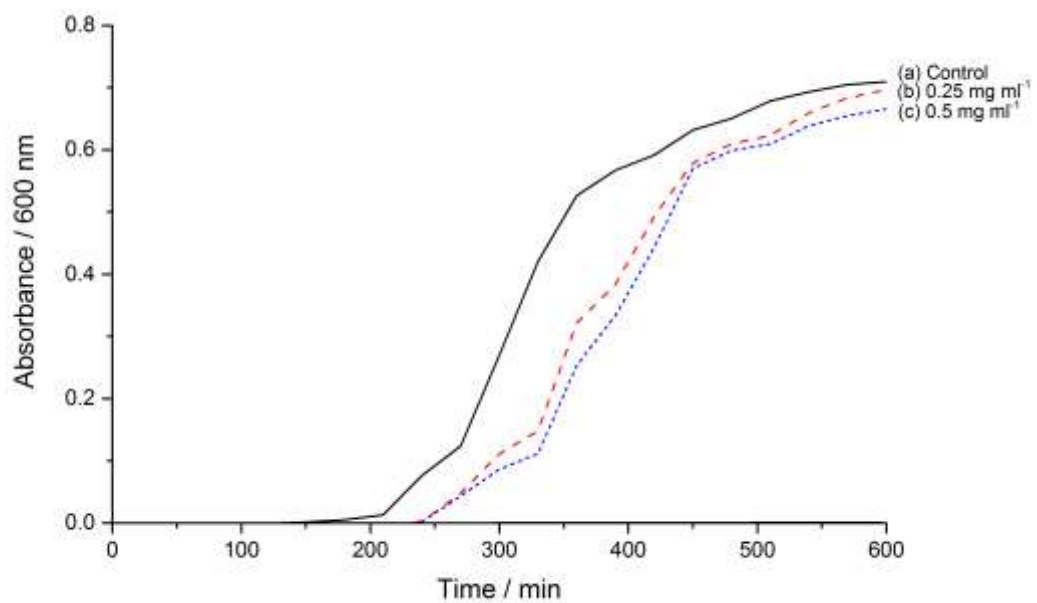


Figure 3-16: Growth curve of *E. coli* cells grown with differing concentrations of Cu NPs.

Table 3-6: Generation time calculated during the log phase for the *E. coli* growth curve

Growth Curve	Generation Time / min
Control	35
0.25 mg ml ⁻¹	50
0.5 mg ml ⁻¹	50

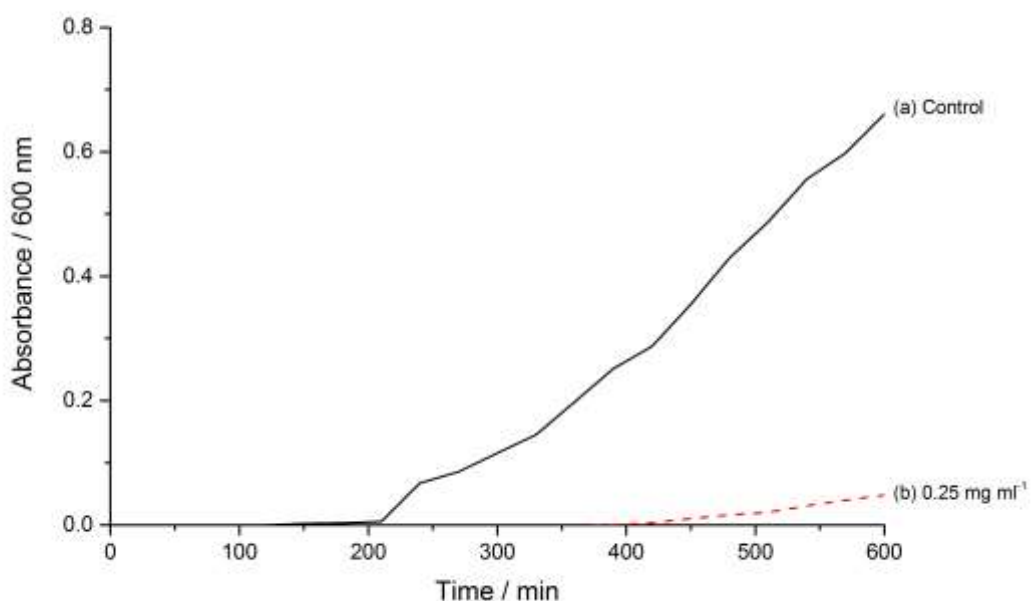


Figure 3-17: Growth curve of *S. aureus* cells grown with differing concentrations of Cu NPs.

Usually, serial dilution and viable colony counts at 30 minute intervals are necessary to calculate the colony forming counts (cfu). However, the optical density (OD) can be used as an indication of increasing bacterial cell density which is proportional to the cell population. Two points (0.2 and 0.4) on the optical density scale were chosen to represent the doubling of cell numbers (turbidity). The generation time was only calculated for *E. coli* with the Cu NPs. This is due to the fact that the *S. aureus* growth curves had not reached the log phase after 10 hours.

The generation time calculated for the control curve for *E. coli* is 35 minutes. This indicates that in the control it takes 35 minutes for *E. coli* growth was 35 minutes to double in cell mass. With the inclusion of Cu NPs in the growth of *E. coli* at concentrations of 0.25 mg ml⁻¹ and 0.5 mg ml⁻¹, the generation time increased to 50 minutes. This indicates that the inclusion of the Cu NPs has increased the time it takes the *E. coli* mass to double, therefore decreasing the growth rate.

3.5 Conclusion

The antimicrobial efficacy and repeatability of copper and copper(I) oxide thin films deposited via AACVD using $[\text{Cu}(\text{NO}_3)_2 \cdot 3\text{H}_2\text{O}]$ in methanol at 350 °C either cooled under nitrogen or air were investigated. This thin film technique is a simple and industrially scalable process. An advantage of AACVD is the ability to deposit on a wide range of substrates including the commonly used materials on touch surfaces in hospitals, such as stainless steel. We examined the antimicrobial activity of copper and copper(I) oxide films against *E. coli* and *S. aureus*. The antimicrobial activity of both copper and copper(I) oxide showed a highly significant reduction in viable bacterial counts. The results indicate that antimicrobial effectiveness is not reduced when copper is oxidised. The results have also shown that after repeated cleaning and testing over seven days the activity of the thin films is still highly significant. Further studies would involve quantifying the release of copper ions from the films, as well as investigating the impact of morphology on antimicrobial activity.

The MIC and MBC of Cu NPs were tested against a range of bacteria and found to have a MIC and MBC of 0.5 – 1 mg ml⁻¹. These values are higher than expected due to the high concentration of initial bacterial suspension. The growth curve of the Cu NPs was carried out over 10 hours against *E. coli* and *S. aureus*. It was seen that Cu NPs concentration was below the MIC concentration. However, the Cu NPs were able to inhibit the growth between 4 – 6 hours.

4

Indium Oxide and Gallium Oxide

The following chapter presents the results obtained from the deposition of indium oxide and gallium oxide thin films and investigating the different properties of the films. The thin films materials were fully characterised and the transparent conducting properties of indium oxide were investigated whereas the gallium oxide films were tested for their antimicrobial properties using serial dilution and viable colony counts on to agar plates.

4. Introduction

There has been a lot of interest in thin films of group 13 metal oxides. In this chapter we will be looking at indium oxide and gallium oxide and exploring their different properties. Indium oxide (In_2O_3) and gallium oxide (Ga_2O_3) were deposited using methanol as an oxygen source as well as a solvent. In_2O_3 is a transparent conducting oxide (TCO) and these properties will be explored. The antimicrobial activity of Ga_2O_3 was also investigated.

4.1 Transparent Conducting Oxides

TCOs are found in a wide range of applications that require materials to be conductive and transparent in the visible region of light. Therefore, the TCO material must have a band gap >3.2 eV (< 380 nm). There is enormous interest in increasing the conductivity of existing TCOs or identifying alternatives. TCOs are typically composed from doped or undoped semiconductors and combine the ability of high electrical conductivity and high optical transparency. The standards of TCO are to transmit $>85\%$ of visible light and have a high electrical conductivity ($<10^{-4}$ Ωcm).¹⁵⁵⁻¹⁵⁹

The most widely used and developed TCO is indium-tin-oxide (ITO). It is used as a standard for TCOs in industry. ITO is made from the doping of tin into indium oxide. The Sn^{4+} cations replace the In^{3+} ions resulting in an overall positive charge imbalance. This results in more electrons being available in the conduction band (n-type doping). The conductivity of the ITO improves due to the higher concentration of charge carriers.^{160,161,157}

Conductivity is reliant on the mobility of the charge carriers and in order to improve the electrical conductivity, the mobility of the charge carriers must increase. Charge carriers are dependent on the number of defects in the film. The defects affect the effective mass of the charge carriers and a reduction in the number of defects will decrease the effective mass resulting in higher carrier mobility. Materials that possess high levels of doping reduce carrier mobility that

in turn decrease film transparency due to more charge scattering from ionised impurities.

On account of these properties, TCOs can be found in optoelectronic devices such as flat panel displays and photovoltaic cells.¹⁶² A range of metal oxides can be used as TCO such as In_2O_3 , ZnO and SnO_2 .¹⁶³⁻¹⁶⁵ To improve the properties of the TCO materials, doping of the metal oxide is carried out to yield highly conductive thin films. These are examples of n-type TCOs where the conductivity is attributed to shallow donor states located near the conduction band, which are far superior to the p-type TCOs that produce poorer materials. In order to improve the conductivity of TCOs, the mobility of the charge carriers must be increased.¹⁵⁵ This depends on the number of defects present in the film. The selection of appropriate dopant is based on the knowledge of band structure for the metal oxide material.

4.1.1 Band theory of solids

Indium oxide, gallium oxide and zinc oxide (chapter 5) are examples of semiconductors, which falls between an insulator and a conductor. For a semiconductor, the electrical conductivity increases as the temperature increase. This is due to possessing a small enough band gap between the valence band and conduction band that thermal excitation can bridge the gap. The conductivity of a material relies on the delocalised valence electrons.

The position of the Fermi level is important and influences the conductivity of a material. The Fermi level is defined as the highest occupied orbital at absolute zero ($T=0$). When the valence band is not completely full and the fermi level is close enough, electrons can be promoted to the empty levels. This will result in a movement of electrons and the material is an electrical conductor.

There are different types of semiconductors; intrinsic, n-type and p-type. An intrinsic semiconductor, such as silicon, is shown Fig. 4-1b. The Fermi level lies in between the bands and the band gap is small enough for thermal energy to promote electrons to the upper band. This leaves positive holes (an absence of electrons) in the valence band that results in the material being conductive.

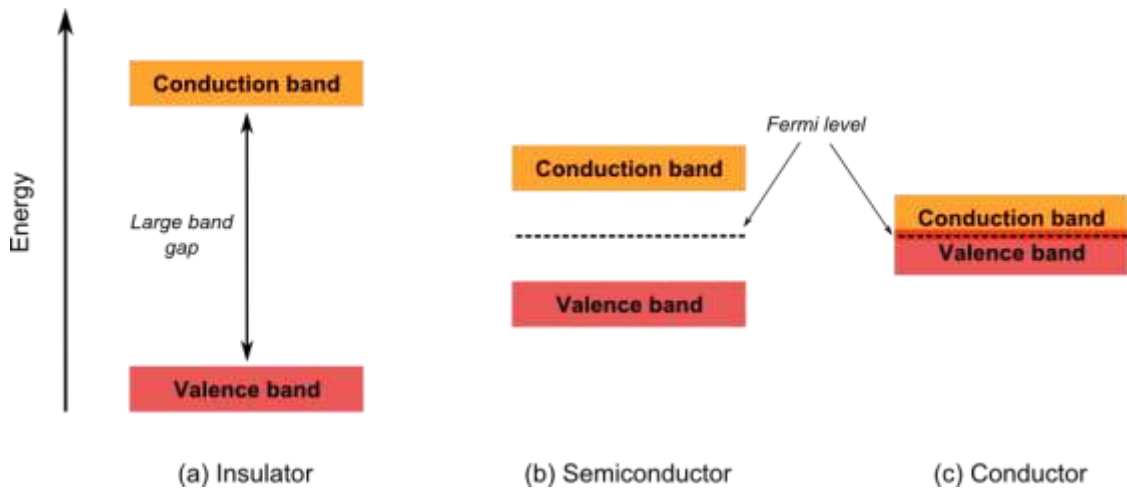


Figure 4-1: Energy band theory for solids.

The Fermi level position can be altered with the addition of dopants in the form of electron holes or excess electrons producing p-type and n-type semiconductors. If a material has an addition of impurities, which contributes to the number of electrons (e.g. Sb and P) the Fermi level is raised towards the conduction band. This greatly increases conductivity due to the extra electrons being easily excited into the conduction band, hence these are n-type semiconductors (Fig 4-2a). If a material has an addition of impurities (e.g. Al and Ga) that provide ‘positive’ holes (electron acceptors) to the material, it is a p-type semiconductor. This lowers the fermi level towards the valence band allowing electrons to be mobile, which increases conductivity (Fig. 4-2b).

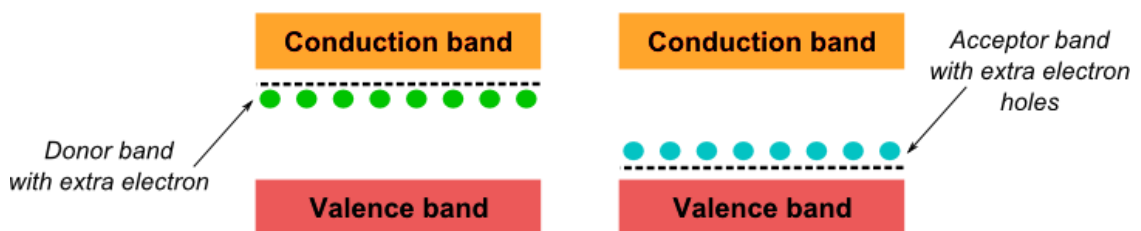


Figure 4-2: Doping of n-type and p-type semiconductors.

4.1.2 Indium oxide

Indium oxide (In_2O_3) is a wide band gap, n-type semiconductor, which usually have a cubic bixeyte structure. In_2O_3 can easily be doped with other metals to enhance the properties of the films. Unlike Ga_2O_3 , In_2O_3 is an electrical conductor at room temperature and transparent in visible light therefore are commonly used as TCOs. A direct band gap of In_2O_3 has been widely stated to be ~ 3.7 eV however, a weaker absorption at ~ 2.6 eV (indirect band gap) has also been observed that is associated with defects.^{166,167}

4.1.3 In_2O_3 deposition

There are a variety of different deposition techniques that can be used to deposit In_2O_3 ranging from sputtering, CVD and screen printing. Previous investigations have used InCl_3 as an Indium precursor via spray pyrolysis or alternative CVD process such as ultrasonic spray CVD. Extensive research has been carried out in synthesising single-source precursor to deposit In_2O_3 usually using indium alkoxides, $[\text{R}_2\text{In}(\text{OR}')]_2$, $\text{R} = \text{Me}, \text{Et}$; $\text{R}' = \text{CH}_2\text{CH}_2\text{NMe}_2, \text{CH}_2\text{CH}_2\text{OMe}$. However, the precursors can be air or moisture sensitive. In this investigation we deposit In_2O_3 in a single step process via AACVD.^{168,169}

4.1.4 Gallium oxide

Gallium oxide (Ga_2O_3) which crystallizes primarily in the monoclinic β crystal structure, has high chemical stability, and is thermally stable (melting point approximately 1900 °C). While being an electrical insulator at room temperature, Ga_2O_3 becomes semiconducting above 500 °C.^{169,170} This wide band gap semiconductor material, having the ability to operate at higher temperatures, presents a potential practical application as a gas sensor. At higher temperatures, (> 900 °C) its electrical conductivity is reliant on the concentration of oxygen, thereby it is able to measure the proportion of oxygen levels in a system. At lower temperatures (> 500 °C), Ga_2O_3 thin films acts as a surface-control-type sensor to

reducing gases. Therefore, it may be feasible to adjust the function of the gas sensor from reducing gases to oxidizing gases with temperature when using Ga_2O_3 .¹⁷¹⁻¹⁷³

Gallium is a semi-metallic element that is normally inert. The main application for gallium (Ga^{3+}) is as a semiconductor, such as gallium arsenide and gallium nitride. Gallium is not known to have any biological role due to its low bioavailability. However, gallium has demonstrated harmful effects on microorganisms, particularly in mechanisms involving the metabolism of iron.¹⁷⁴

Gallium has been used in biological studies despite having no known physiological functions in the human body. The mechanism for the antimicrobial activity of gallium (Ga^{3+}) is due to its ability to mimic iron (Fe^{3+}) but not to participate in redox reactions. Gallium is able to compete with iron and interferes with the absorption and activity of Fe^{3+} . Iron is important for cell division and essential for the formation of DNA. Therefore disruptions in the absorption of iron can cause the cells not to be able to produce sufficient DNA for replication, which ultimately leads to its death.¹⁷⁴⁻¹⁷⁶

Iron is a vital metal used in quaternary proteins containing heme molecules such as haemoglobin, and myoglobin. Iron also plays an important role in forming iron-sulphur (Fe-S) clusters inside proteins that catalyse a wide range of biochemical reactions and pathways. Any kind of disruption of these proteins and reactions can cause a shutdown in a number of cellular operations. Cytochrome is a metalloenzyme (protein containing a metal ion) that is important as it facilitates the transfer of electrons acquired from reduced molecules. Some microorganisms use different species as electron donors (e.g. Fe^{2+} , H_2) and electron acceptors (e.g. Fe^{3+} , SO_4^{2-}).¹⁷⁶

The poor solubility of iron materials causes a low dissolved concentration of Fe^{3+} ($\sim 10^{-10}$ mol/L).¹⁷⁶ This leads to iron becoming a limiting factor for growth of microorganisms. To overcome this, bacteria and fungi excrete organic compounds known as siderophores. Siderophores are Fe^{3+} scavengers due to their solubility and have ligands that act as reactive sites that bind to Fe^{3+} cations.¹⁷⁶⁻¹⁷⁹

Gallium with a trivalent charge (Ga^{3+}) has an ionic radius of $\sim 0.55 \text{ \AA}$ that corresponds well with Fe^{3+} ($\sim 0.5 \text{ \AA}$). This can allow Ga^{3+} to displace Fe^{3+} in biochemical molecules and pathways. However, iron is redox active but gallium is not. Therefore, the substitution of Fe^{3+} with Ga^{3+} will lead to the inactivation of Fe-dependent biomolecules.

Gallium is Food and Drug Administration (FDA) approved for intravenous administration. Studies carried out in the 1960s, demonstrated the ability of radioactive gallium (^{67}Ga) at high concentration to target tumour cells. This has developed to a ^{67}Ga scan that is used as imaging and detection for tumours and cancers. ^{67}Ga has been seen to be most useful in the detection of viable lymphomatous tumours in Hodgkin's and non-Hodgkin's lymphoma.¹⁸⁰⁻¹⁸²

The ability of ^{67}Ga has led to an increased investigation into antitumor potential of gallium. Studies carried out in 1970s compared toxicity of group 13 (trivalent cations) including gallium, aluminium, and indium. This research showed gallium nitrate had the highest antineoplastic activity towards tumours and was also the least toxic.^{183,184}

The National Cancer Institute (NCI) continued research into the antitumor effectiveness of gallium nitrate in Phase 1 and Phase 2 clinical trials. Two different clinical trials used gallium nitrate administered using two arrangements; a constant intravenous infusion given over 24 hours for 5 – 7 days or short intravenous infusion over 15 – 30 minutes.^{180,185-187}

Antimicrobial activity of gallium has been demonstrated with *in vitro* investigation of gallium in the form of gallium maltolate^{188,189} and gallium nitrate.^{190,191} Studies have shown that gallium nitrate can inhibit the growth of biofilms. Biofilms were grown in the presence and absence of low concentration of gallium nitrate and it was observed that limiting the presence of Fe in the nutrients had a positive correlation with the concentration of Ga and microbial reduction was observed. However, when Fe was introduced into the medium, competition between the Ga^{3+} and Fe^{3+} occurred causing the antimicrobial activity of Ga to decrease.^{192,193}

Gallium oxide (Ga_2O_3) is a potential source of Ga ions and investigations into the antimicrobial activity of Ga^{3+} were carried out using Ga_2O_3 -doped phosphate-based glasses (PBGs). PBGs are durable materials used as wound dressings where antibacterial ions such as copper and silver are incorporated. This unique system would be able to deliver Ga^{3+} as the glass degrades. The tests demonstrated that the PBGs had antibacterial effects on different HAI bacterial agents. Results indicated that 1% mol Ga_2O_3 -doped was sufficient to be potent against a range of organisms tested. Investigation on Ga_2O_3 nanoparticles have shown that they interfere with the adhesion mechanism of bacterial strains. This could reduce the formation of biofilms.¹⁹⁴

4.1.5 Ga_2O_3 deposition

Ga_2O_3 can be easily deposited using aerosol assisted chemical vapour deposition (AACVD). *In situ* reaction of $[\text{Ga}(\text{NMe}_2)_3]_2$ or GaR_3 and ROH ($\text{R} = \text{CH}_2\text{CH}_2\text{NMe}_2$, $\text{CH}(\text{CH}_2\text{NMe}_2)_2$, $\text{CH}(\text{CH}_3)\text{CH}_2\text{NMe}_2$, $\text{CH}_2\text{CH}_2\text{OMe}$ and $\text{C}(\text{CH}_3)_2\text{CH}_2\text{OMe}$) in toluene have been carried out.⁸⁸ Different morphologies were observed depending on the donor functionalised alcohol used. This is an investigation of methanol as a reactant and the carrier solvent, in combination with GaMe_3 , to form Ga_2O_3 thin films. We have previously shown that the *in situ* AACVD of GaMe_3 and donor functionalised alcohol in toluene yielded transparent films of $\beta\text{-Ga}_2\text{O}_3$ at 450 °C. However, the use of methanol as the solvent has been shown to lead to different microstructures for rutile or anatase titanium dioxide films deposited via AACVD.⁹¹ A change in microstructure or phase could in turn affect the functional properties of the films. Therefore, we were interested in investigating the effect of using methanol in place of a donor functionalised alcohol as the oxygen source. Methanol was used to investigate whether it was possible to deposit Ga_2O_3 using a mono-functionalised alcohol which has not been previously reported in the literature.

This chapter describes the deposition of indium oxide and gallium oxide, and then an assessment on their properties. The gallium precursors investigated are gallium nitrate $[\text{Ga}(\text{NO}_3)_3]$ and trimethylgallium $[\text{Ga}(\text{CH}_3)_3]$, whereas the indium oxide precursor investigated was trimethylindium $[\text{In}(\text{CH}_3)_3]$. In order to analyse the effect of solvent on the characteristics of the film, different additives were investigated. Two types of diols, ethylene glycol $\text{HOCH}_2\text{CH}_2\text{OH}$ and diethylene glycol, $((\text{HOCH}_2\text{CH}_2)_2\text{O}$, digol), and donor functionalised alcohol $\text{HOCH}_2\text{CH}_2\text{NMe}_2$ were studied as oxygen source additives (Fig. 4-3).

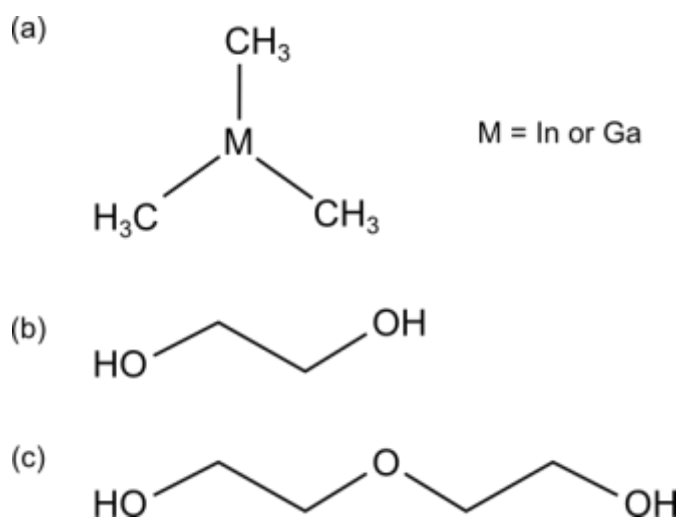


Figure 4-3: Structural diagram of a) $\text{M}(\text{CH}_3)_3$, b) ethylene glycol and c) diethylene glycol.

Due to gallium having natural antimicrobial activity, the effectiveness of the gallium oxide films will be explored. Indium is not an antibacterial agent, therefore the TCO properties will be analysed. The appearances, morphology and reproducibility of the films will be examined in order to choose conditions that produce films that are best for its applications.

4.2 Experimental

4.2.1 Materials and General Methods

The precursor solution for all AACVD depositions was placed in a glass bubbler and vaporised by use of a Vicks ultrasonic humidifier. This produced an aerosol of the precursor in the solvent used. Nitrogen (99.9%) carrier gas was used as supplied from BOC. Depositions were carried out on SiO₂ coated float-glass that was cleaned using propan-2-ol, acetone and dried in air prior to use. The glass substrates were of ca. 90 mm x 45 mm x 4 mm in size. The heating of the glass substrate to the desired temperature was carried out under nitrogen gas and two-way taps were used to divert the nitrogen carrier gas through the bubbler. The aerosol was carried into the reactor in a stream of nitrogen gas through a brass baffle and a top plate was suspended 0.5 cm above the glass substrate to ensure a laminar flow. After all the precursor solution had passed through the chamber the taps were turned to allow only N₂ gas flow through the bypass tap. This was maintained until the reaction chamber temperature fell below 100 °C. The N₂ gas was stopped and the glass substrates were removed. The N₂ gas flow rate was controlled by a calibrated flow meter positioned before the gas enters the bypass bubbler. The total deposition time was in the region of 50 – 80 min.

A graphite block containing a Whatman cartridge heater was used to heat the glass substrate. The temperature of the substrate was monitored by a Pt–Rh thermocouple. Coated substrates were handled and stored in air. Large pieces of glass (ca. 4 cm x 2 cm) were used for X-ray powder diffraction but the coated substrate was cut into ca. 1 cm x 1 cm squares for subsequent analysis by SEM, WDX, transmission/reflectance and UV absorption studies.

InMe₃ and GaMe₃ were used as supplied from SAFC HiTech. InMe₃ and GaMe₃ are pyrophoric and hence manipulations involving these chemicals were performed under a dry, oxygen-free dinitrogen atmosphere using standard Schlenk techniques or in an Mbraun Unilab glovebox. All solvents and alcohols

commercially procured from Aldrich were dried with anhydrous engineering equipment and stored in Young's tap flasks.

4.2.2 AACVD reaction of $Ga(NO_3)_3$ and $HOCH_2CH_2OH$

Dried methanol or toluene (30 ml) was added to gallium nitrate [$Ga(NO_3)_3$, 1.56 mmol] and ethylene glycol [$HOCH_2CH_2OH$, 4.69 mmol]. The resulting solution was mixed under N_2 for 30 minutes in the AACVD bubbler. The resulting solution was mixed for 30 minutes using a sonicator in the AACVD bubbler. The substrate was heated to 450 °C and 550 °C in separate experiments under a flow of N_2 at 1 L/min. After the N_2 was diverted through the bubbler, the aerosol was transported into the reaction chamber. Once deposition was complete the substrate was cooled to below 100 °C under N_2 , before being removed and stored in air. The film deposition time was 1 hour and transparent films covering the entire glass substrate were produced. At each temperature a transparent film with a white powdery appearance was deposited.

4.2.3 AACVD reaction of $Ga(NO_3)_3$ and $(HOCH_2CH_2)_2O$

Dried methanol or toluene (30 ml) was added to gallium nitrate [$Ga(NO_3)_3$, 1.74 mmol] and digol [$(HOCH_2CH_2)_2O$, 10.45 mmol]. The resulting solution was mixed under N_2 for 30 minutes in the AACVD bubbler. The substrate was heated to 400 °C and 450 °C in separate experiments under a flow of N_2 at 1 L/min. At each temperature a transparent film with a white powdery appearance was deposited.

4.2.4 AACVD reaction of $GaMe_3$ with diols

Dried methanol (30 ml) was added to trimethylgallium [$GaMe_3$, 1.74 mmol] and either ethylene glycol [$HOCH_2CH_2OH$, 10.45 mmol] or digol [$(HOCH_2CH_2)_2O$, 10.45 mmol] at -78 °C. The resulting solution was mixed under N_2 for 30 minutes in the AACVD bubbler. The substrate was heated to 450 °C under N_2 at 1 L/min. A transparent film was deposited with uniform coverage and a slight brown tinge.

4.2.5 AACVD reaction of GaMe₃ and methanol

Dried methanol (30 ml) was added to trimethylgallium [GaMe₃, 4.35 mmol] at -78 °C. The resulting solution was mixed under N₂ for 30 minutes in the AACVD bubbler. The Ga₂O₃ films deposited at 450 °C were amorphous. In order for the crystalline phase to be observed, the films were annealed at a high temperature. The same procedure was carried out but a quartz piece placed on top of the glass substrate. The quartz piece was placed in a furnace set at 1000 °C overnight. This produced the crystalline β-Ga₂O₃ on quartz glass.

4.2.6 Preparation of copper gallium oxide thin film

Copper nitrate trihydrate ([Cu(NO₃)₂.3H₂O], 2.06 mmol) was added to dried methanol (30 ml) at room temperature and allowed to dissolve. The copper nitrate solution was then slowly added to GaMe₃ (4.35 mmol) at -78 °C. After 30 minutes of mixing the solution was used for an AACVD experiment. An aerosol was generated at room temperature. A graphite heating block under the glass substrate heated the CVD reactor to 450 °C. Once deposition was complete, the substrate was cooled to room temperature under N₂. The film deposition time was 1 hour and transparent films covering the glass substrate were produced. Crystalline copper gallium oxide films were obtained by depositing onto quartz glass and annealing at 1000 °C overnight in a furnace.

4.2.7 Characterisation of thin films

The resulting thin films were handled and stored in air. The coated glass substrates were used for powder X-ray diffraction (XRD) measured on a Bruker D8 X-ray diffractometer with CuKα₁ and CuKα₁ radiation of wavelength 0.154056 and 0.154439 nm respectively emitted with an intensity ratio of 2:1, a voltage of 40 kV and current of 40 mA. The samples were indexed using the GSAS programme, refined via the Rietveld method (LeBail model), and compared to database

standards. Energy dispersive X-ray analysis (EDX) was obtained on Philips XL30ESEM instrument and Scanning electron microscopy (SEM) on a JEOL 6301 instrument. UV-Vis-NIR spectra were recorded in the range 190 – 1100 nm using a Helios double beam instrument. Reflectance and transmission spectra were recorded between 300 – 2300 nm by a Zeiss miniature spectrometer. Reflectance measurements were standardised relative to a rhodium mirror and transmission relative to air.

X-ray photoelectron spectroscopy (XPS) was performed using a Thermo Scientific K-alpha photoelectron spectrometer using monochromatic Al_{Kα} radiation. Samples were earthed using copper tape. Higher resolution scans were recorded for the principal peaks of Cu(2p), Ga(3d, 2p), O(1s) and C(1s) at a pass energy of 50 eV. The peaks were modelled using CasaXPS software with binding energies adjusted to adventitious carbon (284.5 eV) for charge correction.

Dr Husn-Ubayda Islam performed X-ray absorption spectroscopy (XAS) measurements on the Dutch-Belgian Extended X-ray absorption fine structure (EXAFS) beamline (BM26A) at the ESRF in Grenoble. Monochromatic radiation was supplied by a double Si(111) crystal, and fluorescence was measured using a 9 element germanium solid state detector. XAS of the film was acquired in fluorescence. Measurements of the thin film and pelletized copper standards were taken on the copper K-edge (8987eV). XAS data were processed and X-ray absorption near edge structure (XANES) analysis was performed using Horae Athena software, and detailed EXAFS analysis was performed on Excurve version 9.273.

4.2.8 Microbiology Assay

E. coli strain (ATCC 25922) and *S. aureus* (8325-4) was maintained by weekly subculture on Brain Heart Infusion (BHI) agar (Oxoid, Basingstoke, UK). One bacterial colony of either *E. coli* or *S. aureus* was used to inoculate 10 mL of sterile BHI broth (Oxoid, Basingstoke, UK) and incubated aerobically at 37 °C for 24 hours.

Bacteria from the overnight culture were harvested by centrifugation at 13,000 xg for 1 minute. Bacteria were then re-suspended in phosphate-buffered saline (PBS) (Oxoid, Basingstoke, UK) and again centrifuged for 13,000 xg for 1 minute. Finally the bacterial pellet was re-suspended in PBS before use. The turbidity of the bacterial cell suspension was measured at 600 nm using a spectrophotometer and was adjusted to an optical density which corresponded to approximately 10^5 colony forming units (cfu) per 25 μ L aliquot.

Prior to use, the gallium oxide and copper gallium oxide samples were cut into 1x1 cm sections. A humidity chamber was created to ensure that the suspensions did not dry out. For each exposure time, triplicate samples were analysed and uncoated glass microscope slides were used as a control. Each exposure time was also repeated twice. A 25 μ L aliquot of the bacterial cell suspension was spread evenly on the surface of each slide and incubated at room temperature (21 ± 2 °C) for the allocated exposure time. After incubation the slides were aseptically transferred to 225 μ L PBS and vortexed for 30 seconds to release the bacteria into the solution. Serial dilutions of the resulting bacterial suspensions were prepared in PBS and 25 μ L from each dilution was spread on to MacConkey Agar (Oxoid, Basingstoke, UK) for *E. coli* and BHI agar (Oxoid, Basingstoke, UK) for *S. aureus*. Plates were allowed to dry before inverting and incubating aerobically at 37 °C for 24 hours. After incubation, any bacterial colonies were counted and viable counts of bacteria were calculated. Mann-Whitney U test was used to determine the significance of the activity of gallium oxide and copper gallium oxide compared to the control glass slide. As well as, determining the significance of the activity of gallium oxide compared to the copper gallium oxide.

4.2.9 AACVD of $InMe_3$ and MeOH in toluene

The substrate was heated to 450 °C under a flow of N_2 at 1 L/min. Toluene (20 mL) and MeOH (0.46 mL, 11.2 mmol) was added to $InMe_3$ (0.3 g, 1.88 mmol) at -78 °C. The resulting solution was mixed under N_2 for 30 mins in the AACVD bubbler. After this time the N_2 was diverted through the bubbler transporting the aerosol into the

reaction chamber. Once deposition was complete the substrate was cooled to below 100 °C under N₂, before being removed and stored in air. No film deposition was observed.

4.2.10 AACVD of InMe₃ and MeOH

Dry MeOH (20 mL) was added to InMe₃ (0.20 g, 1 mmol) at -78 °C. The resulting solution was mixed under N₂ for 30 mins in the AACVD bubbler. The substrate was heated to 4 different temperatures; 350, 400, 450 and 500 °C in separate experiments under a flow of N₂ at 1 L/min. At each temperature a uniform transparent film was deposited with the greatest substrate coverage observed at 450 °C.

4.2.11 AACVD of InMe₃ with HOCH₂CH₂NMe₂ in toluene

The substrate was heated to 450 °C under a flow of N₂ at 1 L/min. Toluene (30 mL) and the donor-functional alcohol HOCH₂CH₂NMe₂ (1.12 mL) was added to InMe₃ (0.3 g, 1.88 mmol) at -78 °C. The resulting solution was mixed under N₂ for 30 mins in the AACVD bubbler. After this time the N₂ was diverted through the bubbler transporting the aerosol into the reaction chamber. Once deposition was complete the substrate was cooled to below 100 °C under N₂, before being removed and stored in air. A transparent film with a brown tinge with 35% coverage of the substrate was deposited.

4.2.12 AACVD of InMe₃ with HOCH₂CH₂NMe₂ in MeOH

Dry MeOH (20 mL) and 6 mol equivalents of HOCH₂CH₂NMe₂ (0.78 mL) were added to InMe₃ (0.20 g, 1 mmol) at -78 °C. The resulting solution was mixed under N₂ for 30 mins in the AACVD bubbler. The substrate was heated to 4 different temperatures; 350, 400, 450 and 500 °C in separate experiments under a flow of N₂ at 1 L/min. At each temperature a uniform transparent film was deposited with the greatest substrate coverage (60%) observed at 350 °C.

4.2.13 Characterisation of In₂O₃ films

X-ray diffraction patterns were measured on a Bruker-Axs D8 (GADDS) diffractometer using CuK_{α1} radiation in glancing angle mode. Scanning electron microscopy (SEM) was carried out on a JEOL JSM-6301F field emission SEM at an accelerating voltage of 5 keV. Wavelength dispersive X-ray (WDX) analysis was obtained on a Philips XL30SEM instrument. UV/VIS/Near IR transmittance and reflectance spectra were obtained on a Perkin Elmer Fourier transfer Lambda 950 spectrometer using an air background and recorded between 190 and 1100 nm.

4.3 Results and Discussion

4.3.1 Gallium Oxide

Initially two different gallium precursors with different oxygen sources (diols and alcohols) were investigated to study which conditions deposited adherent gallium oxide thin films reproducibly and with good coverage (Table 4-1, Fig 4-4). Gallium nitrate ($\text{Ga}(\text{NO}_3)_3$) depositions were investigated with a masters student Rushita Mehta. AACVD with the use of gallium nitrate were carried out initially with Rushita, however they were repeated and full characterisation was carried out.

Table 4-1: *Experimental conditions and resultant films deposited.*

	Gallium Precursor	Diol	Solvent	Temp. / °C	Film appearance
A	Gallium Nitrate, [$\text{Ga}(\text{NO}_3)_3$]	Ethylene glycol	Toluene	450	No film deposition
B		Ethylene glycol	MeOH	450	Non-adherent, white powdery film
C		Ethylene glycol	MeOH	550	
D		Digol	Toluene	450	No film deposition
E		Digol	MeOH	450	White powdery film
F	Trimethylgallium, [GaMe_3]	Ethylene glycol	MeOH	450	Transparent film with a slight brown colour
G		Digol	MeOH	450	
H		None	MeOH	450	Transparent film

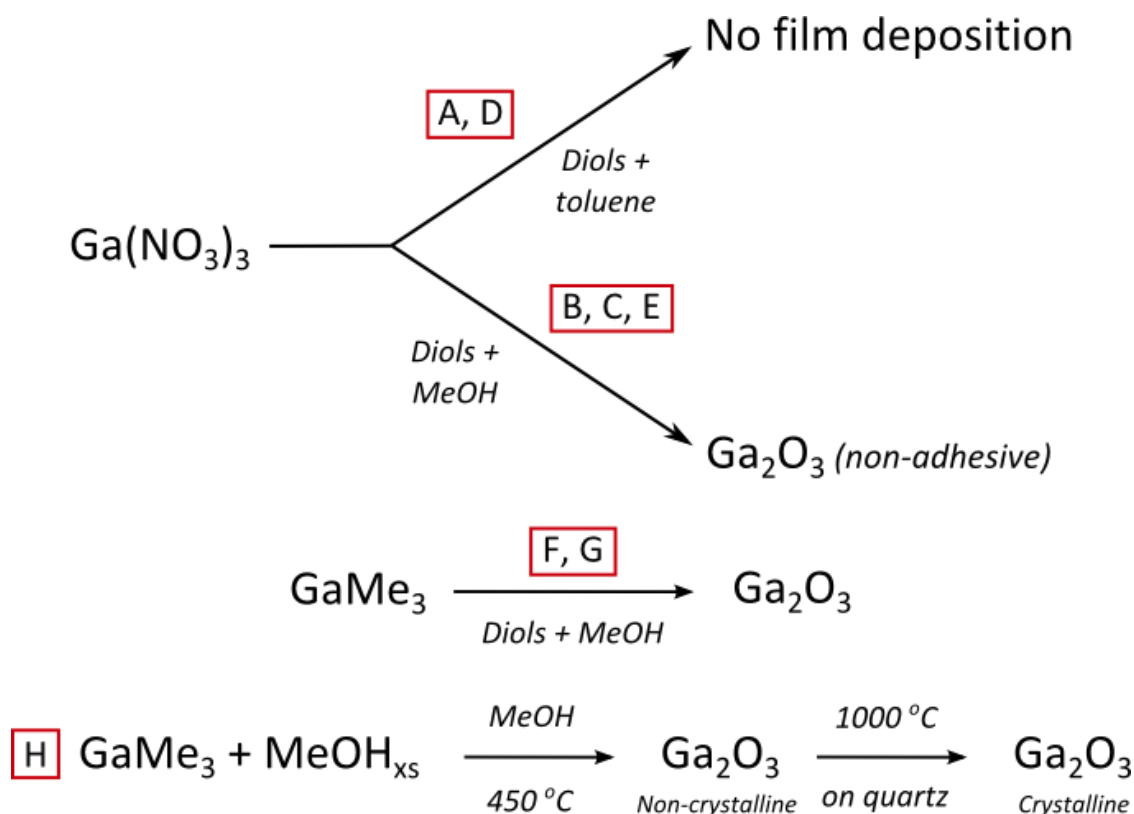


Figure 4-4: Aerosol-assisted CVD reactions to deposit gallium oxide films.

Gallium oxide thin films were generated *in situ* from the AACVD between gallium nitrate precursor and excess diol. An excess of diol was used to ensure the gallium oxide thin film was not oxygen deficient. The gallium precursor that was initially investigated was gallium nitrate ($\text{Ga}(\text{NO}_3)_3$), which was mixed with two different diols; ethylene glycol ($\text{HOCH}_2\text{CH}_2\text{OH}$) and digol ($(\text{HOCH}_2\text{CH}_2)_2\text{O}$).

Initially toluene was chosen as the solvent (Reaction A), however there was some difficulties with the solubility of ethylene glycol and $\text{Ga}(\text{NO}_3)_3$ in toluene. Not enough of the precursor and diol was able to dissolve in the solvent for a film to deposit. Most of the reactants were left at the bottom of the AACVD bubbler after the experiment had completed.

Methanol was then investigated as the solvent and the gallium precursor and diols easily dissolved in this solvent. The substrate was heated to 450 °C and 550 °C with ethylene glycol (Reaction B and C). Both conditions produced non-adherent

transparent thin films with a white powdery appearance. A different diol was then investigated, digol ((HOCH₂CH₂)₂O), in an attempt to improve the solubility and hence quality of film produced. Gallium nitrate was mixed with digol in toluene (Reaction D) however, there were solubility issues whereby no film was deposited and the reactants remained in the AACVD bubbler. MeOH was also investigated (Reaction E) in combination with Ga(NO₃)₂ and digol which produced a non-adherent powdery film.

XRD measurements were performed on the thin films but no XRD pattern were seen. This suggests that the films are non-crystalline, which is expected since Ga₂O₃ films deposited at temperatures below 700 °C are amorphous. To produce crystalline Ga₂O₃, the films need to be deposited on quartz and annealed in a furnace at 1000 °C overnight. This was attempted for the films deposited using both diols, however no film was present on the quartz substrate after annealing. This could be due to the film deposited being too thin to be identified or the annealing process destroyed the film.

With the investigation of the use of the precursor, Ga(NO₃)₃, it was established that deposition of 450 °C resulted in complete coverage of the substrate and therefore AACVD runs were chosen at this particular temperature for further study and analysis. As mentioned earlier, the films formed using Ga(NO₃)₃ as a precursor were not adherent to the glass substrate, and so, a more reactive gallium source precursor was required in order for this to occur. It has been previously reported that the chemical reaction between GaMe₃ and donor-functionalized alcohols produced films that were adherent to the substrate. Thereby the use of GaMe₃ with the diols was expected to produce similar results (Reactions F and G).

Transparent films with a slight brown colour were deposited on glass from the AACVD reaction of GaMe₃ and diol, either ethylene glycol (HOCH₂CH₂OH) or digol [(CH₂CH₂OH)₂O] in dry MeOH at 450 °C. The films deposited were uniform and covered the substrate completely. The films were adherent to the substrate.

EDX measurements were taken to determine the composition of the films. EDX confirmed the presence of gallium and oxygen. However, due to the films being

thin, there was breakthrough to the underlying glass substrate. This leads to an increase of oxygen present in the data obtained since the oxygen detected is from the film itself and from the glass substrate. This was taken into account when calculating the Ga:O ratio. Reaction F produced Ga₂O₃ film with a Ga:O ratio of 1:1.4 whereas, Reaction G was 1:1.8. EDX also indicated 5% carbon contamination which can explain the brown tinge in the appearance of the film. However, there are errors associated with this method of calculation due to not all of the oxygen present in the glass being detected.

It has been shown that methanol as solvent can lead to the formation of films with unusual microstructure such as TiO₂.⁹¹ The formation of Ga₂O₃ films using methanol as the alcohol and/or solvent were investigated. AACVD of GaMe₃ and six equivalents of methanol and toluene as a solvent with a deposition temperature of 450 °C resulted in no film growth. Therefore the use of methanol as both the oxygen source and solvent was investigated.

The AACVD reaction of GaMe₃ and excess methanol was carried out at 450 °C (Reaction H). A transparent film was deposited that covered the entire substrate. The successful formation of Ga₂O₃ thin film via the *in situ* AACVD reaction of GaMe₃ and methanol indicates that there is no need to prepare, isolate and purify a single-source precursor.

The temperature of deposition was too low for crystalline Ga₂O₃ to form since temperatures above 700 °C are necessary. For crystalline Ga₂O₃ to form, the film was deposited onto quartz substrate instead of glass and annealed overnight in a furnace set at 1000 °C. The film changed from being transparent to a white, less adhesive film. The crystallinity of the annealed Ga₂O₃ films was investigated using powder XRD data on the annealed Ga₂O₃. Peaks seen in Figure 4-5 match to the positions expected for β-Ga₂O₃.

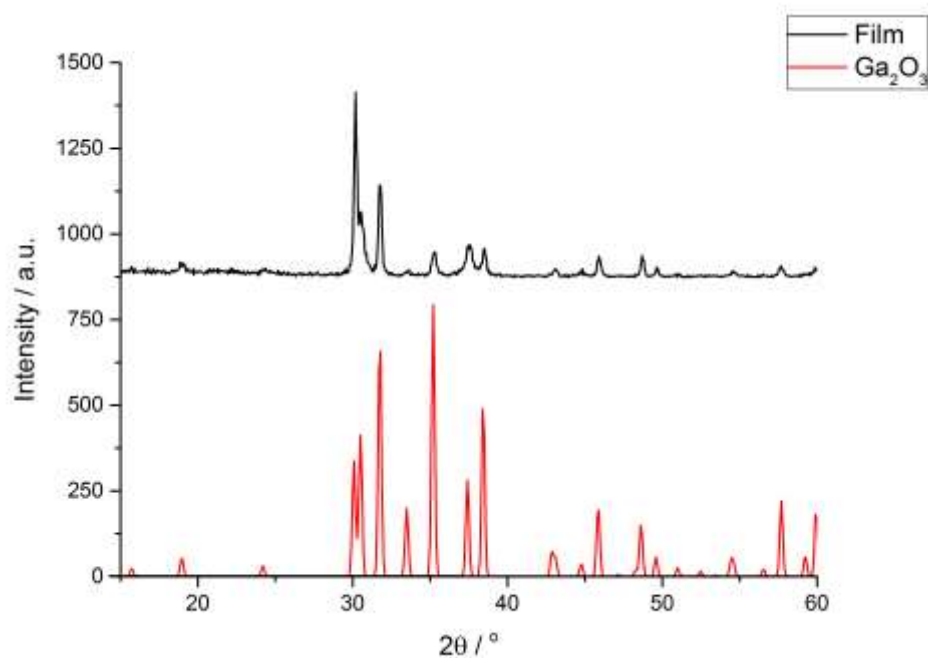


Figure 4-5: XRD pattern of crystalline Ga_2O_3 film (black) deposited using GaMe_3 and MeOH at $450\text{ }^\circ\text{C}$ and annealed with standard reference Ga_2O_3 XRD pattern (red).

The films deposited using $\text{Ga}(\text{NO}_3)_3$ produced non-adherent films that could be easily removed with touch and suspending in organic solvents (methanol, acetone). However, the films deposited using GaMe_3 were adherent to the substrate and were not changed after suspending in organic solvents (methanol, acetone) although they were damaged and completely removed under acidic conditions (conc. HNO_3).

4.3.2 Optical Properties

The transmission and reflectance measurements were taken for the Ga_2O_3 thin films. All the as-deposited films displayed minimal reflectivity (5 – 15%). However depending on the gallium precursor, the transmission varied. Ga_2O_3 deposited from $\text{Ga}(\text{NO}_3)_3$ with ethylene glycol, or digol in MeOH had transmission between 65 – 77% whereas the films deposited using GaMe_3 were more transparent with transmissions between 77 – 89%.

The UV/Visible measurements were taken between 300 – 1100 nm. All films displayed a slight shift in the absorption edge towards the visible relative to plain glass substrate. A Tauc plot was constructed to calculate the band gap of the Ga₂O₃ films. This is constructed by plotting photon energy ($h\nu$) against the square of the materials absorption coefficient multiplied by the photon energy, $(\{\alpha h\nu\}^2)$.¹⁰² Films deposited using Ga(NO₃)₃ had a band gap between 4 – 4.2 eV, which is lower than the literature value of 4.5 – 4.9 eV. This could be due to impurities present in the film that skew the band gap calculated. The band gap calculated for the Ga₂O₃ deposited using GaMe₃ was between 4 – 4.8 eV, which is comparable to the literature value.⁸⁸

4.3.3 Morphology of Ga₂O₃ films

SEM of the Ga₂O₃ thin films deposited using Ga(NO₃)₃ and GaMe₃ are shown in Fig. 4-6. It can be seen that the gallium precursor, diol and annealing films have an effect on the morphology of the film.

Ga₂O₃ films deposited using Ga(NO₃)₃ and diols produced films with uniform spherical particles with sizes ranging from 0.4 – 1.2 μm, which can be related to the formation of powdery-like depositions seen. Whereas, the films deposited using GaMe₃ and diols produced different microstructure corresponding to the more adherent transparent deposition. For these films, larger agglomerated particles ranging between 0.5 – 1.8 μm have formed.

The morphology of Ga₂O₃ deposited using GaMe₃ and MeOH produced a morphology consisting of smaller particles (~100 nm) agglomerated together. When the film was annealed producing crystalline Ga₂O₃, the microstructure changed and consisted of larger particles (~0.8 μm) conforming to island growth model.

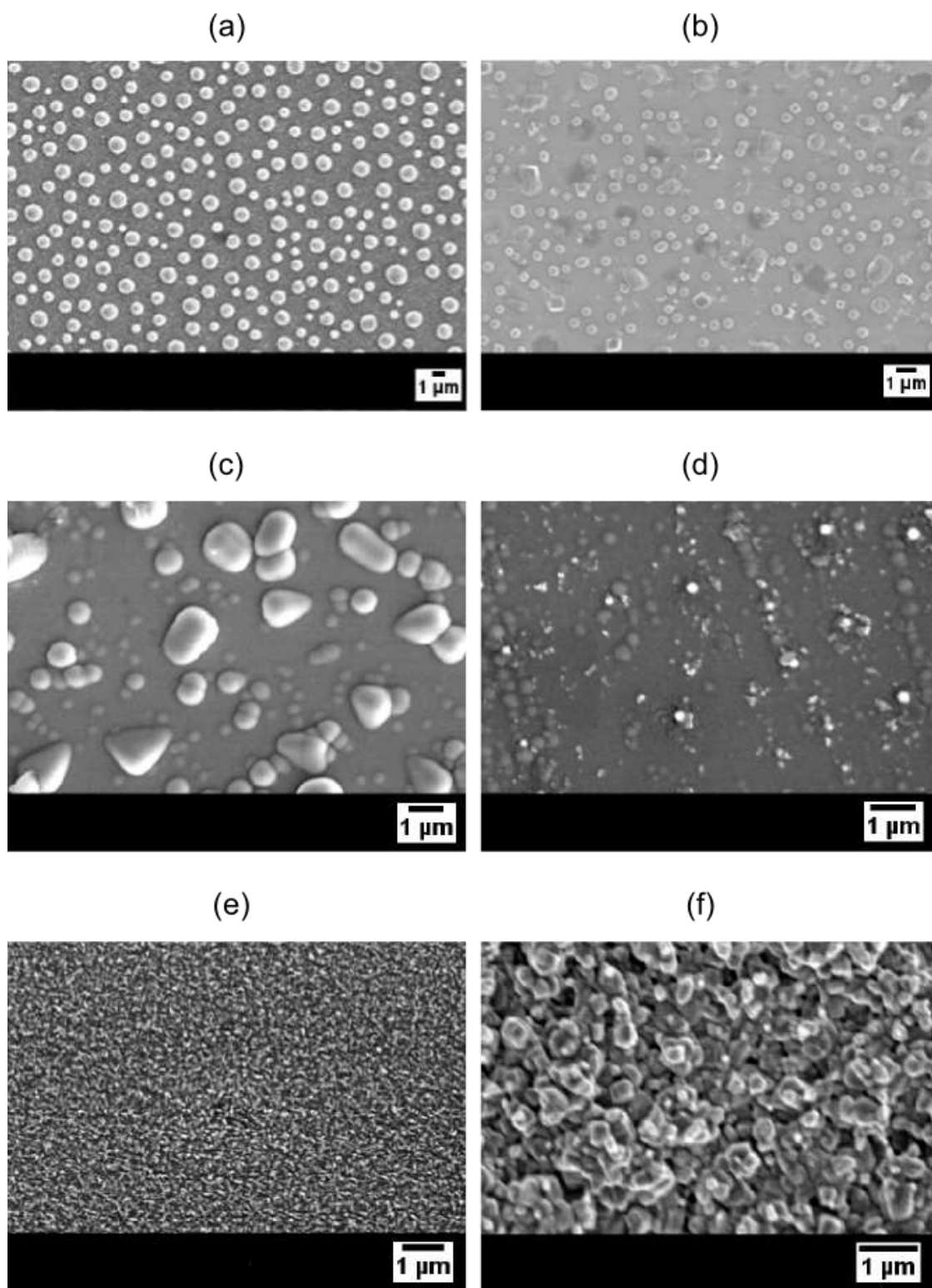


Figure 4-6: SEM images of Ga_2O_3 deposited using reactions:

a) Reaction B [$Ga(NO_3)_3/MeOH/HOCH_2CH_2OH$], b) Reaction E [$Ga(NO_3)_3/MeOH/(CH_2CH_2OH)_2O$], c) Reaction F [$GaMe_3/MeOH/HOCH_2CH_2OH$], d) Reaction G [$GaMe_3/MeOH/(CH_2CH_2OH)_2O$], e) Reaction H [$GaMe_3/MeOH$] and f) Annealed film of Reaction H at 450 °C.

4.3.4 Gallium Oxide film

The gallium precursor that produced the most reproducible and adherent films was GaMe₃. In comparison to the use of diol, when methanol was used as the oxygen source, the films produced were more transparent and adhesive. This is an advantage for antimicrobial coatings because there will be a wide variety of surfaces that these coating can be potentially deposited on. Therefore, AACVD depositions using GaMe₃ and methanol were repeated and deposited on to microscope slides instead of float glass and further analysis was carried out. The film thickness of the amorphous Ga₂O₃ thin films deposited on microscope slides were taken using side-on SEM. Fig. 4-7 shows that the thickness of the film is uneven, therefore an average of the film thickness was calculated, which was approximately 250 nm.

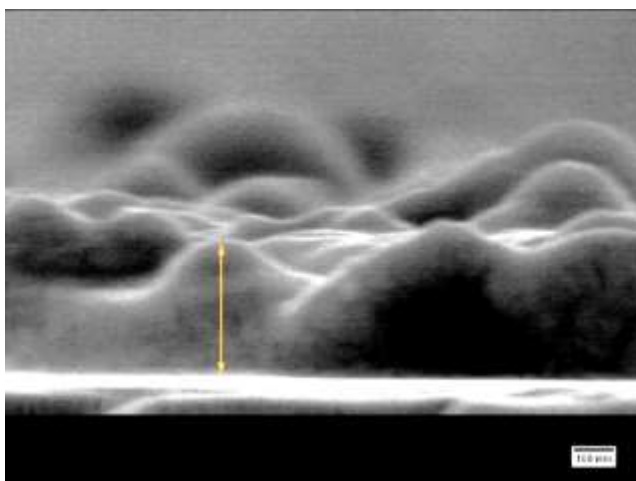


Figure 4-7: Side-on SEM of amorphous Ga₂O₃ thin films.

4.3.5 XPS analysis of Ga₂O₃ films

XPS was performed on these amorphous thin films (Fig. 4-8) to confirm the presence of Ga₂O₃ without annealing the film. The binding energies of Ga 3d_{5/2} and 3d_{3/2} were seen at 20.5 eV and 20.1 eV respectively, which corresponds to Ga³⁺ found in Ga₂O₃.⁸⁸ The binding energies of Ga 2p_{3/2} and 2p_{1/2} were seen at 1117.9 and 1144.9 eV respectively. This region was observed due to the low doublet

splitting in the Ga 3d. These binding energy values also correspond to Ga³⁺ in Ga₂O₃ confirming the presence of Ga₂O₃ on the surface of the amorphous thin films deposited on a microscope slide.

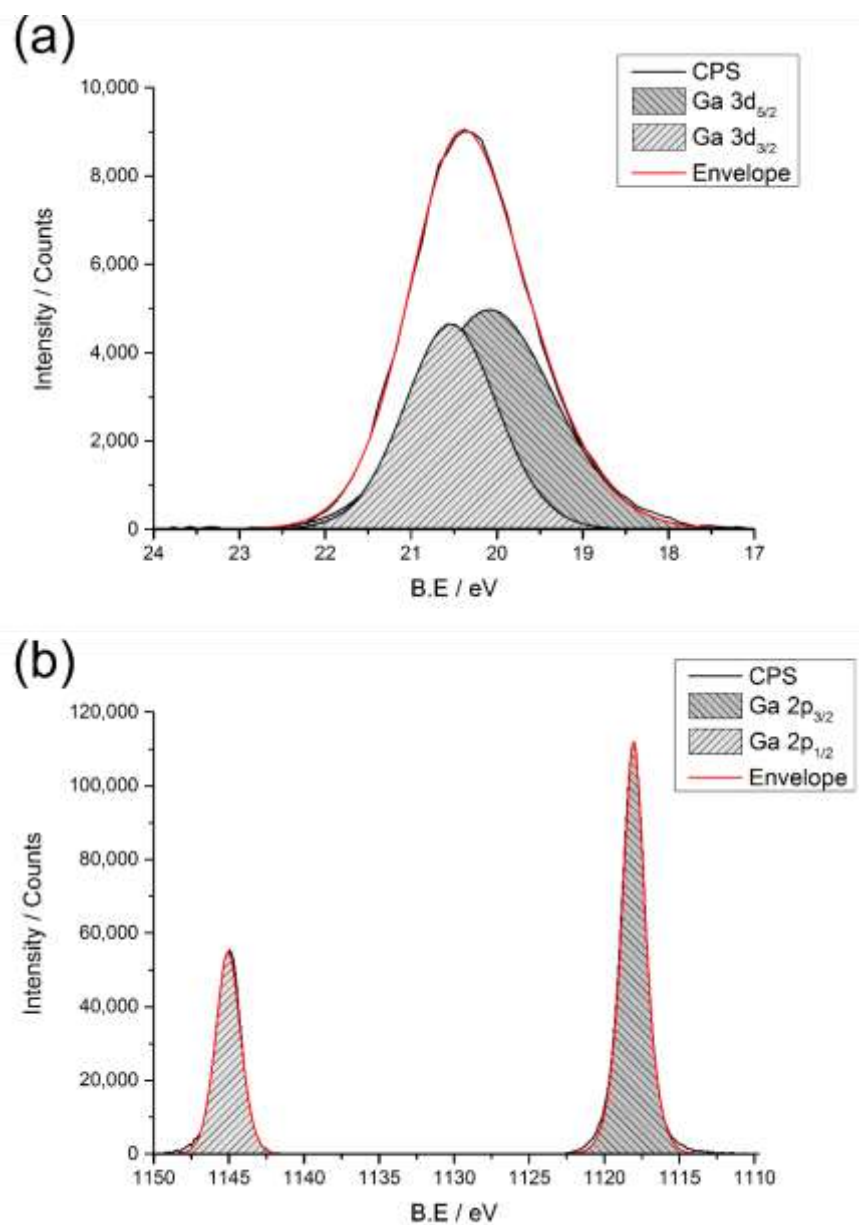


Figure 4-8: XPS spectra of a) Ga 3d and b) Ga 2p peaks from the surface of the amorphous Ga₂O₃ films.

4.4 Copper Gallium Oxide Thin Films

The high antimicrobial activity of copper has been previously discussed in chapter 3. Therefore, in order to enhance the efficacy of the Ga₂O₃ films, an investigation into incorporating copper into the films were carried out. The antibacterial mechanism of copper is different to gallium, which could allow for more effective films.

AACVD of GaMe₃ and copper nitrate [Cu(NO₃)₂.3H₂O], in a ratio of 2:1 respectively in dried methanol at -78 °C was carried out. The suspension was allowed to mix for 30 minutes forming a dark yellow solution. AACVD of the solution was carried out at 450 °C and once the deposition was complete, the film was allowed to cool to room temperature under nitrogen. A colourless transparent film was produced.

The films deposited were adherent to the glass substrate and were not changed after suspension in organic solvents (methanol, acetone) although they were damaged and completely removed under acidic conditions (conc. HNO₃).

XRD measurements were performed on these films but no XRD pattern was observed. This would indicate that the films were deposited at a temperature too low to form crystalline thin films. However, it also confirms that no crystalline copper or copper oxide was formed.

The films deposited on quartz was clear and transparent but once annealed at 1000 °C, the films appeared white. The film become less adherent to the quartz surface and were easily removed using organic solvent. XRD measurements were taken from these crystalline film, which produced an XRD pattern, as shown in Fig. 4-9. The XRD pattern does not fit with β-Ga₂O₃ previously seen, however some peaks observed correspond to Ga₂O₃ as well as copper(II) oxide (CuO). Since the films transparency decreased and the films were less adhesive to the surface, the amorphous material appears more appropriate for microbiological analysis and will be further analysed.

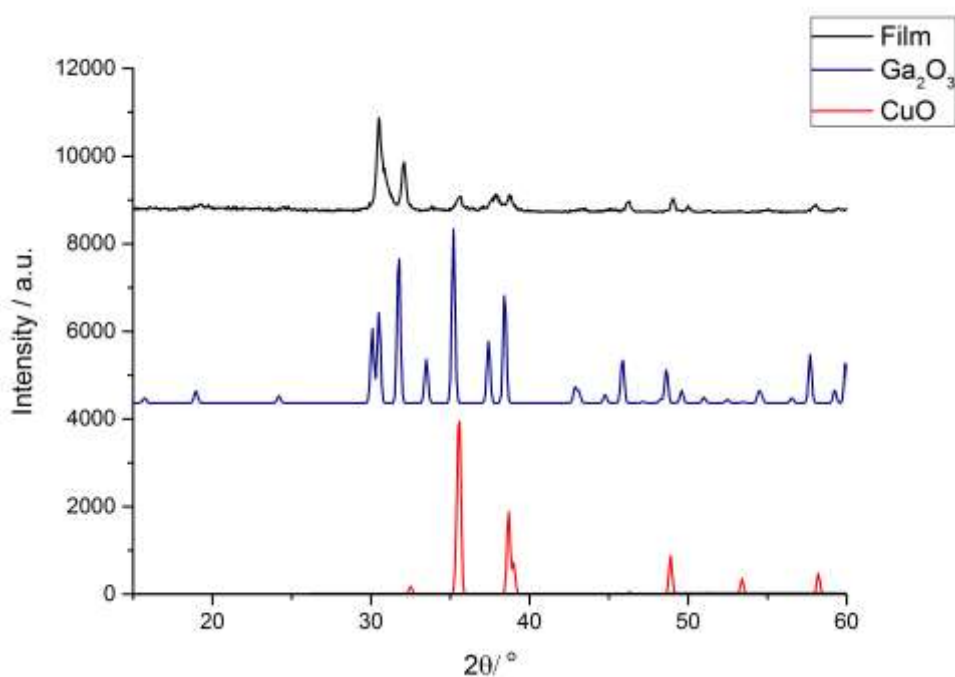


Figure 4-9: XRD pattern of crystalline copper gallium oxide film with standard patterns of Ga_2O_3 and CuO .

4.4.1 EDX Measurements

EDX analysis was utilised to obtain the composition of the film and carried out to determine the stoichiometry of the amorphous material. The EDX measurements (Table 4-2) have shown there is on average 4.4 at% Cu incorporated into the film. The gallium to copper ratio was 4.7:1 indicating that not all the copper in the precursor starting solution was transferred to the deposited film.

Table 4-2: EDX measurements taken from the amorphous copper gallium oxide film.

	<i>Atomic %</i>						<i>Average</i>
<i>Gallium</i>	23.4	23.6	12.5	14.1	24.4	26.5	20.7
<i>Copper</i>	3.0	3.2	5.2	5.3	5.1	4.6	4.4

4.4.2 XPS analysis of copper gallium oxide films

XPS was performed on the amorphous material in order to identify what was present and gallium and copper were identified on the surface. The binding energies of Ga $3d_{5/2}$ and $3d_{3/2}$ were seen at 20.5 and 20.1 eV respectively that corresponds to Ga^{3+} found in Ga_2O_3 (Fig 4-10).⁸⁸ The oxidation state of copper was investigated for the amorphous material and the binding energies observed for Cu $2p_{3/2}$ was 932.6 eV corresponds to Cu^{2+} and Cu^{1+} . Satellite peaks usually found between 940 – 946 eV for Cu^{2+} were not observed suggesting that Cu^{2+} is not present at the surface and the peaks correlate to Cu^{1+} .^{195,196} The binding energy of Cu $2p_{1/2}$ is 952.37 eV also corresponds to Cu^{1+} . XPS has identified both Ga_2O_3 and Cu_2O present on the surface of this amorphous material suggesting that a composite may have been deposited. Quantification using peak areas determined by the Shirley method and empirical sensitivity factors gave a gallium to copper ratio of 6.6:1. This differs from the ratio obtained from the EDX measurements which was 4.7:1. This suggests that there may be more copper in the bulk than on the surface.

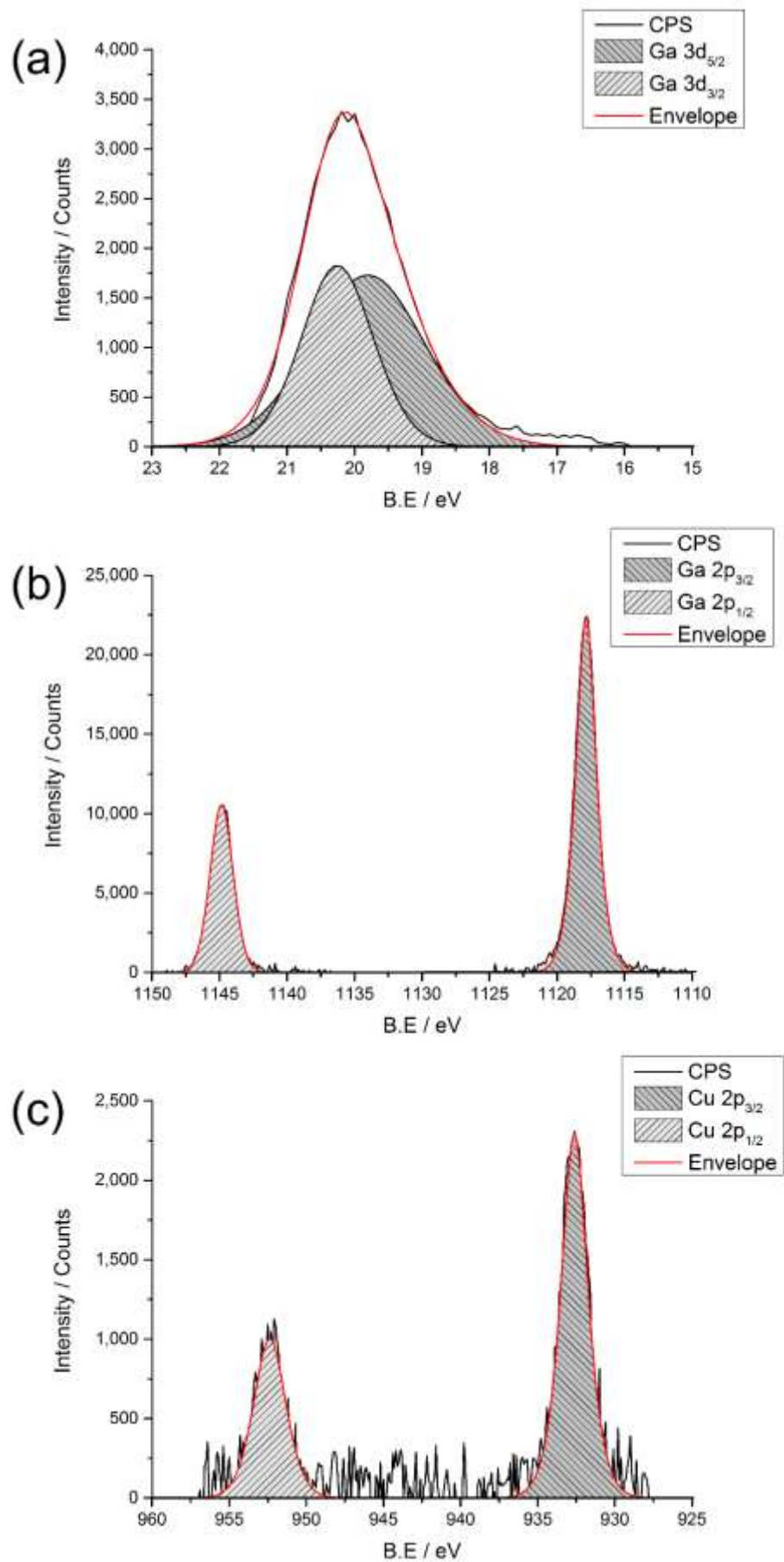


Figure 4-10: XPS spectra of a) Ga 3d, b) Ga 2p and c) Cu 2p peaks from the surface of the amorphous copper gallium oxide films.

4.4.3 Optical Properties

The optical properties of the amorphous copper gallium oxide films were studied by transmission and reflectance measurement between 300 and 2300 nm and by UV-Vis spectroscopy between 90 – 1100 nm. The amorphous films showed a slight shift in the adsorption edge towards the visible relative to a glass substrate. The films displayed minimal reflectivity (5 – 10%) and high transmission (74 – 84%). This is very similar to the results seen for the Ga₂O₃ film deposited but the pure Ga₂O₃ films had higher transmission.

The optical properties were investigated using UV/Visible spectra measurement between 300 – 1100 nm. This data can be used to find the band gap of a material by converting the data in to a Tauc plot.¹⁰² This is constructed by plotting photon energy ($h\nu$) against the square of the materials absorption coefficient multiplied by the photon energy ($\{\alpha h\nu\}^2$). The amorphous material had a band gap calculated at 2.05 eV, which corresponds to Cu₂O (2.1 eV).¹⁹⁷ This correlates with the results obtained from XPS indicating the presence of Cu₂O in the film suggesting that the amorphous material is a composite of Ga₂O₃-Cu₂O.

4.4.4 X-ray absorption spectroscopy

XAS was used to elucidate the local structure of the copper species within the amorphous thin film. XAS is a powerful atom specific, average technique which can be used to determine oxidation state, geometry, bond distances and coordination numbers.

Linear combination analysis (LCA) and X-ray absorption near edge structure (XANES) were performed on the Ga₂O₃-Cu₂O thin films. Cu k-edge XANES data for the sample is shown in Fig. 4-11 along with the corresponding data for metal powders: Cu, Cu₂O and CuO. The energy scales of all the spectra have been consistently normalised. Fig. 4-11 shows the local environment of the Cu can have an effect on the shape of the XANES spectra making it easier to identify the local environment of the Cu present in the Ga₂O₃-Cu₂O films. In this case, the XANES

spectra for the amorphous Ga₂O₃-Cu₂O films match that of Cu, Cu₂O and CuO standards indicating that copper is present in the film in all three oxidation states.

LCA for the Ga₂O₃-Cu₂O (Table 4-3) calculated the Cu/Cu₂O/CuO ratio present in the film is 0.37/0.60/0.03. The XPS data and band gap calculations previously discussed the presence of Cu₂O however, the XANES data indicates that Cu, Cu₂O and a very small amount CuO were identified. XPS only identified the presence of Cu₂O on the surface of the material. This could be due to Cu and CuO not being present at the surface but can be detected in the bulk of the film. The LCA also shows that Cu₂O has the largest amount in the ratio, which corresponds to the identification that the composite is Ga₂O₃-Cu₂O material.

EXAFS were analysed and revealed the presence of two distances (Table 4-3). The local structure of Cu₂O with 2 Cu-O distances that were found to be 1.87 Å, which corresponds to bond distances found in Cu₂O (1.85 Å). The Cu-Cu distances were identified as 2.55 Å, which is comparable to Cu-Cu bond distance found in pure copper films (2.54 Å).

Table 4-3: Linear combination analysis (LCA) of XANES fit for amorphous Ga₂O₃-Cu₂O film

LCA of XANES of Ga ₂ O ₃ -Cu ₂ O					
Standard	Ratio		R-factor		
Cu ₂ O	0.60 (0.03)		2.51 x 10 ⁻⁴		
CuO	0.03 (0.02)				
Cu	0.37 (0.02)				
EXAFS fit of Ga ₂ O ₃ -Cu ₂ O					
Scatter	N	R _{XRD} (Å)	R _{EXAFS} (Å)	σ ² (Å ²)	F
O	2.0	1.85 (Cu ₂ O)	1.87 (0.03)	0.010	12
		1.95 (CuO)			
Cu	4.6	2.54 (Cu)	2.55 (0.02)	0.010	

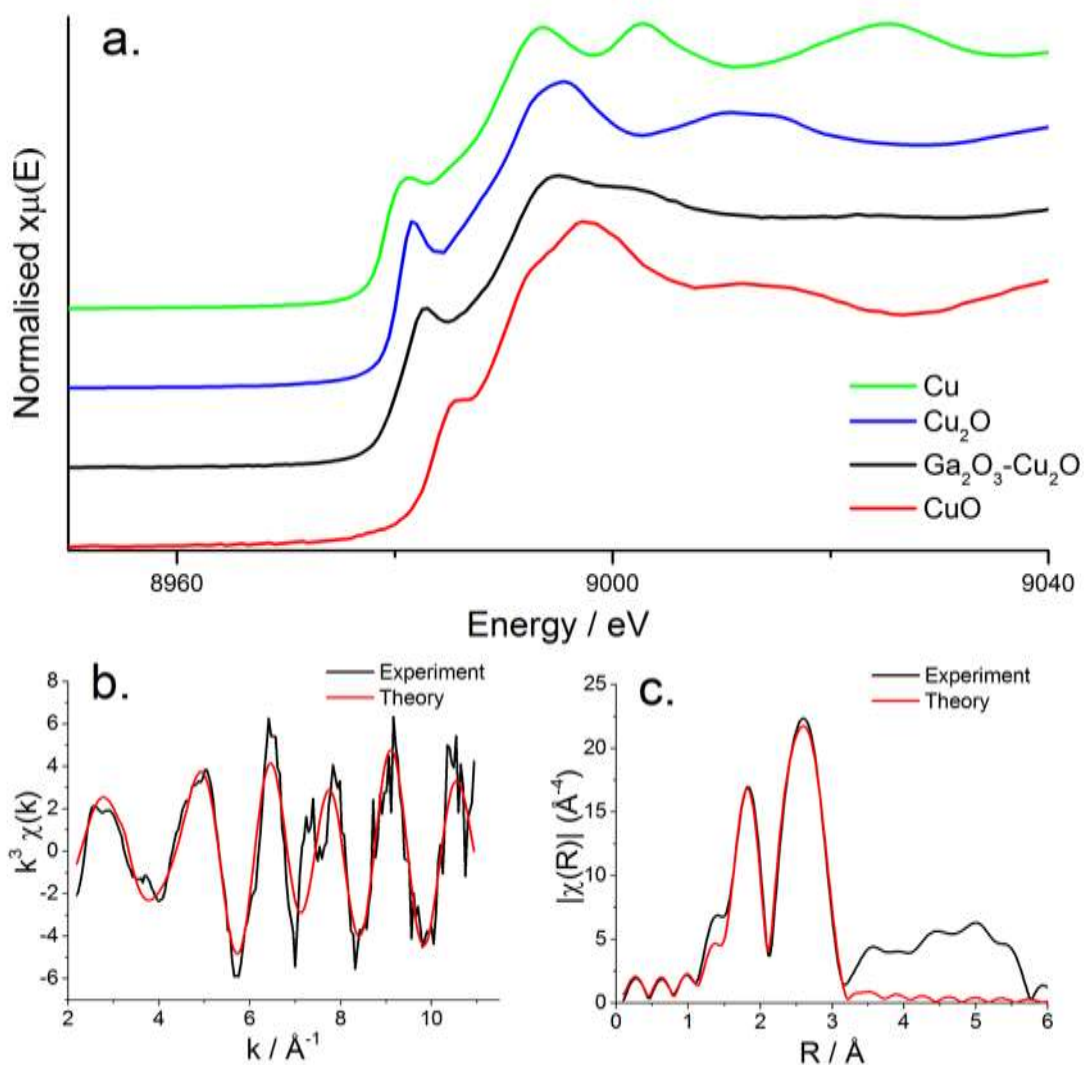


Figure 4-11: Normalised copper K-edge XANES spectra for Cu metal foil, Cu, Cu_2O and $\text{Ga}_2\text{O}_3\text{-Cu}_2\text{O}$ thin film sample. b) k^3 -weighted $\chi(k)$ spectra $\text{Ga}_2\text{O}_3\text{-Cu}_2\text{O}$ and theoretical fit. c) Fourier transform of EXAFS of the $\chi(k)$.

4.4.5 Morphology of $Ga_2O_3-Cu_2O$ films

SEM was used to examine the surface morphology of the deposited films. The microstructure of the amorphous $Ga_2O_3-Cu_2O$ films was shown to have particles approximately 100 – 200 nm (Figure 4-12). The particles appear to cluster together. This microstructure observed is different from the Ga_2O_3 films previously discussed (Fig. 4-12). The morphology of pure Ga_2O_3 films appear to consist of larger particles that were uniform and similar in shape.

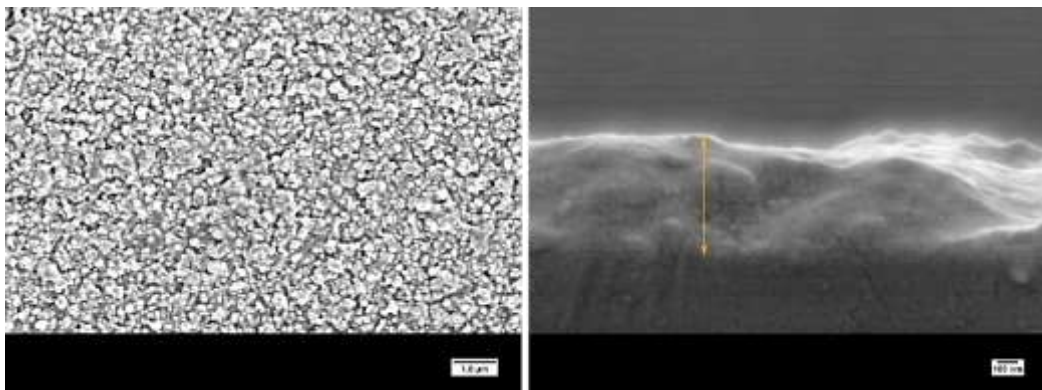


Figure 4-12: SEM and side-on SEM images of amorphous $Ga_2O_3-Cu_2O$ thin film.

4.5 Antimicrobial activity of Ga₂O₃ and Ga₂O₃-Cu₂O

Copper gallium oxide thin film would be advantageous due to the films possessing the ability to have multi-route antimicrobial activities while maintaining transparency. This will enable the thin films to have a wide variety of applications since AACVD has the ability to deposit on a diverse range of substrates including stainless steel that is primarily used for touch surfaces in hospitals.

The antimicrobial properties of amorphous Ga₂O₃ and Ga₂O₃-Cu₂O films deposited from GaMe₃ in methanol or a mixture of GaMe₃ and [Cu(NO₃)₂·3H₂O] via AACVD at 450 °C were tested against *E. coli* and *S. aureus*. Samples were cut in 1x1 cm sample sections and were covered with 25 µL of bacterial cell suspension containing approximately 10⁵ cfu. Through enumeration and plating of the bacterial suspensions and subsequent overnight incubation (37 °C), the resultant viable counts of bacteria for each sample section was determined. The results for the gallium oxide and copper doped gallium oxide films, shown in Figure 4-13, demonstrate that the films have antimicrobial activity against *E. coli* and *S. aureus*. Glass microscope slides cut into 1x1 cm² were used as controls. Each point represents the log₁₀ of the mean number of viable bacteria from three samples and error bars represent the standard error. The results for the films demonstrate that doping the Ga₂O₃ has an effect on the antimicrobial activity. For *E. coli*, a 0.9-log₁₀ reduction (P < 0.01) in viable bacteria was observed after 24 hours as shown in Figure 4-13a. In the case of Ga₂O₃-Cu₂O, the same reduction in viable colony counts was achieved after 9 hours (P < 0.001) and 4-log₁₀ reduction was observed after 24 hours. This was similar for *S. aureus*, 1.2-log₁₀ reduction (P < 0.001) for Ga₂O₃ was observed after 24 hours however, for the Ga₂O₃-Cu₂O samples a 0.8-log₁₀ reduction was observed after 9 hours (P < 0.001) and 4-log₁₀ reduction after 24 hours (P < 0.001). When the Ga₂O₃ thin films are compared to Ga₂O₃-doped phosphate-based glasses similar reduction are seen against *Pseudomonas aeruginosa* (0.86-log₁₀ reduction).^{193,194}

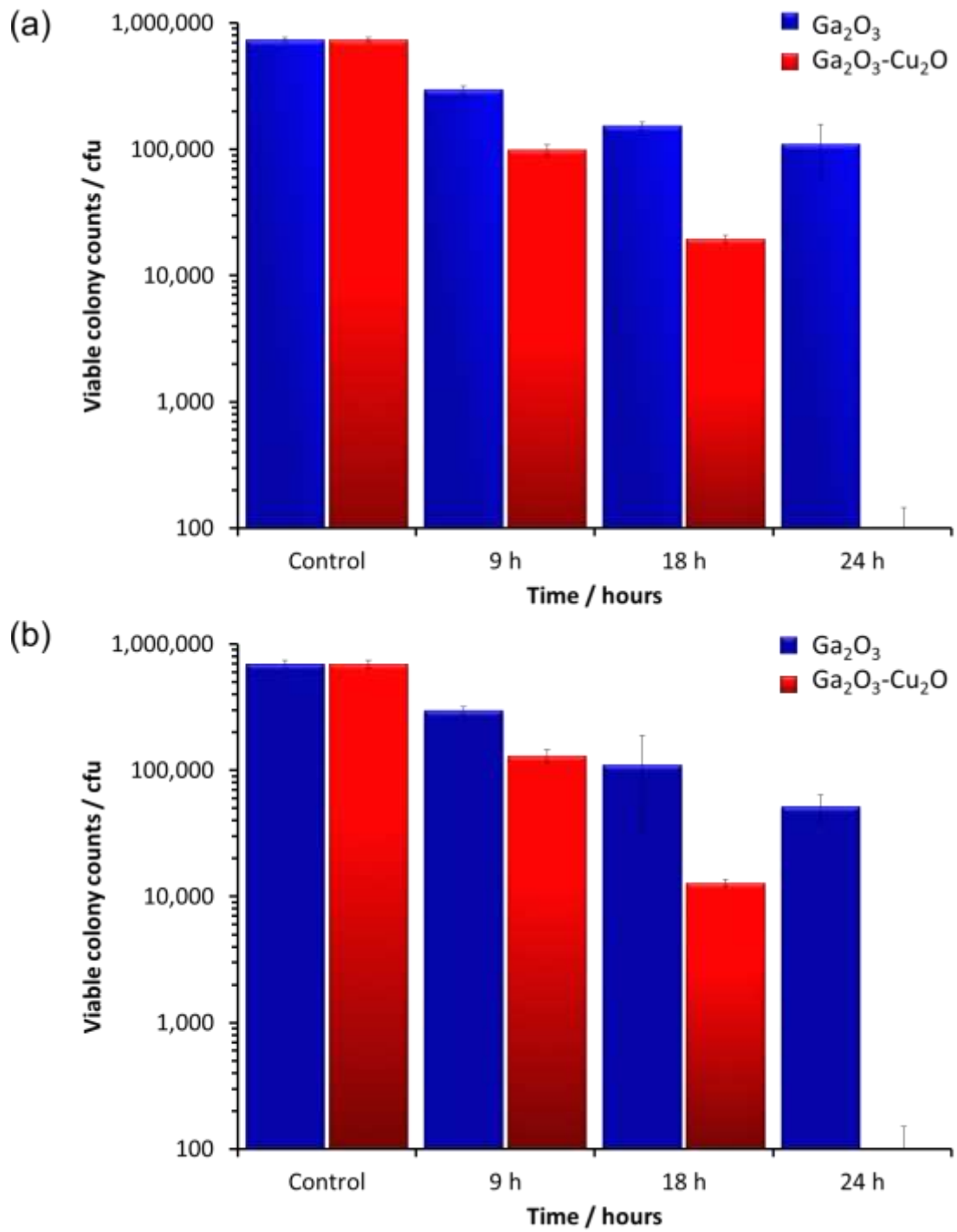


Figure 4-13: Viable counts of bacteria after incubation on Ga_2O_3 and $\text{Ga}_2\text{O}_3\text{-Cu}_2\text{O}$ thin films tested against a) *E. coli* and b) *S. aureus*.

Overall Ga₂O₃ has been demonstrated to have some antimicrobial activity. With the copper gallium oxide, a much greater bacterial reduction was observed. When comparing the difference between the cfu count between Ga₂O₃ and Ga₂O₃-Cu₂O, it was seen to be highly statistically significant ($P < 0.001$) demonstrating the impact of copper on the sample. The Ga₂O₃-Cu₂O has a much improved antimicrobial efficacy over Ga₂O₃ due to the addition of an antimicrobial metal, copper in a mixture of Cu₂O. Copper has been shown to produce highly significant reduction to HAI bacteria. However, the results shows that bacterial reductions from Ga₂O₃-Cu₂O are significantly lower when compared to pure Cu and Cu₂O (chapter 3). It has been shown that copper can get the observed microbial reduction in 30 minutes instead of 24 hours. However, the Ga₂O₃-Cu₂O films were transparent and have the potential to be deposited on a wide variety of surfaces.

4.6 Indium Oxide Thin Films

In section 4.3 the deposition of gallium oxide thin films using diols as the oxygen source and MeOH as a solvent was described. It was seen that the use of different alcohols can have an effect on the morphology of the films. A similar effect has been seen previously for the deposition of indium oxide thin films. For example, the AACVD of InMe_3 and $\text{HOCH}_2\text{CH}_2\text{NMe}_2$ deposited films with a microstructure consisting of spherical particles. However, films deposited using InMe_3 and $\text{HOCH}_2\text{CH}_2\text{OMe}_2$ produced films with a needle-like morphology. It was also shown in the Ga_2O_3 thin films deposited (Fig. 4-6), that different conditions (solvent, precursor) lead to different microstructures. The effect of solvent on AACVD depositions has also been reported for TiO_2 investigations using methanol which showed that it can lead to the formation of rutile TiO_2 instead of anatase that was formed with all other solvents.

A different morphology of a thin film can have an effect on the functional properties of the film. For example, the microstructure of films is important to TCO applications. In photovoltaic technologies such as silicon thin films,¹⁶² TCO layers with a rough microstructure are commonly used to gain energy such that it is not absorbed in visible light and lost. Therefore, the effect of different alcohols as the oxygen source and/or solvent for the deposition of indium oxide has been investigated. The In_2O_3 depositions were investigated alongside master student Arnold Ratnasothy.

The formation of Ga_2O_3 films from diols was described in section 4.3. In order to study the effect of changing the solvent to methanol in this section (Fig. 4-14), the AACVD of In_2O_3 using a donor-functionalised alcohol ($\text{HOCH}_2\text{CH}_2\text{NMe}_2$) or a diol ($\text{HOCH}_2\text{CH}_2\text{OH}$) with MeOH as the solvent is described (Reaction A and B). Initially the AACVD of InMe_3 and six equivalents of MeOH in toluene (Reaction D) was studied. Similarly to Ga_2O_3 , no film growth was observed and therefore AACVD of InMe_3 and excess (Reaction C) MeOH was attempted with MeOH acting as the oxygen source and solvent. Transparent thin films of In_2O_3 were deposited and MeOH was used as a solvent in all subsequent depositions.

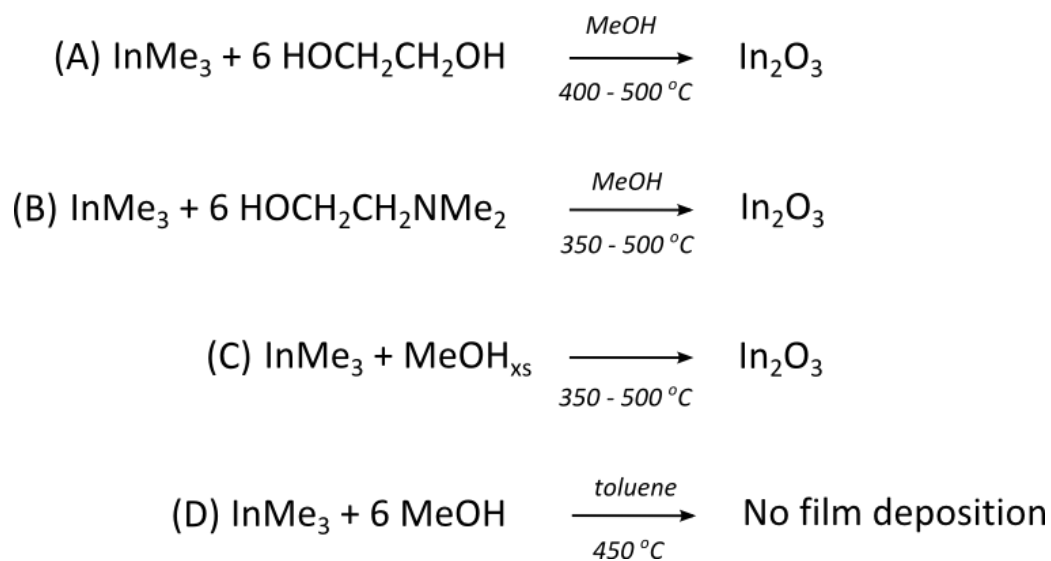


Figure 4-14: AACVD reaction to deposited indium oxide films.

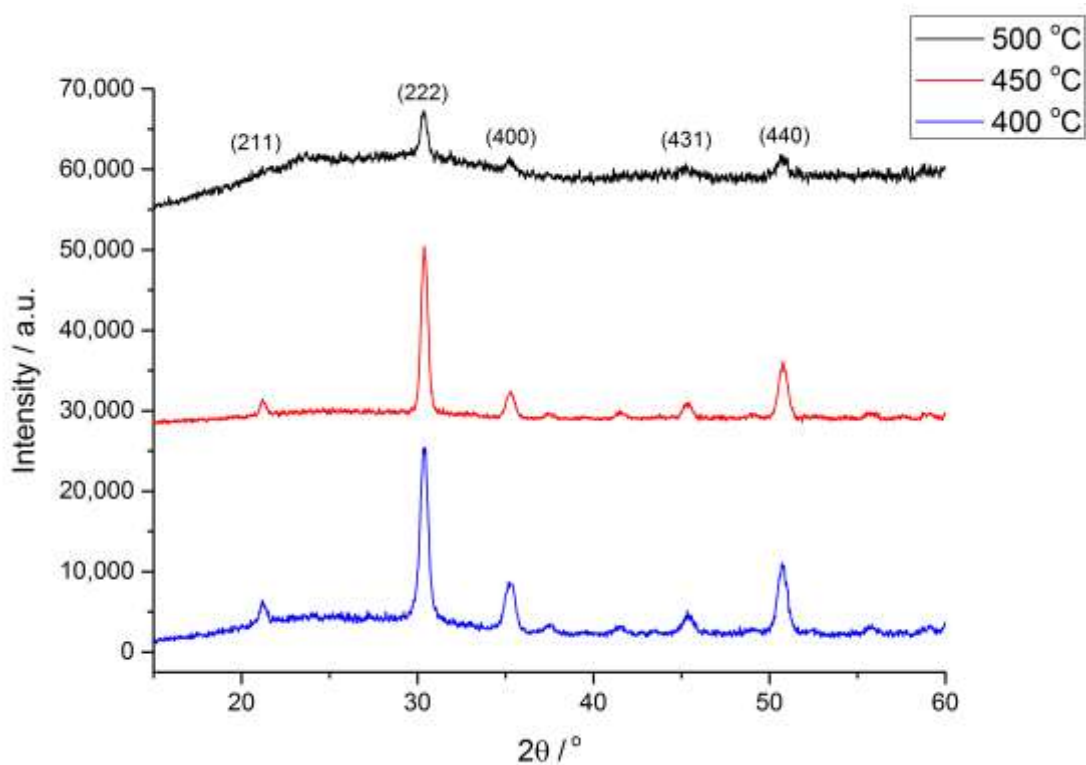


Figure 4-15: XRD patterns obtained for In_2O_3 films deposited by AACVD from the *in situ* reaction of $\text{InMe}_3/\text{HOCH}_2\text{CH}_2\text{OH}$ in MeOH at temperatures between 400 – 500 °C.

In order to investigate the dependence of the physical and chemical attributes of the film on temperature, depositions were also carried out at reduced and higher substrate temperatures between 350 °C and 500 °C.

Following from the Ga₂O₃ films (section 4.3), trimethylindium (InMe₃) was chosen as the indium precursor and methanol as the solvent. Ethylene glycol (HOCH₂CH₂OH) produced the better Ga₂O₃ films with better coverage. Therefore, this diol was used in this investigation. Transparent films were deposited uniformly onto glass substrate from the deposition of AACVD of InMe₃ in methanol (Fig. 4-15). The depositions were carried out between 400 – 500 °C. The best coverage of the glass substrate was achieved at 450 °C in agreement with the Ga₂O₃ films discussed previously. The films were adherent to the substrate and were not changed after suspending in organic solvents (methanol, acetone) although they were damaged and completely removed under acidic conditions (conc. HNO₃).

The In₂O₃ were analysed using a wide range of techniques. EDX analysis detected the presence of both indium and oxygen for all the films. However, once again there is a breakthrough to the underlying glass substrate. Therefore, it was not possible to produce accurate composition of the thin films using this technique.

4.6.1 Powder X-ray Diffraction

All the In₂O₃ films deposited were cubic crystalline In₂O₃ therefore powder X-ray diffraction (XRD) patterns (Fig. 4-15 – 4-17) can be taken, unlike the Ga₂O₃ films. All the films showed a strong reflection in the (222) plane, which has been seen previously for thin films of In₂O₃. XRD patterns exhibit three broad Bragg peaks at 31.2°, 36.5°, and 52.4° 2θ, as well as features at 21.9° 2θ that are broad due to scattering from the amorphous glass substrate.

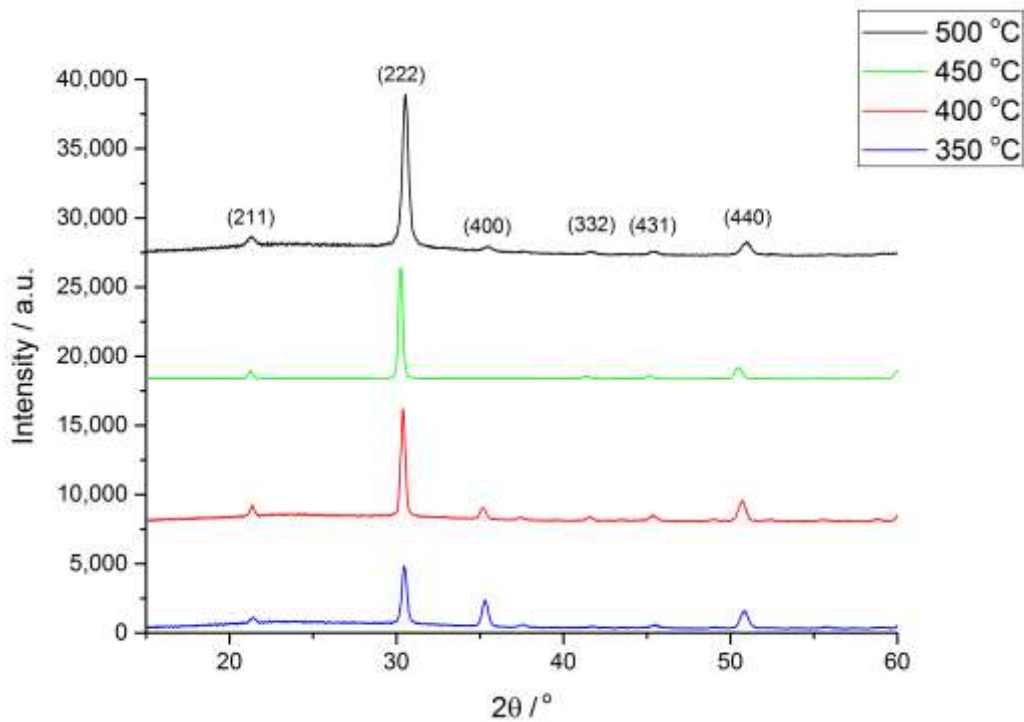


Figure 4-16: XRD patterns obtained for In_2O_3 films deposited by AACVD from the *in situ* reaction of $\text{InMe}_3/\text{HOCH}_2\text{CH}_2\text{NMe}_2$ in MeOH at temperatures between 350 – 500 °C.

4.6.2 Lattice Parameters

The powder XRD data was used to calculate the lattice parameters. The fitting process used the Le Bail model where refinement is limited to (HKL) lines defined by the cell and space group. GSAS with EXPGUI, a graphical user interface editor was performed to control the progression of the equally weighted fitting to obtain unit cell parameters. The model was based on an indium oxide framework, with a starting indium oxide lattice parameter of 10.117 Å.

The lattice parameter calculated for the as-deposited In_2O_3 films are displayed in Table 4-4. Most of the films match with the literature value of 10.117 Å for In_2O_3 . However, films deposited at lower temperatures (350 – 400 °C) have smaller lattice parameter values calculated than expected. This decrease could be attributed to an increase in oxygen deficiencies in the lattice resulting in an increase in repulsion.¹⁴⁴

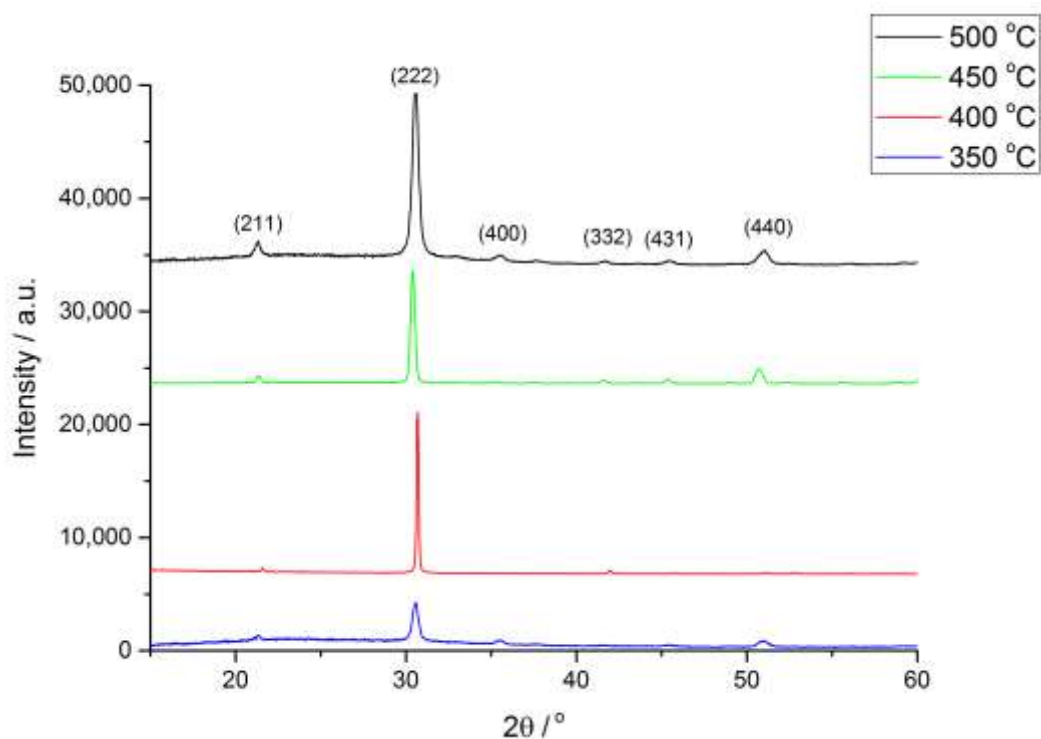


Figure 4-17: XRD patterns obtained for In_2O_3 films deposited by AACVD from the in situ reaction of $\text{InMe}_3/\text{MeOH}$ at temperatures between 350 – 500 °C.

Table 4-4: Experimental conditions and resultant characterisation for In_2O_3 films deposited.

	Reactions	Temp/ °C	a/Å	Fitted wRp	% Trans
A	$\text{InMe}_3 / \text{HOCH}_2\text{CH}_2\text{OH} / \text{MeOH}$	400	9.982 (5)	0.0807	74 – 92
	$\text{InMe}_3 / \text{HOCH}_2\text{CH}_2\text{OH} / \text{MeOH}$	450	10.093 (7)	0.1074	42 – 51
	$\text{InMe}_3 / \text{HOCH}_2\text{CH}_2\text{OH} / \text{MeOH}$	500	10.143 (3)	0.0599	72 – 93
B	$\text{InMe}_3 / \text{HOCH}_2\text{CH}_2\text{NMe}_2 / \text{MeOH}$	350	10.163(1)	0.0645	77 – 83
	$\text{InMe}_3 / \text{HOCH}_2\text{CH}_2\text{NMe}_2 / \text{MeOH}$	400	10.176(1)	0.0673	55 – 66
	$\text{InMe}_3 / \text{HOCH}_2\text{CH}_2\text{NMe}_2 / \text{MeOH}$	450	10.233(1)	0.0921	80 – 87
	$\text{InMe}_3 / \text{HOCH}_2\text{CH}_2\text{NMe}_2 / \text{MeOH}$	500	10.144(3)	0.0894	80 – 89
C	$\text{InMe}_3 / \text{MeOH}$	350	10.128(1)	0.0766	91 – 95
	$\text{InMe}_3 / \text{MeOH}$	400	10.094(1)	0.0998	71 – 88
	$\text{InMe}_3 / \text{MeOH}$	450	10.184(1)	0.0917	80 – 88
	$\text{InMe}_3 / \text{MeOH}$	500	10.145(3)	0.0835	81 – 89

4.6.3 Optical properties

The optical properties were investigated using transmission and reflectance measurements between 300 – 2300 nm and UV/Visible measurements between wavelengths of 300 – 1000 nm. All the In_2O_3 films displayed minimal reflectivity (5 – 10 %) and high transmissions (71 – 95%) for most of the films. Generally, the films using MeOH as the oxygen source as well as the solvent had higher transmissions on average than the others. This could be due to less carbon contamination due to less organic compounds used at the start of the deposition. In the visible region, the reflectance was high (80 – 90%) for all the In_2O_3 films. For TCOs, the transmission needs to be >85%.

Using the UV/visible data, a Tauc plot was constructed to calculate the band gap of the In_2O_3 films. All the films had band gaps varying between 3.5 – 3.7 eV which is comparable with literature values of In_2O_3 (~3.7 eV).¹⁶⁶

4.6.4 Morphology of In_2O_3 Films

The morphology of the In_2O_3 films was investigated using SEM. It was previously described how precursor and solvent can have an effect on the microstructure of the films. For these films, different morphologies were observed with a change of temperature (all other conditions the same). Fig. 4-18 show how the increase in temperature change the morphology from small particles (~100 nm) to larger particles (~400 nm) and then into needle-like clusters. This is in contrast with morphology observed from $\text{InMe}_3/\text{HOCH}_2\text{CH}_2\text{OH}$ and $\text{InMe}_3/\text{HOCH}_2\text{CH}_2\text{NMe}_2$ in MeOH.

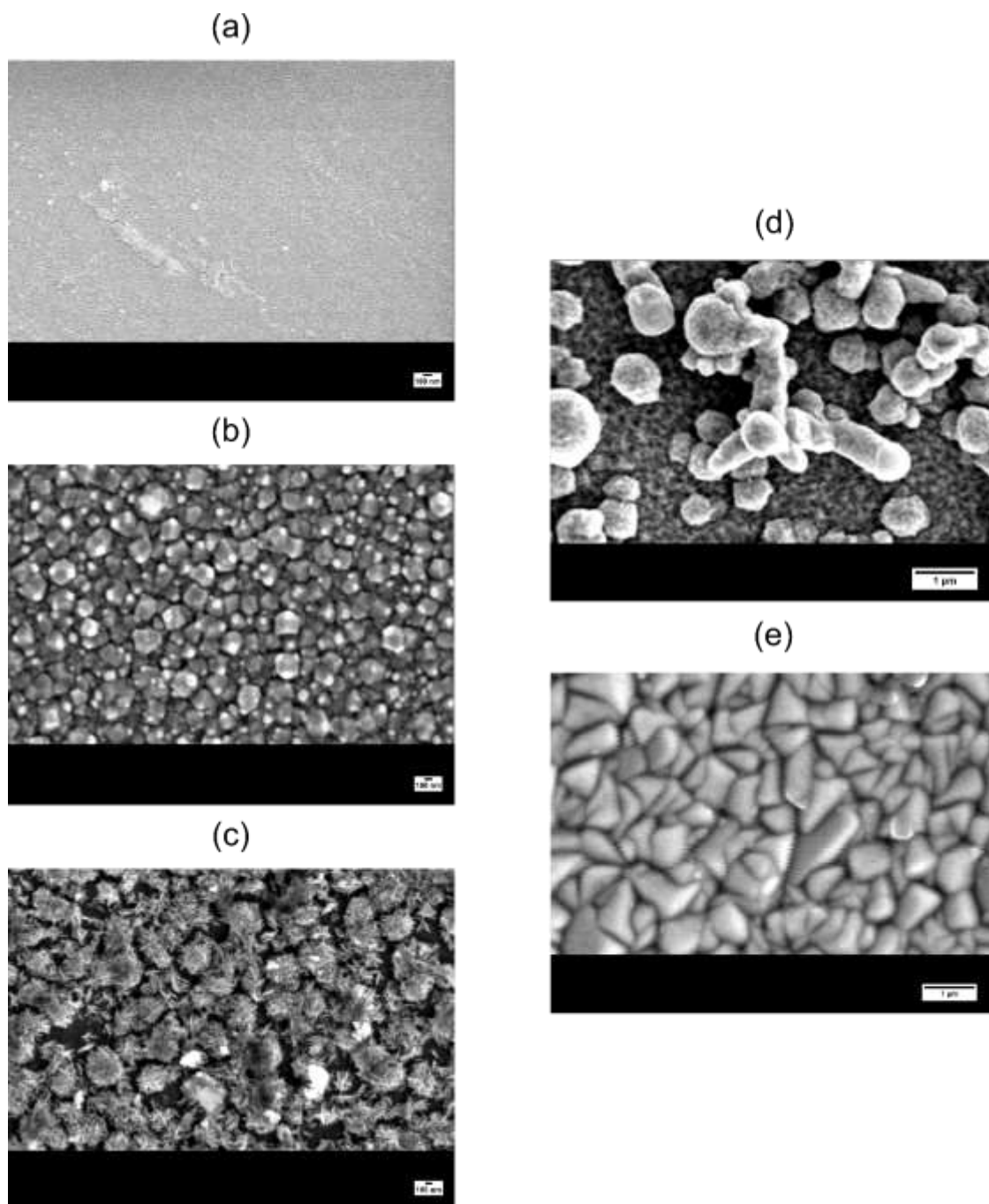


Figure 4-18: SEM images of films grown from $\text{InMe}_3/\text{MeOH}$ at a) 400 °C, b) 450 °C, and c) 500 °C, d) Film grown from $\text{InMe}_3/\text{HOCH}_2\text{CH}_2\text{OH}$ in MeOH at 450 °C and e) film grown from $\text{InMe}_3/\text{HOCH}_2\text{CH}_2\text{NMe}_2$ in MeOH at 450 °C.

Films deposited using the diol (HOCH₂CH₂OH) had a microstructure consisting of much larger particles ranging from 0.5 – 1 μm, whereas the films using the donor-functionalised alcohol had spherical agglomeration and an even coverage. These results indicate that not only the alcohol and solvent used have an effect on the morphology but also on the temperature of deposition does as well.

Further analysis of the films was carried out on the best films (in terms of surface coverage and transmission) which were InMe₃/HOCH₂CH₂NMe₂ in MeOH and InMe₃/MeOH deposited at 450 °C, to investigate the functional properties.

Film thickness measurements were obtained on the chosen films using side-on SEM. The film thickness for the films deposited at 450 °C from InMe₃/HOCH₂CH₂NMe₂ in MeOH and InMe₃/MeOH were 750 and 250 nm respectively (Fig. 4-19). This indicates that the films deposited using the donor-functionalised alcohol produced thicker films. This could be due to the increase solubility of the *in situ* precursor formed.

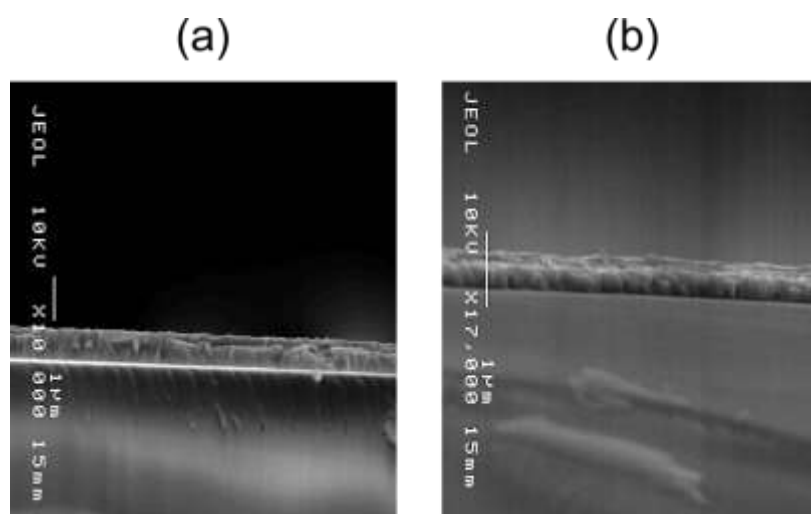


Figure 4-19: Side-on SEM images of films grown at 450 °C from a) InMe₃/HOCH₂CH₂NMe₂ in MeOH and b) InMe₃/MeOH.

4.6.5 Preferred Orientation

The degree of preferred orientation using Bragg's crystal plane was determined using the calculation of the texture coefficient. The reflections analysed for the In₂O₃ films were 211, 222, 400, 332, 431 and 440. The texture coefficient was calculated using the following equation:

$$TC_{(hkl)} = \frac{I_{(hkl)} / I_{o(hkl)}}{\frac{1}{N} \sum_N I_{(hkl)} / I_{o(hkl)}} \quad (4.1)$$

The texture coefficient (TC) of a given (hkl) plane, I is the experimental relative intensity, I_o is the reference intensity and N is the number of reflections. Table 4-5 show the extent of preferred orientation for each particular peak seen on the XRD. It is seen that In₂O₃ film deposited from InMe₃/MeOH at 400 °C are orientated in the [400] direction but the increase in temperature to 450 °C changes the orientation to [440] direction. As the temperature increases to 500 °C, the orientation changes again to the [222] direction. This change from (440) to (400) to (222) as the temperature increases has been since for the deposition of In₂O₃. This change in preferred orientation can be related to the morphology observed in Fig. 4-18 from In₂O₃ films with small particles to needle-like clusters.

Table 4-5: Texture coefficient intensity ratio for XRD peaks obtained from films deposited from InMe₃/MeOH.

	211	222	400	332	431	440
400 °C	0.33	0.12	1.22	0.18	1.31	4.04
450 °C	0.47	0.32	4.17	0.39	0.65	0.88
500 °C	0.35	1.91	0.48	0.47	0.99	1.81

The preferred orientation (Table 4-6) were calculated for these XRD patterns and the film deposited with InMe₃/MeOH with either HOCH₂CH₂OH or HOCH₂CH₂NMe₂ at 450 °C. The preferred orientation is similar to the In₂O₃ grown at 450 °C without

additional oxygen source in the [400] directions. Even though all the films grown at 450 °C have grown in the same direction, the morphology is very different.

Table 4-6: Texture coefficient intensity ratio for XRD peaks obtained from In_2O_3 films deposited using a diol or donor functionalised alcohol at 450 °C.

	211	222	400	332	431	440
InMe₃/ HOCH₂CH₂OH/ MeOH	1.00	1.41	2.09	0.60	0.89	1.47
InMe₃/ HOCH₂CH₂NMe₂/ MeOH	0.35	0.48	1.91	0.47	0.99	1.81

4.6.6 Raman Analysis

Raman patterns were taken of these two best In_2O_3 films in terms of surface coverage and transmission (films deposited at 450 °C from $\text{InMe}_3/\text{HOCH}_2\text{CH}_2\text{NMe}_2$ in MeOH and $\text{InMe}_3/\text{MeOH}$). Characteristic In_2O_3 peaks were observed with the strongest band appearing at $\sim 360 \text{ cm}^{-1}$ with a weaker band at 307 cm^{-1} . These matched well with Raman bands previously reported. The Raman pattern also identified the presence of graphitic carbon in the films.¹⁹⁸

4.6.7 Electric Properties

Initially the films were tested using a two point probe which indicated a decrease in resistivity as temperature increased. Once again the two best films were tested further; films deposited at 450 °C from $\text{InMe}_3/\text{HOCH}_2\text{CH}_2\text{NMe}_2$ in MeOH and $\text{InMe}_3/\text{MeOH}$. Linear van der Pauw four point probe technique was used to measure the electrical resistance.¹⁹⁹ A current (I) was applied across two outer probes and a potential difference (v) measured across two inner probes. The negligible contact and spreading resistance associated with the voltage probes allows sheet resistance, R_s to be calculated using the following equation:

$$R_s = 4.53 \frac{v}{I} \quad (4.2)$$

The sheet resistance is defined as the resistance of one square of film and is independent of the square size. The resistance was measured at up to 9 points across the surface of each film. The measurements were taken at the centre of the film to ensure that enough film was present to provide a good flow of current and potential difference.²⁰⁰ The as-deposited In₂O₃ films show a low sheet resistance (Table 4-7) indicating a high electrical conductivity. Sheet resistivity was also calculated using the following equation (4.3) where R_s is the sheet resistance and d is the film thickness.

$$\rho = R_s d \quad (4.3)$$

Sheet resistivity of R_s = 3.44 and 4.88 Ω□⁻¹ for the InMe₃/MeOH and InMe₃/HOCH₂CH₂NMe₂ in MeOH films respectively were observed. Higher value of sheet resistance were obtained from films deposited with HOCH₂CH₂NMe₂. The presence of the donor-functionalised alcohol has therefore had an effect on the electrical properties of this In₂O₃ films.

In order to understand more about the electrical properties of the films, detailed measurements of the Hall mobility and carrier concentrations were carried out. Hall effect measurements showed that the films exhibited n-type conductivity indicating that electrons were the dominant charge carrier species.

For films deposited using InMe₃/MeOH a specific resistivity (ρ) of 8.60 x 10⁻⁵ Ωcm and a charge carrier concentration (n) of 9.3 x 10²⁰ cm⁻³ was obtained. The mobility of the charge carrier (μ) were 77 cm² V⁻¹ s⁻¹. The results for the films deposited from InMe₃/HOCH₂CH₂NMe₂ in MeOH were similar with specific resistivity of 3.66 x 10⁻⁵ Ωcm and a charge carrier concentration of 2.12 x 10²⁰ cm⁻³ and charge carrier mobility was 79.9 cm² V⁻¹ s⁻¹. Low electrical resistivity is often described as that in the order of 10⁻⁴ Ωcm. These undoped In₂O₃ films have an electrical resistivity which is comparable to that of doped In₂O₃ films.

Table 4-7: Electrical properties of films grown from $\text{InMe}_3/\text{HOCH}_2\text{CH}_2\text{NMe}_2$ in MeOH and $\text{InMe}_3/\text{MeOH}$ at 450 °C.

Film	R_s / Ωcm^{-1}	d /nm	ρ / Ωcm	μ / $\text{cm}^2 \text{V}^{-1} \text{s}^{-1}$	n / cm^{-3}
$\text{InMe}_3/\text{HOCH}_2\text{CH}_2\text{NMe}_2$	4.88	750	3.66×10^{-5}	77	9.3×10^{20}
$\text{InMe}_3/\text{MeOH}$	3.44	250	8.60×10^{-5}	79.9	2.12×10^{20}

The electrical conductivity of a material relies on the number of charge carriers and the mobility of the charge. TCOs currently used have systems with n ranging between $10^{20} - 10^{21} \text{ cm}^{-3}$ and μ for an n-type material of $10 - 40 \text{ cm}^2 \text{V}^{-1} \text{s}^{-1}$.²⁰¹ It can be seen that the inclusion of the donor functionalised alcohol improves conductivity and results obtained from these In_2O_3 films are comparable to In_2O_3 films deposited using similar procedure with $n = 1 \times 10^{20} \text{ cm}^{-3}$ and $\mu = 71 \text{ cm}^2 \text{V}^{-1} \text{s}^{-1}$. When compared to other doped TCOs such as $\text{Mo}:\text{In}_2\text{O}_3$, $n = 4 \times 10^{20} \text{ cm}^{-3}$ and $\mu = 119 \text{ cm}^2 \text{V}^{-1} \text{s}^{-1}$ these undoped In_2O_3 had better conductivity.²⁰¹⁻²⁰³ Some of the parameters calculated are ideal for TCO materials however the carrier mobility for both films need to improve when compared to current commercial material.

These results indicate that these high conductivity undoped In_2O_3 are suitable candidates for TCO materials. The origin of the high conductivity is unknown but has been seen previously. It was shown that surface donors dominate the conductivity rather than the bulk defects.²⁰⁴

4.7 Conclusion

This investigation used different types of oxygen sources; diols, donor functionalised alcohol and alcohol. Using this range of oxygen sources produce different quality of films and morphology. The most transparent, adherent films were the amorphous Ga_2O_3 deposited from $\text{GaMe}_3/\text{MeOH}$ via AACVD. Copper gallium oxide thin films were deposited using $\text{GaMe}_3/\text{Cu}(\text{NO}_3)_2 \cdot 3\text{H}_2\text{O}/\text{MeOH}$. An amorphous material was deposited that was identified as $\text{Ga}_2\text{O}_3\text{-Cu}_2\text{O}$. The antimicrobial efficacy of transparent Ga_2O_3 and $\text{Ga}_2\text{O}_3\text{-Cu}_2\text{O}$ films tested against *E. coli* and *S. aureus*. It was seen that the Ga_2O_3 films possessed antibacterial activity but $\text{Ga}_2\text{O}_3\text{-Cu}_2\text{O}$ were significantly more potent.

Further investigation were undertaken using different oxygen sources and solvents with InMe_3 to deposit In_2O_3 . Similar results were seen with different microstructure observed that affected the TCO properties. The Hall effect measurements were carried out and saw that these In_2O_3 films deposited from $\text{InMe}_3/\text{MeOH}$ and $\text{InMe}_3/\text{HOCH}_2\text{CH}_2\text{NMe}_2/\text{MeOH}$ had conductivity similar to doped In_2O_3 . These undoped In_2O_3 have the potential to be TCO materials.

5

Zinc Oxide

The following chapter presents the results obtained from the deposition of zinc oxide and copper doped zinc oxide thin films and the investigation of the different properties of the films. The films were deposited using AACVD and Dual Source AACVD. The thin films materials were fully characterised and tested for their antimicrobial properties using serial dilution and viable colony counts on to agar plates.

5. Introduction

Chapter 4 discussed the theory and properties of transparent conductive oxides (TCOs) of indium oxide. Zinc oxide (ZnO) is also a very common TCO that is used widely in industry. Alternatives TCOs to indium-tin-oxide (ITO) are being investigated due to the worldwide depletion of indium.²⁰⁵ ZnO is becoming more widely used for many different applications. ZnO thin films are of high interest due to its TCO properties, the ability to have high transparency as well as high electrical conductivity. ZnO is a n-type semiconductor with a wide band gap of 3.3 eV and has high optical transmittance over a wide spectrum and low resistivity. Research suggests that the high conductivity of ZnO is due to oxygen vacancies or interstitial Zn atoms present. Aluminium, one of the most commonly used dopants for ZnO (AZO), yields typical resistivities between $1 - 3 \times 10^{-4} \Omega\text{cm}$.^{206,207}

ZnO has a wurtzite structure with lattice parameters, $a = 3.28 \text{ \AA}$ and $c = 5.206 \text{ \AA}$. The structure comprises of alternative planes of fourfold coordinated O^{2-} and Zn^{2+} ions that are stacked along the c-axis alternately. The electrical properties of ZnO are influenced by the oxygen vacancies and additional zinc atoms that are located in the interstitial sites. Doping of ZnO is common in order to improve the electrical properties.

5.1 Antimicrobial Activity of Zinc Oxide

Zinc is an essential metal in many microorganisms due to its involvement in many cellular reactions.²⁰⁸ Zn^{2+} ions are non-toxic towards many microorganisms at low concentrations. However, above $10^{-7} \text{ mol L}^{-1}$, homeostasis allows for Zn^{2+} to penetrate into cells and become cytotoxic.²⁰⁹ It has been proposed that direct contact of ZnO particles can destabilise bacterial membranes upon direct contact.^{210,211} The intrinsic antimicrobial properties of Zn^{2+} have been investigated. There have been studies describing the antimicrobial activity of ZnO however, the exact mechanism is not known. Many mechanisms for antimicrobial activity have been suggested. One possible mechanism is the generation of

hydrogen peroxide and reactive oxygen species (ROS). The generation of hydroxyl radicals by the reactions between oxygen and water can lead to damage to cell membranes, proteins, and DNA, which can ultimately lead to the death of the cell.²¹²⁻²¹⁷

Hydrogen peroxide can be toxic due to Fenton-type reactions (discussed in chapter 3). Studies have also shown that the production of ROS can be different in the dark and when exposed to visible light. Results exhibited that the antibacterial activity of ZnO was reduced when not exposed to light. Further investigation indicated that the level of ROS increased by 400% when illuminated.^{216,218}

5.1.1 Zinc Oxide Deposition

In this chapter, the antimicrobial activity of zinc oxide and copper doped zinc oxide deposited via AACVD will be discussed. Zinc oxide films have deposited using different variation of CVD,^{219,220} sol-gel²²¹ and magnetron sputtering.²²² The doping of zinc oxide with copper is of increasing interest in research due to the different properties that are exhibited. Most research on the antimicrobial activity of ZnO is a nanomaterials. It is of interest to see how ZnO thin films compare.

This investigation describes the deposition of copper doped zinc oxide thin film via AACVD, and the assessment of the antimicrobial activity of the resulting films. The zinc precursors that are being investigated are Zinc nitrate hexahydrate [Zn(NO₃)₂·6H₂O], and Zinc acetate dihydrate, [Zn(OAc)₂·2H₂O]. To dope copper into the ZnO films, the copper precursors investigated in chapter 3, which are copper nitrate [Cu(NO₃)₂·3H₂O], copper acetylacetonate [Cu(acac)₂], and copper acetate [Cu(OAc)₂·H₂O] were used. The concentration of copper incorporated into ZnO will be increased to see if there is an increase or decrease in antimicrobial effectiveness. The colour, transparency and reproducibility will be analysed in order to investigate the most appropriate thin films for antibacterial coatings.

5.2 Experimental

All chemicals used in this report were purchased from Sigma-Aldrich Chemical Co. Nitrogen (99.99%) was obtained from BOC and was used as supplied. Deposition was on microscope slides or 150 × 45 × 45 mm SiO₂ coated float-glass (the SiO₂ acts as a barrier layer preventing diffusion of ions from within the glass into the deposition film) which has been supplied by Pilkington NSG. Prior to use the glass substrate were cleaned with acetone and isopropanol and temperature was monitored during the deposition using a Pt–Rh thermocouple.

Nitrogen was passed through a two-way tap, which was used to divert the nitrogen carrier gas through a glass bubbler. All deposition experiments were conducted by heating the cold-wall horizontal-bed reactor to the required temperature before diverting the nitrogen line through the aerosol into the reactor. The aerosol was carried into the reactor in a stream of nitrogen gas through a brass baffle to obtain a laminar flow. The gas flow was continued until all of the precursor mix had passed through the reactor, typically 1 h. The glass substrate was allowed to cool with the graphite block under a flow of nitrogen until it reached room temperature before it was removed.

5.2.1 AACVD of [Zn(NO₃)₂·6H₂O] and [Cu(NO₃)₂·3H₂O]

Zinc nitrate hexahydrate [Zn(NO₃)₂·6H₂O, 1.68 mmol] and copper nitrate trihydrate [Cu(NO₃)₂·3H₂O, 0.9 mmol] were added to methanol (30 mL). An aerosol was generated at room temperature using a humidifier with the graphite heating block under the glass substrate heating the CVD reactor to 450 °C. The film was allowed to cool under a flow of N₂ until room temperature. A yellow film with very poor coverage was deposited.

5.2.2 AACVD of [Zn(NO₃)₂·6H₂O] and [Cu(acac)₂]

Zinc nitrate hexahydrate [Zn(NO₃)₂·6H₂O, 1.68 mmol] and copper nitrate [Cu(acac)₂, 1.91 mmol] were added to acetone (30 mL). Solution was allowed to mix for 30 minutes using a sonicator. The graphite heating block under the glass

substrate was heated to 450 °C. An aerosol was generated at room temperature using a humidifier. Once the entire aerosol had passed through and had finished, the films were allowed to cool under N₂. A yellow film was produced with very poor coverage.

5.2.3 AACVD of [Zn(OAc)₂·2H₂O] and [Cu(NO₃)₂·3H₂O]

Zinc acetate dihydrate, [Zn(OAc)₂·2H₂O, 2.28 mmol] and copper nitrate trihydrate [Cu(NO₃)₂·3H₂O, 0.9 mmol] were added to MeOH (30 mL). The resulting solution was allowed to mix in the AACVD bubbler. An aerosol was generated at room temperature using a humidifier with the graphite block under the glass substrate heating the CVD reactor to 450 °C. The film was allowed to cool under a flow of N₂ until room temperature. A yellow transparent thin film with 25% coverage of the substrate was produced.

5.2.4 AACVD of [Zn(OAc)₂·2H₂O] and [Cu(acac)₂]

Zinc acetate dihydrate, [Zn(OAc)₂·2H₂O, 2.28 mmol] and copper(II) acetylacetonate, [Cu(acac)₂, 1.91 mmol] were added to acetone or MeOH in separate experiments. After addition the solid was allowed to mix for 15 minutes and used immediately for AACVD deposition. An aerosol was generated using a humidifier. The graphite heating block under the glass substrate was heated to 450 °C. Once deposition was completed the substrate was cooled to room temperature. Not all the Cu(acac)₂ were able to dissolve in the methanol and some of the precursor was left behind in the AACVD bubbler once the deposition was complete. Deposition using acetone produced a blue film with 25% coverage of the substrate was produced. For deposition using methanol, a green film with good coverage was produced.

5.2.4.1 AACVD of [Zn(OAc)₂·2H₂O] and [Cu(acac)₂] (high concentration)

Zinc acetate dihydrate, [Zn(OAc)₂·2H₂O, 4.56 mmol] and Copper(II) acetylacetonate, [Cu(acac)₂, 3.44 mmol] were added to MeOH. The same condition

as reaction 5.2.4 was carried out. A dark green film was deposited with a metallic copper tinge that covered the entire substrate.

5.2.4.2 AACVD of [Zn(OAc)₂·2H₂O] and [Cu(acac)₂] (low concentration)

Zinc acetate dihydrate, [Zn(OAc)₂·2H₂O, 1.14 mmol] and copper(II) acetylacetonate, [Cu(acac)₂, 0.96 mmol] were added to MeOH. The same condition as reaction 5.2.4 was carried out. A dark green film was deposited with a metallic copper tinge that covered the entire substrate. A green film was deposited with good coverage.

5.2.4.3 AACVD of [Zn(OAc)₂·2H₂O] with [Cu(acac)₂] with CTAB (high concentration)

The conditions of reaction 5.2.4 were repeated only using methanol with the addition cetyl trimethylammonium bromide, CTAB [(C₁₆H₃₃)N(CH₃)₃Br, 0.55 mmol] producing dark green film with poor coverage.

5.2.4.4 AACVD of [Zn(OAc)₂·2H₂O] with [Cu(acac)₂] with CTAB (low concentration)

The conditions of reaction 5.2.4.3 was repeated with the change of CTAB, [(C₁₆H₃₃)N(CH₃)₃Br, 0.055 mmol] concentration. A green thin film was produced with metallic copper colour at the bottom of the substrate.

5.2.4.5 AACVD of [Zn(OAc)₂·2H₂O] with [Cu(acac)₂] and HOCH₂CH₂OMe

The conditions of reaction 5.2.4 was repeated only using methanol with the addition of HOCH₂CH₂OMe (0.1 mL) to the solution. A very dark green film was deposited that covered the majority of the substrate.

5.2.5 AACVD of [Zn(OAc)₂·2H₂O] with methanol

Zinc acetate dihydrate, [Zn(OAc)₂·2H₂O, 2.28 mmol] was mixed with 30 mL of MeOH. An aerosol was generated at room temperature using a humidifier with the graphite heating block under the glass substrate heating the CVD reaction to 350 – 450 °C in separate experiments. The film was allowed to cool under a flow of N₂

until it reached room temperature. At each temperature, a transparent film was deposited.

5.2.6 AACVD of [Zn(OAc)₂·2H₂O] and [Cu(OAc)₂·H₂O]

Zinc acetate dihydrate, [Zn(OAc)₂·2H₂O, 2.28 mmol] and copper acetate [Cu(OAc)₂·H₂O, 0.043 mmol] were added to MeOH (30 mL). The resulting blue solution was mixed until all precursor had dissolved. An aerosol was generated at room temperature using a humidifier with graphite heating block under the glass substrate heating the CVD reactor to 350 and 450 °C in separate experiments under a flow of N₂. Once the deposition was complete the film was allowed to cool to room temperature. At each temperature, a transparent green film was deposited.

5.2.7 Dual source AACVD of [Zn(OAc)₂·2H₂O] and [Cu₂(OAc)₂·H₂O]

Dual source AACVD was set up with two separate bubblers. In one bubbler, zinc acetate dihydrate, [Zn(OAc)₂·2H₂O, 2.28 mmol] was mixed with MeOH (30 mL) and the second bubbler had [Cu₂(OAc)₂·H₂O, 0.043 mmol] and MeOH (30 mL) mixture. Both AACVD bubblers were attached to the reactor separately via a Y-junction. Aerosols were formed for each AACVD bubbler using two humidifiers with the graphite heating block under the glass substrate heating the CVD reactor to 350 – 450 °C in separate experiments. Once deposition was complete, the films were allowed to cool to room temperature under a flow of N₂. At each temperature, a transparent green film was deposited.

5.2.7.1 Dual source AACVD of [Zn(OAc)₂·2H₂O] and [Cu(acac)₂]

Dual source AACVD was set up described in reaction 5.2.7. In one bubbler, Zn(OAc)₂·2H₂O, (2.28 mmol) was mixed with MeOH (30 mL) and the other bubbler had a mix of Cu(acac)₂, (1.91 mmol) in MeOH (30 mL). The graphite heating block under the glass substrate was heated to 400 °C. Once the deposition was complete, a green uniform film was produced.

5.2.7.2 Dual source AACVD of [Zn(OAc)₂·2H₂O] and [Cu(OAc)₂·H₂O] – differing Cu concentration

Dual source AACVD was set up as described in reaction 5.2.7. The concentration of zinc acetate remained constant in one AACVD bubbler. In the other, the concentration of copper acetate (0.022 – 0.41 mmol) mixed with MeOH (30 mL) was varied. This resulted in 1 – 18% copper solutions for a separate 9 experiments. The graphite heating block under the glass substrate was heated to 350 - 450 °C. Once deposition was completed the substrate was cooled to room temperature. As the concentration of copper increased, the colour of the films become more pronounced, the films became a darker green.

5.2.8 Characterisation

The resulting zinc oxide and copper-doped zinc oxide films were handled and stored in air. The coated glass substrates were used for powder X-ray diffraction (XRD) and then were cut into 1 cm × 1 cm squares for subsequent analysis by Scanning Electron Microscopy (SEM), on a JEOL 6301 filament scanning electron microscope. A Perkin-Elmer Lambda 25 UV-Vis Spectrometer was used to measure the UV-Vis absorption spectra of the samples. Reflectance and transmission spectra were recorded between 300 – 2300 nm by a Zeiss miniature spectrometer. Reflectance measurement were standardised relative to a rhodium mirror and transmission relative to air. Raman spectroscopy was performed using a Renishaw 1000 spectrometer equipped with a 514.5 nm laser.

X-ray photoelectron spectroscopy (XPS) was performed using a Thermo Scientific K-alpha photoelectron spectrometer using monochromatic Al_{Kα} radiation. Samples were earthed using copper tape. Higher resolution scans were recorded for the principal peaks of Cu(2p), Zn(2p), O(1s) and C(1s) at a pass energy of 50 eV. The peaks were modelled using CasaXPS software with binding energies adjusted to adventitious carbon (284.5 eV) for charge correction.

Dr Husn-Ubayda Islam performed X-ray absorption spectroscopy (XAS) measurements on the Dutch-Belgian Extended X-ray absorption fine structure (EXAFS) beamline (BM26A) at the ESRF in Grenoble. Monochromatic radiation was supplied by a double Si(111) crystal, and fluorescence was measured using a 9 element germanium solid state detector. XAS of the film was acquired in fluorescence. Measurements of the thin film and pelletized copper standards were taken on the copper K-edge (8987eV). XAS data were processed and X-ray absorption near edge structure (XANES) analysis was performed using Horae Athena software, and detailed EXAFS analysis was performed on Excurve version 9.273.

5.2.9 Antimicrobial activity

E. coli strain (ATCC 25922) was maintained by weekly subculture on Brain Heart Infusion (BHI) agar (Oxoid, Basingstoke, UK). *E. coli* was used to inoculate 10 mL of sterile BHI broth (Oxoid, Basingstoke, UK) and incubated aerobically at 37 °C for 24 hours. Bacteria from the overnight culture were harvested by centrifugation at 13000 × g for 1 minute. *E. coli* was then re-suspended in phosphate-buffered saline (PBS) (Oxoid, Basingstoke, UK) and again centrifuged at 13,000 × g for 1 minute. Finally the bacterial pellet was re-suspended in PBS before use. The turbidity of the bacterial cell suspension was measured at 600 nm using a spectrophotometer and was adjusted to an optical density which corresponded to approximately 10⁵ colony forming units (cfu) per 25 µL aliquot.

Prior to use, the zinc oxide and copper zinc oxide slides were cut into 1 × 1 cm sections. A humidity chamber was created to ensure that the suspensions did not dry out. A 25 µL aliquot of the bacterial cell suspension was spread evenly on the surface of each slide and incubated at room temperature (21 ± 2 °C) for the allocated exposure time. For each exposure time (3, 6 and 18 hours), triplicate samples were analysed and uncoated glass microscope slides were used as a control. The samples were then irradiated for up to 18 hours using a white light

source (General Electric 28 W Watt Miser™ T5 2D compact fluorescent lamp) emitting an average light intensity of 3,750 250 lux at a distance of 30 cm from the samples. A further set of samples (in triplicate) was maintained in the dark for the duration of the irradiation time. Each exposure time was also repeated on two separate occasions

After incubation the slides were aseptically transferred to 225 µL PBS and vortexed for 30 seconds to release the bacteria into the solution. Serial dilutions of the resulting bacterial suspensions were prepared in PBS and 25 µL from each dilution was spread on to MacConkey Agar (Oxoid, Basingstoke, UK). Plates were incubating aerobically at 37 °C for 24 hours. After incubation, any bacterial colonies were counted and viable counts of bacteria were calculated. Mann-Whitney U test was used to determine the significance of the activity of zinc oxide or copper zinc oxide slides compared to the glass control.

5.3 Results and Discussion

Initially a range of copper and zinc precursors were investigated to study which precursors deposited copper doped zinc oxide thin films and with good coverage. Zinc nitrate and zinc acetate are readily available zinc precursors for single-source deposition of zinc oxide thin films while maintaining transparency in order to test their antimicrobial effectiveness. Copper nitrate, copper(II) acetylacetonate, and copper acetate are also readily available to deposit copper thin films (see chapter 3). These copper precursors were used to dope copper into zinc oxide. Along with the change of precursors, temperature, and solvent were also investigated.

Table 5-1: *The results of using a variety of zinc and copper precursors and solvents.*

	Zinc Precursor	Copper Precursor	Solvent	Film	Film Appearance
A	<i>Zinc Nitrate, [Zn(NO₃)₂·6H₂O]</i>	<i>Copper nitrate, [Cu(NO₃)₂·3H₂O]</i>	MeOH	ZnO/CuO	Small brown/yellow patches
B		<i>Copper(II) acetylacetonate, [Cu(acac)₂]</i>	Acetone	Non-crystalline	Small yellow patches
C	<i>Zinc Acetate, [Zn(OAc)₂·2H₂O]</i>	<i>Copper nitrate, [Cu(NO₃)₂·3H₂O]</i>	MeOH	ZnO	Yellow film
D		<i>Copper(II) acetylacetonate, [Cu(acac)₂]</i>	Acetone	ZnO	Transparent green film
E			MeOH	ZnO	Transparent green film

A number of depositions were investigated (Table 5-1) with a change of solvent, zinc and copper precursors. All these factors can influence the composition, coverage and appearance of the desired thin films.

Zinc nitrate, $[\text{Zn}(\text{NO}_3)_2 \cdot 6\text{H}_2\text{O}]$ is soluble in methanol and the first zinc precursor to be investigated. Either copper nitrate, $[\text{Cu}(\text{NO}_3)_2 \cdot 3\text{H}_2\text{O}]$ or copper(II) acetylacetonate, $[\text{Cu}(\text{acac})_2]$ was used to dope copper into zinc oxide using a zinc to copper precursor ratio of 2:1.

Zinc nitrate $[\text{Zn}(\text{NO}_3)_2 \cdot 6\text{H}_2\text{O}]$ and copper nitrate, $[\text{Cu}(\text{NO}_3)_2 \cdot 3\text{H}_2\text{O}]$ were mixed and used at a deposition temperature of 450 °C. The substrate was allowed to cool to room temperature under nitrogen to produce a film. A small film made from patches of brown and yellow was deposited. Powder X-ray diffraction (XRD) data were used to identify a mixture of ZnO and CuO (Fig 5-2a).

In an attempt to produce a film with better coverage, an alternative copper precursor was investigated. Copper(II) acetylacetonate, $[\text{Cu}(\text{acac})_2]$, was added to a solution of $[\text{Zn}(\text{NO}_3)_2 \cdot 6\text{H}_2\text{O}]$ in methanol. The resulting solution was allowed to mix in a sonicator for 15 minutes however, all the $[\text{Cu}(\text{acac})_2]$ did not dissolve in the solution. The same solubility problems with $[\text{Cu}(\text{acac})_2]$ that were encountered in chapter 3 were observed here. A deposition was carried out at 450 °C and the film was allowed to cool to room temperature under nitrogen. Undissolved $[\text{Cu}(\text{acac})_2]$ was left in the AACVD bubbler when deposition was complete. Small patches of yellow films were deposited on the substrate. The films were not crystalline enough to produce a XRD pattern (Fig. 5-2b).

In order to overcome the formation of mixtures and poor film coverage, an alternative zinc precursor was investigated. Zinc acetate dihydrate, $[\text{Zn}(\text{OAc})_2 \cdot 2\text{H}_2\text{O}]$, was added to a solution of copper nitrate, $[\text{Cu}(\text{NO}_3)_2 \cdot 3\text{H}_2\text{O}]$ in methanol. Methanol was chosen since it is a solvent that both zinc acetate and copper nitrate are soluble in and the temperature of deposition was chosen to be 450 °C since previous deposition of metal oxides (chapter 4) have been shown to have the best coverage and reproducible films at that temperature. AACVD of zinc acetate with copper nitrate in methanol was carried out at 450 °C and the substrate was allowed to cool to room temperature under nitrogen. This produced a yellow film with poor coverage. Powder XRD data were used to identify that ZnO was deposited (Fig. 5-3a).

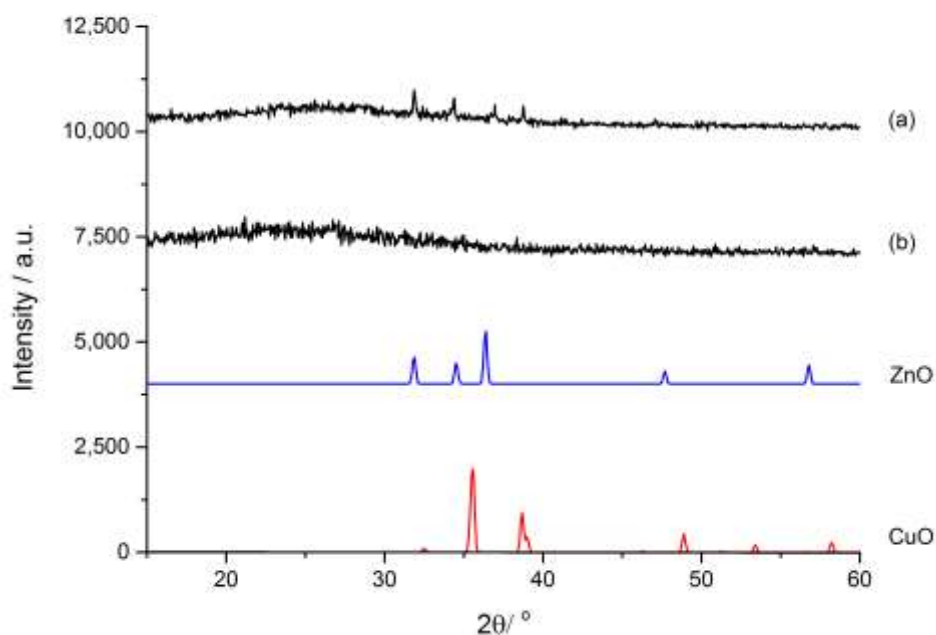


Figure 5-2: XRD patterns of thin films deposited from $Zn(NO_3)_2 \cdot 6H_2O$ at $450\text{ }^\circ C$ with a) $[Cu(NO_3)_2 \cdot 3H_2O]$ and b) $Cu(acac)_2$.

Due to the poor films and mixtures deposited using $[Zn(OAc)_2 \cdot 2H_2O]/[Cu(NO_3)_2 \cdot 3H_2O]$, copper(II) acetylacetonate $[Cu(acac)_2]$ was used again as a copper precursor even with the solubility issue associated with it. $[Zn(OAc)_2 \cdot 2H_2O]$ was added to a solution of $[Cu(acac)_2]$ in acetone or methanol in separate experiments. The resulting solution was allowed to mix in a sonicator for 15 minutes once again, but the copper precursor do not fully dissolve. The deposition was carried out at $450\text{ }^\circ C$ and was allowed to cool to room temperature under nitrogen. At the end of the depositions, some undissolved copper precursor remained. For the deposition using acetone, a transparent film with a blue tinge was deposited with good coverage. Powder XRD data identified the presence of ZnO (Fig. 5-3b). The deposition using methanol produced a green film with good coverage, which was identified as ZnO using XRD data (Fig. 5-3c). However, the colours of the films suggest that Cu may have been incorporated.

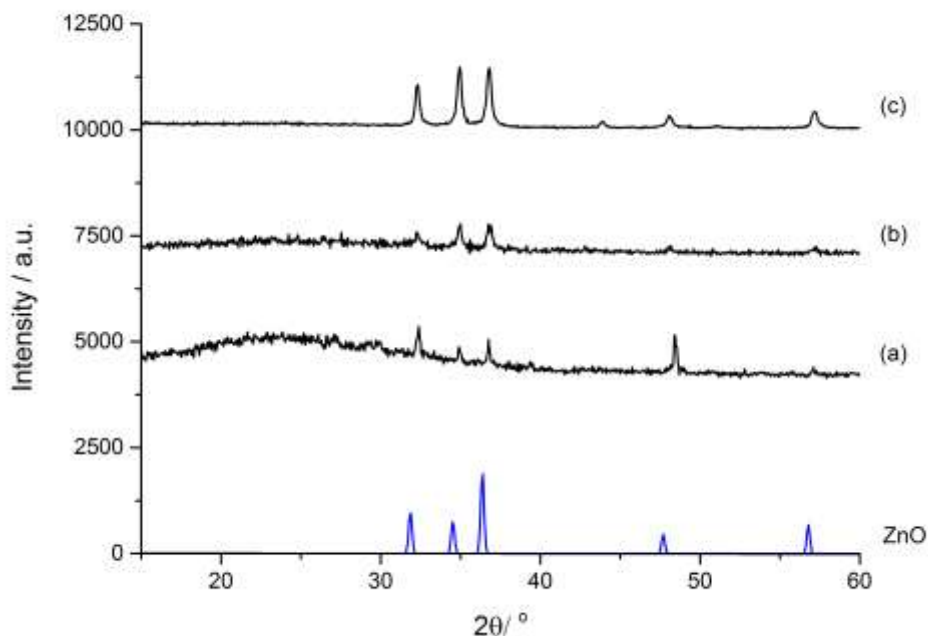


Figure 5-3: XRD patterns of thin films deposited using $[Zn(OAc)_2 \cdot 2H_2O]$ with either a) $[Cu(NO_3)_2 \cdot 3H_2O/MeOH]$, b) $[Cu(acac)_2/acetone]$ and c) $[Cu(acac)_2/MeOH]$.

Research has shown how surfactants can be used as templates for the synthesis of nanomaterials. Surfactants interact with precursors in the gas phase during AACVD deposition which can control the structure and orientation of ZnO. By varying the concentration of surfactants such as cetyl trimethylammonium bromide, $[(C_{16}H_{33})N(CH_3)_3Br]$ known as CTAB, the morphology of the deposited ZnO thin films can be altered.²²³⁻²²⁶

The AACVD deposition of $[Zn(OAc)_2 \cdot 2H_2O]/[Cu(acac)_2]$ in methanol was repeated with the addition of CTAB. The concentration of CTAB was varied between high (0.55 mmol) and low concentrations (0.055 mmol). The resulting solution was allowed to mix in a sonicator for 15 minutes. The deposition was carried out at 500 °C and was allowed to cool to room temperature under nitrogen. At the end of the depositions, some undissolved copper precursor remained in the AACVD bubbler. The high concentration of CTAB produced dark green film with poor coverage whereas, low concentration of CTAB produced green films with better coverage. Powder XRD identified the presence of ZnO for both films (Fig. 5-4).

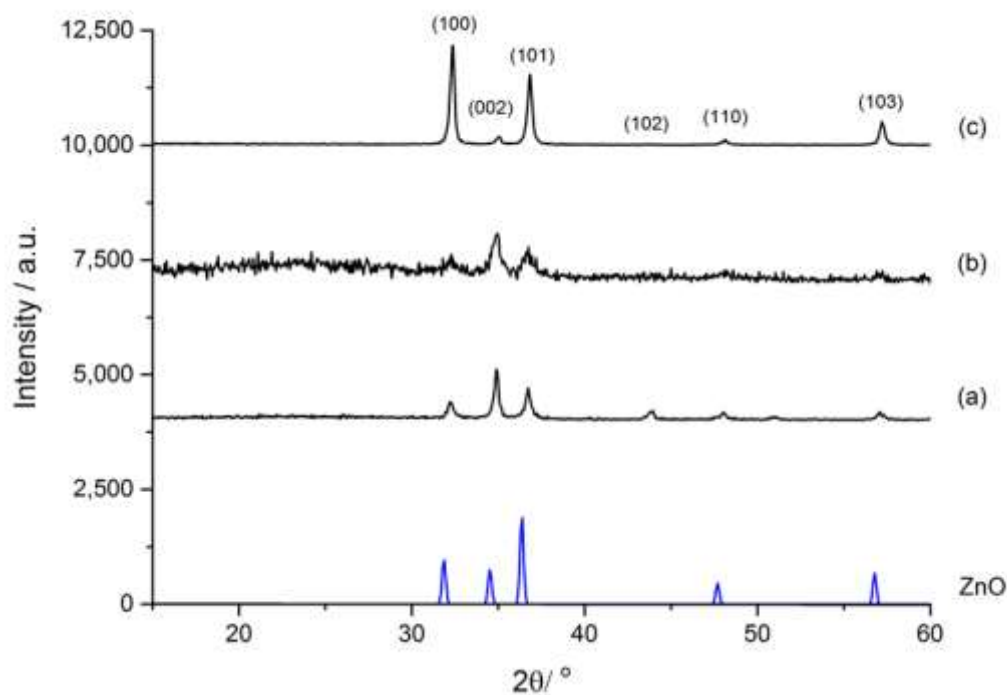


Figure 5-4: XRD patterns of thin films deposited from $\text{Zn}(\text{OAc})_2/\text{Cu}(\text{acac})_2$ with the addition of a) CTAB (low concentration), b) CTAB (high concentration) and c) $\text{HOCH}_2\text{CH}_2\text{OMe}$.

It was previously discussed in chapter 4 that the addition of excess oxygen sources such as donor functionalised alcohols can improve the properties of the as-deposited metal oxide thin films. Donor functionalised alcohols such as $\text{HOCH}_2\text{CH}_2\text{OMe}$ can increase the thickness of the film, producing more adhesive films with better coverage as well as improve TCO properties.

The AACVD deposition of $[\text{Zn}(\text{OAc})_2 \cdot 2\text{H}_2\text{O}]/[\text{Cu}(\text{acac})_2]$ in methanol was repeated with the addition of $\text{HOCH}_2\text{CH}_2\text{OMe}$. The resulting solution was allowed to mix in a sonicator for 15 minutes. The deposition was carried out at $450\text{ }^\circ\text{C}$ and was allowed to cool to room temperature under nitrogen once again. At the end of the depositions, some undissolved copper precursor remained in the AACVD bubbler. A very dark green/blue film was deposition that covered the entire glass substrate. Powder XRD identified that ZnO was present (Fig. 5-4c).

The addition of surfactants and a donor functionalised alcohol produced films with better coverage but influenced the appearance of the film. With these additions, the films deposited were darker and less transparent. This will be a hindrance for their potential application. A different copper precursor was investigated. Even though $[\text{Cu}(\text{acac})_2]$ produced adherent films with good coverage, the solubility issues associated with this precursor cause a lot of waste.

The addition of CTAB and a donor functionalised alcohol also has an effect on the preferred orientation exhibited. The degree of preferred orientation using Bragg's crystal plane was determined using the calculation of the texture coefficient. The reflections analysed for the In_2O_3 films were 100, 002, 101, 102, 110 and 103. The texture coefficient was calculated using equation 4.1, explained in chapter 4. Table 5-2 shows the extent of preferred orientation for each peak seen on the XRD (Fig. 5-4). It is seen that the addition of CTAB with a high or low concentration grow in the [101] direction however the addition of the donor functionalised alcohol grow in the [002] direction. The (002) and (101) plane are commonly seen in ZnO thin films.

Table 5-2: Texture coefficient intensity ratio for XRD peaks obtained from films deposited from $\text{Zn}(\text{OAc})_2/\text{Cu}(\text{acac})_2$ with a) CTAB (low conc), b) CTAB (high conc) and c) $\text{HOCH}_2\text{CH}_2\text{OMe}$.

	100	002	101	102	110	103
a)	1.09	0.82	1.55	0.76	1.01	0.78
b)	1.26	0.60	1.28	0.87	1.05	0.94
c)	0.17	2.69	0.45	1.09	0.29	1.30

Copper acetate $[\text{Cu}(\text{OAc})_2 \cdot \text{H}_2\text{O}]$ was chosen since it is very soluble in methanol. AACVD of copper acetate mixed with zinc acetate in methanol was investigated at temperatures between 350 – 450 °C in separate experiments. The films formed had uniform coverage and were transparent with a mainly green colour. XRD was performed on each film that identified the presence of ZnO (Fig. 5-7).

5.3.1 Dual Source AACVD

In order to deposit thin films with better coverage and produce films that are more reproducible, dual source AACVD can be utilized.²⁰² This involves having the precursors separated in two AACVD bubblers. Each AACVD bubbler has its own humidifier and the aerosol droplets are carried to the AACVD reactor via nitrogen gas through a Y-junction to the CVD reactor. There is a potential to obtain films that have unique microstructure, better coverage, are free from pin-holes and are more reproducible due to more efficient mixing. The precursors are not in contact until they are in gaseous form at the Y-junction. At this point gas particles have the chance to interact and mix more effectively than when mixed as solids (Fig 5-5).

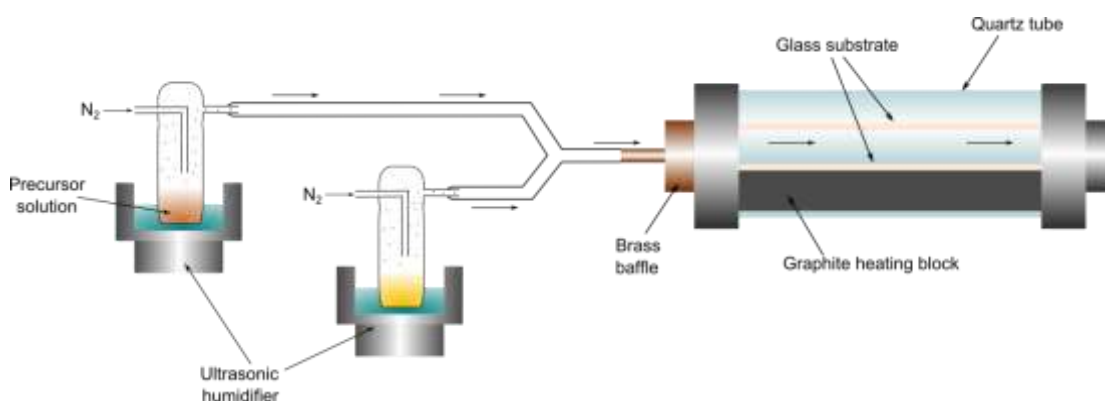


Figure 5-5: Diagram of dual source AACVD.

The zinc acetate and copper acetate reaction was repeated but used with a dual source AACVD set up. In one bubbler there was a mixture of Zn(OAc)₂/MeOH and in the other, a mixture of Cu(OAc)₂/MeOH (Fig. 5-6). The temperatures of the depositions were carried out at 350 and 450 °C. At the end of the deposition, the films were allowed to cool to room temperature. Both temperature conditions produced transparent films with mainly green colour. XRD measurements were performed on the thin films, which identified the presence of ZnO (Fig. 5-7).

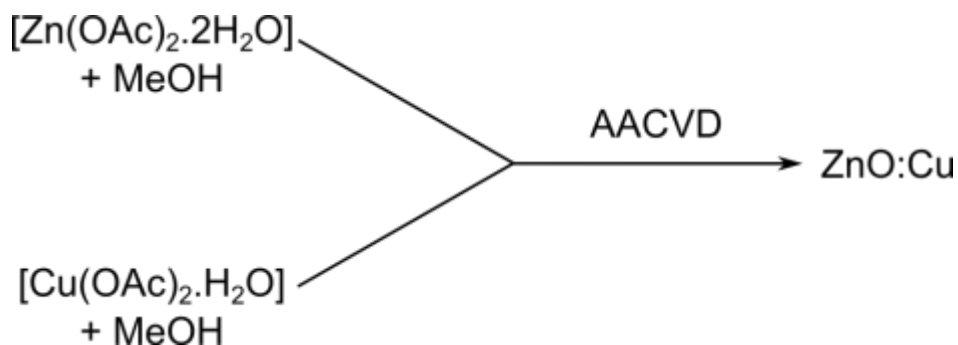


Figure 5-6: Schematic diagram of Dual Source AACVD used in this investigation.

Using both AACVD and dual source AACVD of Zn(OAc)_2 and Cu(OAc)_2 in MeOH, green thin films were produced which were identified as ZnO. It can be seen that temperature has an effect on the crystallinity of the resulting film. Each AACVD method had crystalline XRD patterns for thin films deposited at 450 °C. However, the dual source AACVD set up produced films that had a ‘cleaner’ coverage. The films produced were free from pin-holes and had a uniform colour. Increased uniformity of the films coverage, colour and reproducibility is an advantage for the potential use of these films. The dual source AACVD procedure was chosen to deposit these ZnO:Cu for further investigation.

To investigate how the copper concentration in the starting solution affects the deposited film, the copper concentration was varied from 1 to 8 mol%. Dual source AACVD was carried out using the same conditions previously described but the starting $\text{Cu(OAc)}_2/\text{MeOH}$ solution was varied 1, 2, 4 and 8 mol% concentration when compared to the $\text{Zn(OAc)}_2/\text{MeOH}$ solution. Temperature also has an impact on the properties of the films investigated. Therefore the depositions were studied between 350 – 450 °C. These ZnO:Cu films were also compared to pure ZnO thin films deposited from $\text{Zn(OAc)}_2/\text{MeOH}$ mixture at 350, 400 and 450 °C.

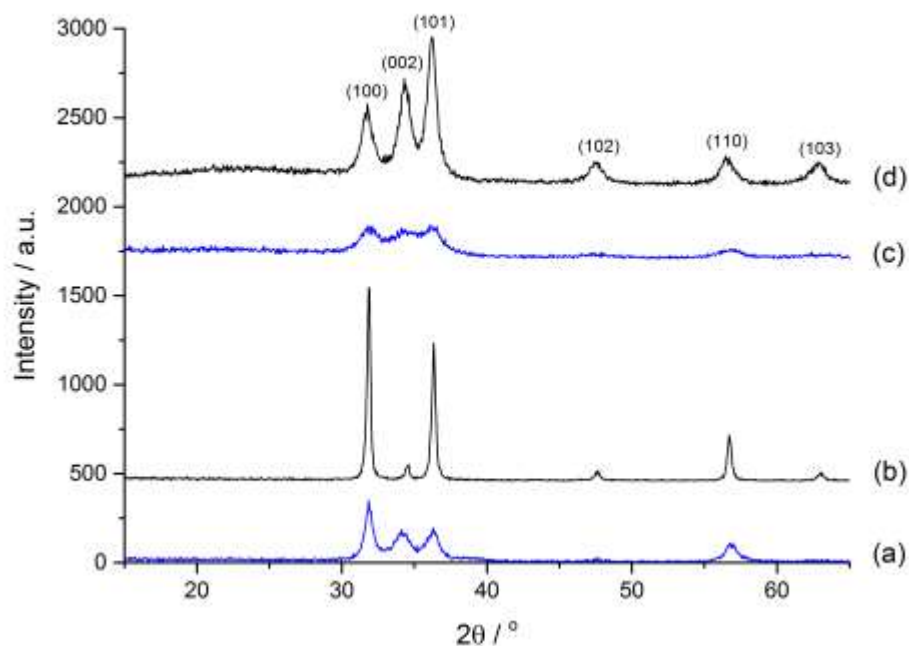


Figure 5-7: XRD patterns obtained from AACVD at a) 350 °C, b) 450 °C and Dual source AACVD at c) 350 °C and d) 450 °C.

The ZnO:Cu thin films deposited at 350 °C were all transparent and clear. The only film that had a green colour was when 8 mol% copper solution was used in the dual AACVD system. XRD patterns of these films were carried out, which identified the presence of ZnO for all the films. At this temperature, the crystallinity of the films were poor however, the highest concentration (Fig 5-8) appeared slightly more crystalline.

The degree of preferred orientation using Bragg's crystal plane was determined using the calculation of the texture coefficient. The reflections analysed for the ZnO films were 100, 002, 101, 102, 110 and 103. The texture coefficient was calculated using equation 4.1, explained in chapter 4. Table 5-3 show the extent of preferred orientation for each particular peak seen on the XRD. It is seen that ZnO film deposited at 350 °C are orientated in the [002] direction but the incorporation of copper changes the orientation to [101] direction which is seen in all the doped films.

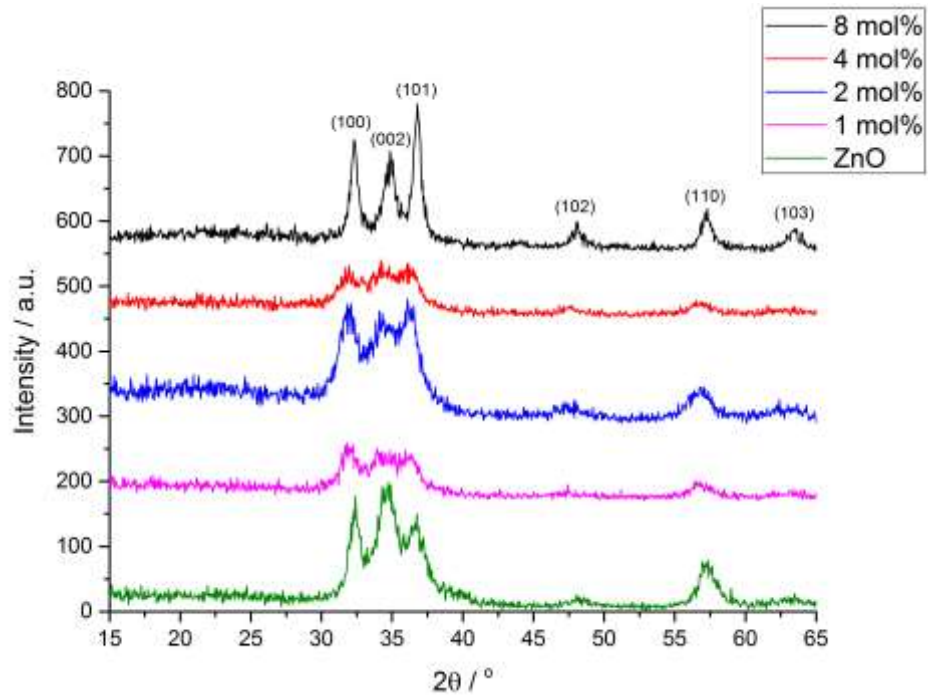


Figure 5-8: XRD patterns obtained from dual source AACVD depositions carried out at 350 °C for ZnO and 1 – 8 mol% ZnO:Cu.

Table 5-3: Texture coefficient intensity ratio for XRD peaks obtained from films deposited using dual source AACVD at 350 °C.

	100	002	101	102	110	103
ZnO	1.09	2.34	1.74	0.34	0.37	0.12
1 mol%	1.28	1.89	2.07	0.50	0.26	0.17
2 mol%	1.97	0.28	2.13	0.97	0.41	0.23
4 mol%	1.25	1.31	2.56	0.59	0.28	0.16
8 mol%	1.13	1.59	2.31	0.56	0.28	0.14

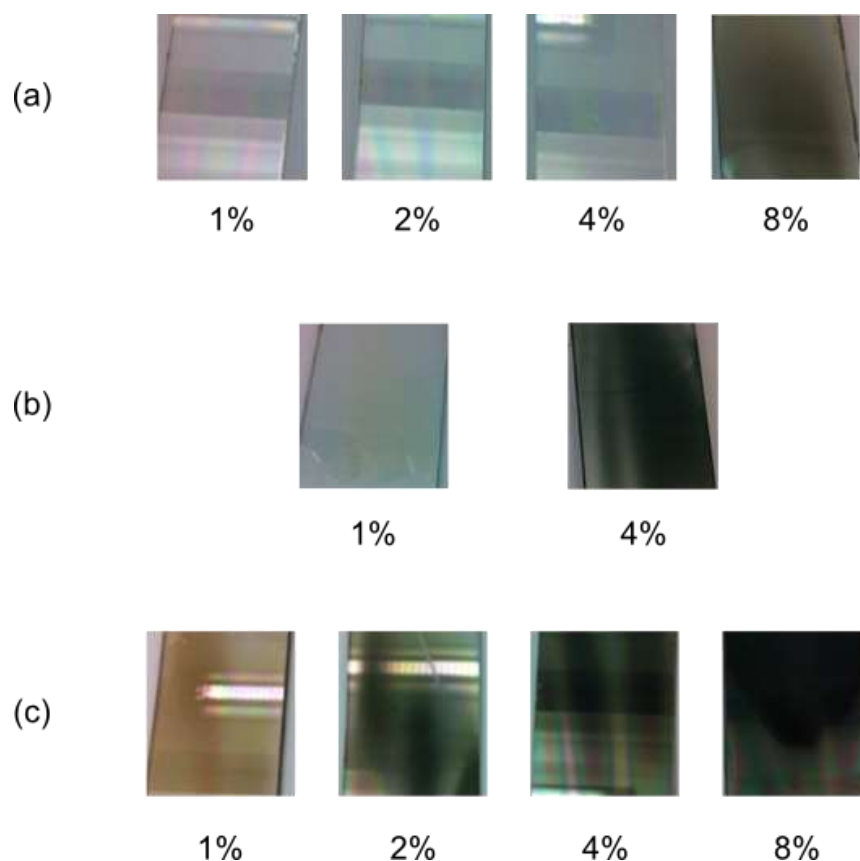


Figure 5-9: Photos of ZnO:Cu thin films deposited using dual source AACVD at a) 350 °C, b) 400 °C and c) 450 °C.

The dual source AACVD was repeated using the same conditions previously described using the $\text{Cu}(\text{OAc})_2/\text{MeOH}$ solution with 1 and 4 mol% concentration when compared to the $\text{Zn}(\text{OAc})_2/\text{MeOH}$ solution but were deposited at 400 °C. The lower copper concentration produced a clear transparent film whereas, 4 mol% produced an uneven green transparent film (Fig. 5-9b). XRD patterns of these films (Fig. 5-10) indicated the presence of ZnO only. The crystallinity of the pure ZnO increased when deposited at this higher temperature, however the copper doped ZnO were not as crystalline. The preferred orientation (Table 5-4) were calculated for these XRD patterns and the film deposited with 1 mol% Cu grow in the [002] direction and 4 mol% Cu films grow in the (101) plane.

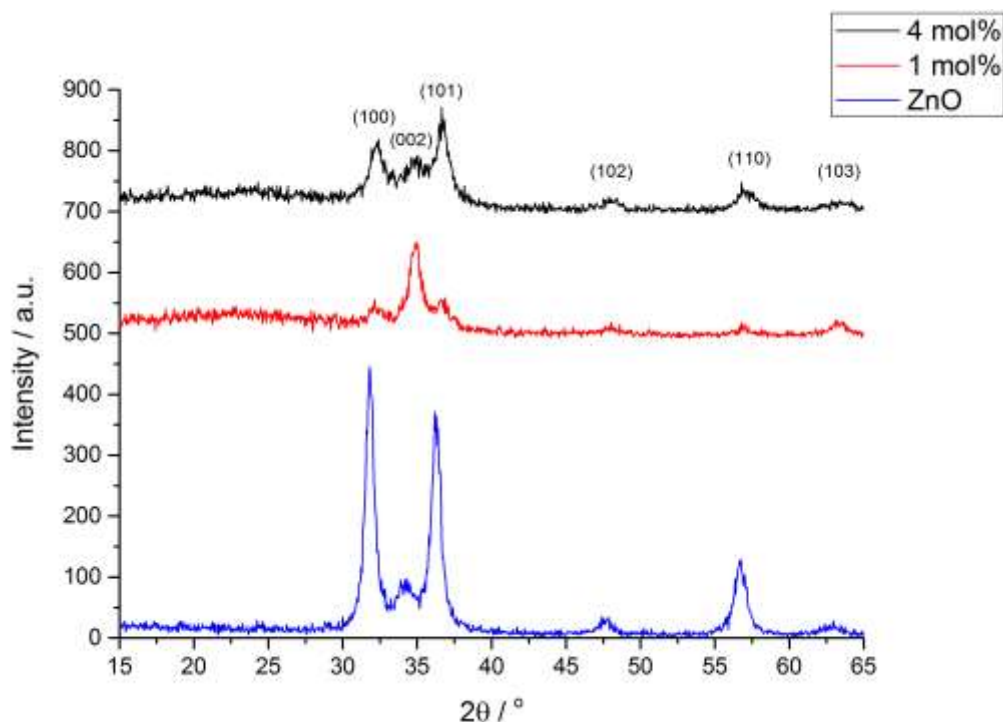


Figure 5-10: XRD patterns obtained from dual source AACVD depositions carried out at 400 °C for ZnO and 1 – 4 mol% ZnO:Cu.

Table 5-4: Texture coefficient intensity ratio for XRD peaks obtained from films deposited using dual source AACVD at 400 °C.

	100	002	101	102	110	103
ZnO	2.01	0.69	2.61	0.28	0.36	0.06
1 mol%	0.77	2.94	1.26	0.60	0.20	0.22
4 mol%	1.18	1.45	2.60	0.33	0.32	0.13

Once again the dual source AACVD was repeated using the same conditions previously described with Cu(OAc)₂/MeOH solution with 1, 2, 4 and 8 mol% concentration when compared to the Zn(OAc)₂/MeOH solution but were deposited at 450 °C. The films produced at this temperature are not as uniform in colour and not as transparent (Fig. 5-9c). At the lowest copper concentration, the films were brown and became a darker green as the copper concentration

increased. XRD patterns of these films were taken, which also only identified the presence of ZnO (Fig 5-11). The crystallinity of the films was greater when compared to the films deposited at a lower temperature. Preferred orientation were calculated for these XRD patterns (Table 5-5) and indicated that the pure ZnO and Cu doped films deposited at 450 °C have preferred orientation in the [101] directions. It has been reported that the preferred orientation of ZnO is commonly in the (002) or (101) plane. The difference has been attributed to the temperature, zinc precursors and depositions rates.^{219,227-230} In this investigation, it has been seen that doping zinc oxide with copper and temperature causes the (101) plane to be dominant for most of the films deposited, whereas ZnO deposited at the lower temperatures of 350 °C and 400 °C have preferred orientation in the (002) plane.

Table 5-5: *Texture coefficient intensity ratio for XRD peaks obtained from films deposited using dual source AACVD at 450 °C.*

	100	002	101	102	110	103
ZnO	1.75	0.78	2.82	0.23	0.35	0.06
1 mol%	0.63	1.79	2.57	0.58	0.20	0.21
2 mol%	0.88	1.80	2.45	0.49	0.21	0.17
4 mol%	0.85	1.88	2.27	0.62	0.19	0.19
8 mol%	1.36	1.29	2.54	0.39	0.27	0.15

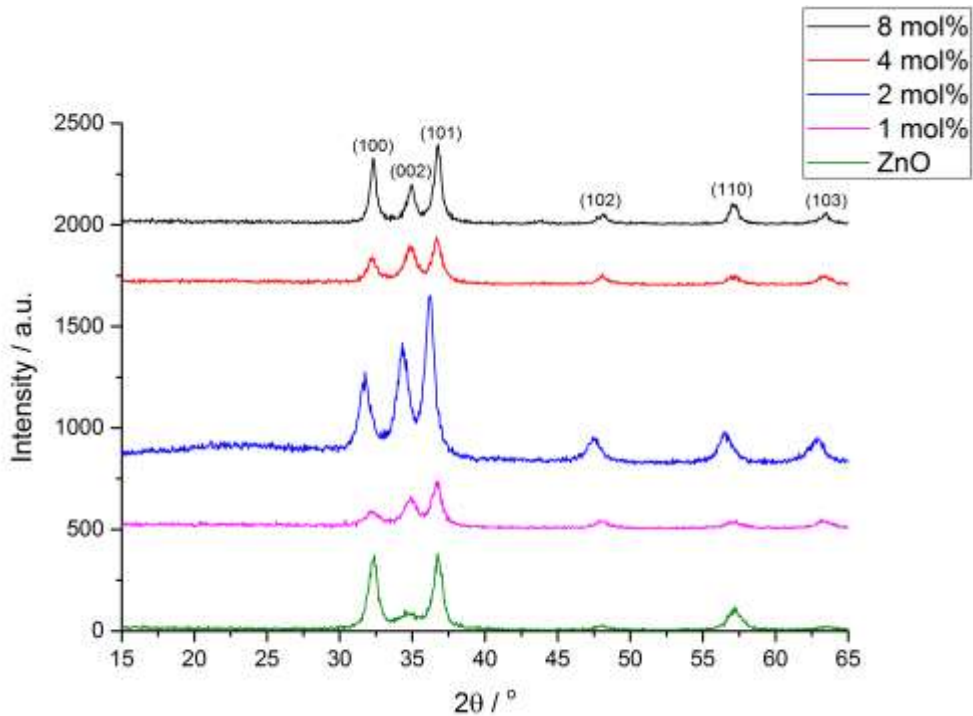


Figure 5-11: XRD patterns obtained from dual source AACVD depositions carried out at 450 °C for ZnO and 1 – 8 mol% ZnO:Cu.

It has been seen that the temperature has a big effect on the appearance of the films and the crystallinity of the XRD patterns obtained. All the films showed that the higher the copper concentration, the higher the potential for the films to have a green colour. The films with the most uniform appearance and transparency were films produced at 350 °C. Even though the crystallinity of the films were not as good as the films deposited at higher temperatures, it was still sufficient to identify the presence of ZnO. Therefore, the deposition temperature chosen for the rest of the depositions was 350 °C.

The dual source AACVD was repeated using the same conditions previously described however the $\text{Cu}(\text{OAc})_2/\text{MeOH}$ solution was varied between 10 - 18 mol% concentration when compared to the zinc starting solution and the deposition temperature was 350 °C. The increase in doping concentration was carried out to see how an increase in copper will affect the films.

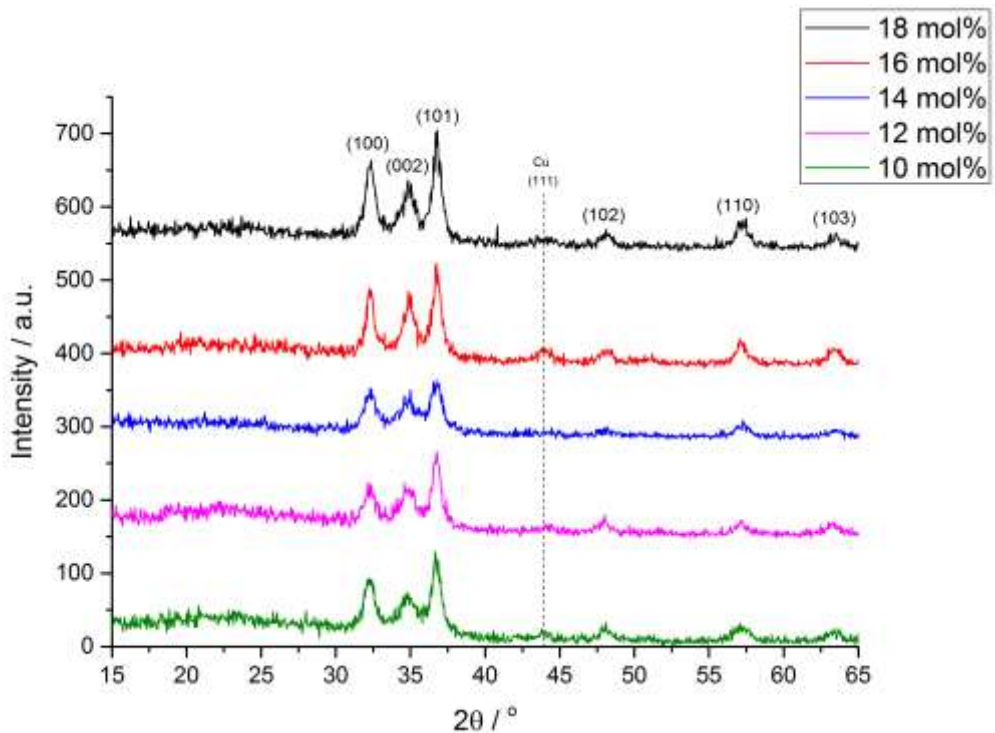


Figure 5-12: XRD patterns obtained from dual source AACVD depositions carried out at 350 °C for 10 – 18 mol% Cu films.

All the films produced at these higher doping concentrations were all green and got darker from 10 – 18%. XRD pattern of these films were taken and identified the presence of ZnO (Fig. 5-12). However, the higher doping concentrations of 16 and 18% had a very weak peak at $\sim 44^\circ$ which corresponds to a copper (111) plane. This could indicate that at higher % mol concentrations, a composite of ZnO and Cu may start to deposit. These XRD patterns were more crystalline than the pattern taken for the lower doping concentrations showing that the increase in copper concentration increases the thin film crystallinity.

5.3.2 Optical Properties

Transmission and reflectance measurements were taken for the ZnO and ZnO:Cu (1 – 18 mol%) thin films deposited with the dual source AACVD system at 350 °C. All the as-deposited films displayed minimal reflectivity (5 – 15%). However depending on the concentration of copper, the transmission varied. As the dopant concentration increased, there was a decrease in transmittance observed (Fig. 5-13a) which could be due to scattering of photons with crystals created by doping²²⁷ and the colour of the films changed from clear to green. Lower concentration of copper doped ZnO thin films have higher transmittance with sharp absorption edges.

The UV/Visible absorption spectrum of pure ZnO and Cu doped ZnO thin films were investigated at room temperature. As shown in Fig. 5-13b, the optical absorption spectra change after Cu doping increase above 8 mol%. The optical absorption observed from these materials can be a result of an exciton peak at energy corresponding to their band gap.^{231,232}

5.3.3 Band Gap

The optical band gap values were calculated from Tauc plots and found to decrease from 3.2 to 2.9 eV (Table 5-2) with increased Cu concentration. This could be due to the higher electronegativity of the Cu-dopant to Zn host, 1.9 and 1.65 respectively.

It has been reported that the incorporation of copper (x – 10%) can lower the band gap of ZnO by ~ 0.21 eV. Studies have shown that O 2p and Cu 3d bands are closely matched in energy. The band gap reduction with increase in Cu doping concentration is consistent with results coming from the first-principles calculation based on density functional theory.^{233,234}

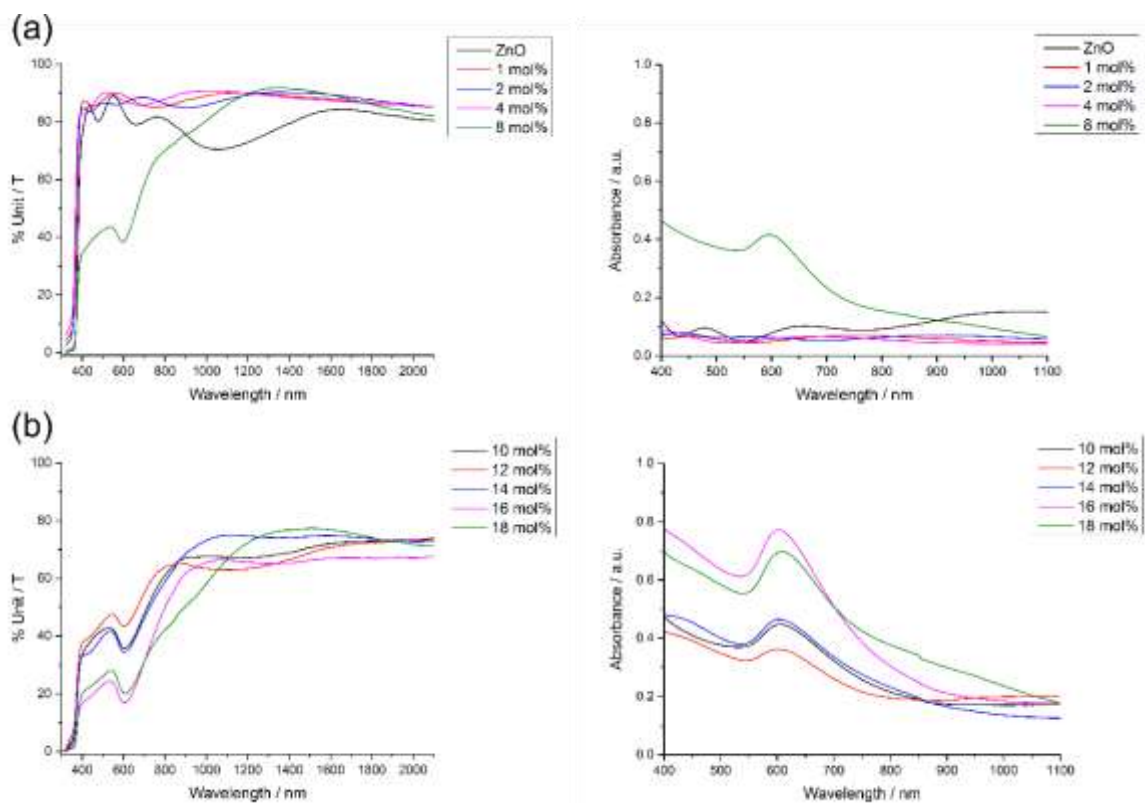


Figure 5-13: a) Optical transmission spectrum taken against an air background showing ZnO and 1 – 18 mol% ZnO:Cu thin films, b) UV/Visible absorbance spectrum for ZnO and 1 - 18 mol% ZnO:Cu films.

Table 5-6: Band gap measurements calculated using a Tauc plot.

Cu mol%	Band Gap / eV
1	3.32
2	3.31
4	3.34
8	3.09
10	3.10
12	3.06
14	3.02
16	2.86
18	2.87

Overall the techniques have indicated that the films produced have adopted a wurtzite ZnO structure with varying amounts of Cu incorporated into the films. As the copper percentage increases, the appearance of the films became darker, intense green colour and less transparent. XRD patterns have shown that at the highest % mol Cu concentration, a Cu peak was starting to develop suggesting that a composite may have been produced. The aim of depositing ZnO:Cu films is to test their antimicrobial effectiveness. Therefore the ZnO:Cu films most appropriate for testing are between 1 – 10 mol% ZnO:Cu. As a result, these films will be further analysed.

5.3.4 Scanning Electron Microscopy (SEM)

SEM images were taken in secondary electron mode at 5kV and the samples were coated with gold before images were taken to avoid charging, as these samples are non-conducting. The microstructure of the films with pure ZnO, and films with starting copper concentrations of 1 - 10 mol% (Fig. 5-14) was found to vary.

The pure ZnO films deposited using $\text{Zn}(\text{OAc})_2/\text{MeOH}$ produced a microstructure composed for particles of different sizes. This size ranged from 100 – 600 nm. This morphology changed when copper was incorporated into the film. For the films using 1% copper concentration of $\text{Cu}(\text{OAc})_2/\text{MeOH}$ produced films made of uniform smaller particles at a range between 50 – 100 nm. As the copper concentration increases, the size of the particles increase and the size of the particles become more uniform.

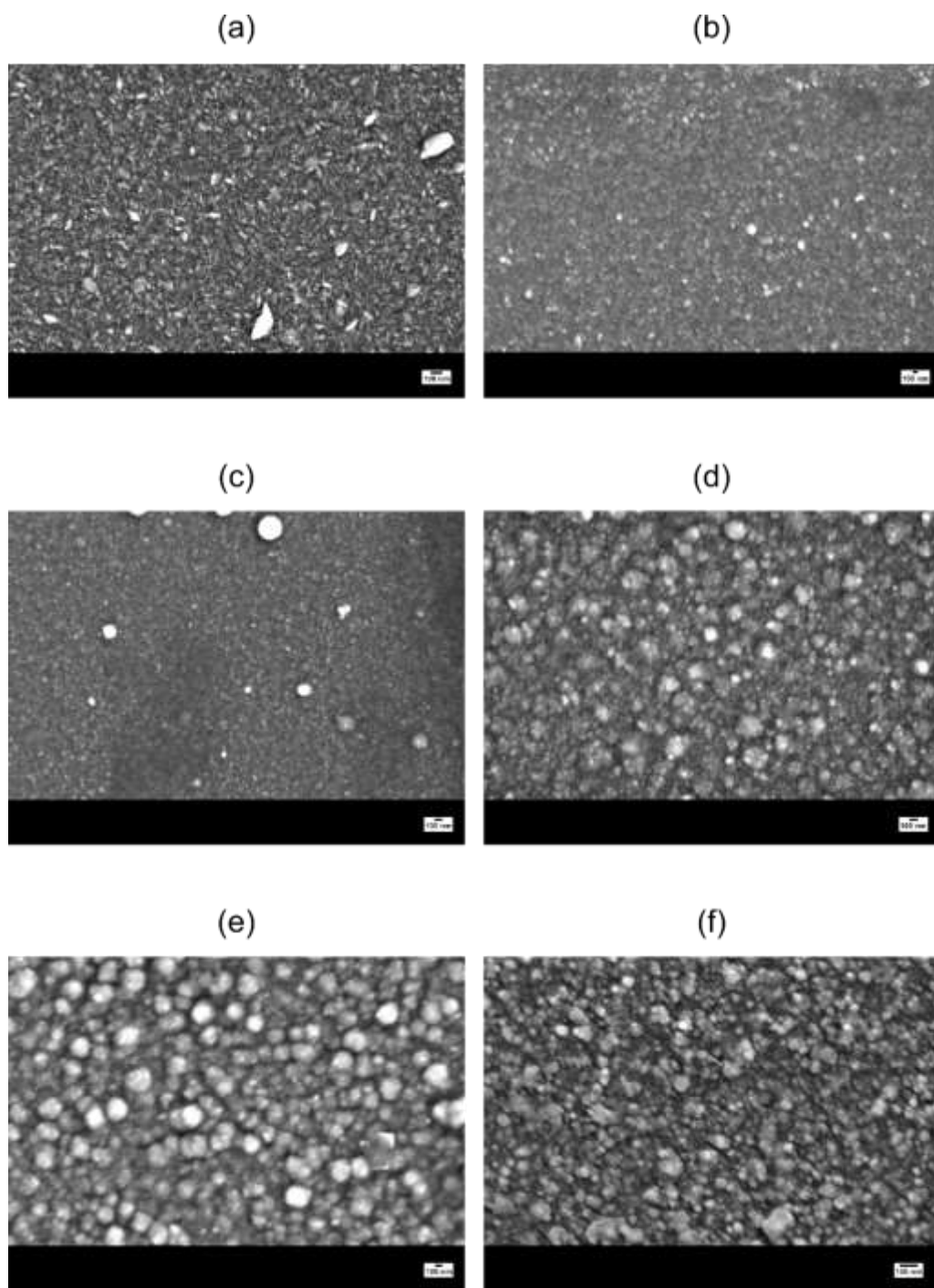


Figure 5-14: SEM images of a) ZnO and ZnO:Cu films b) 1 mol% Cu, c) 2 mol% Cu, d) 4 mol% Cu, e) 8 mol% Cu and f) 10 mol% Cu.

5.3.5 EDX Measurements

EDX analysis was utilised to obtain composition of the films and carried out to determine the stoichiometry of the ZnO:Cu thin films grown with the various copper concentrations. The measurements of the films with starting copper concentrations of 2, 4 and 8 mol% were studied since these were the best films deposited.

Table 5-7: EDX measurements taken from the ZnO:Cu thin films.

ZnO:Cu	Zn/Atomic %			Average	Cu/Atomic %			Average
2 mol%	30.9	25.3	26.1	27.5	0.2	0.2	0.5	0.3
4 mol%	32.8	30.3	26.5	29.9	0.8	1.1	1.1	1.0
8 mol%	28.8	32.1	25.9	28.9	1.0	1.3	1.4	1.2

The EDX measurements have shown that the ratio of Zn to Cu at the start of the AACVD deposition was different to the amount of copper detected in the films. The films with 2 mol% copper concentration from the starting material produced films with an average of 0.3 at% Cu in the film whereas, 4 mol% copper concentration deposited films with 1.0 at% Cu. For the thin films deposited with 8 mol% Cu for the starting solution produced films with 1.2 at% Cu. As the copper precursor concentration increases, more copper is incorporated into the film.

5.3.6 X-ray photoelectron spectroscopy

XPS was carried out on the three ZnO:Cu films to determine the oxide species on the surface of the film. Only the 2, 4 and 8 mol% films were analysed since they were the best films and the most transparent. The peaks observed after analysis of the surface of the film were modelled and the binding energy values compared to literature values to identify the compounds of the film.

The presence and oxidation state of copper were investigated for the ZnO:Cu (2, 4 and 8 mol%). The binding energy of Cu 2p_{3/2} were 932.5, 932.2 and 933.0 eV for 2, 4 and 8 mol% ZnO:Cu respectively. The binding energies correspond to Cu²⁺ and Cu¹⁺ but there were no satellite peaks observed, which are characteristic of Cu²⁺. The binding energies of Cu 2p_{1/2} were at 952.2, 952.1 and 952.8 eV for 2, 4 and 8 mol% ZnO:Cu respectively. This suggests that the copper species present at the surface of the films are Cu¹⁺.¹⁹⁶

The characteristic peaks for the Zn 2p_{3/2} and 2p_{1/2} states appeared at 1021.3 and 1044.4 eV for 2 mol% ZnO:Cu respectively. This was similar to the values for 4 mol% ZnO:Cu that were 1021.5 and 1044.6 eV. The 8 mol% ZnO:Cu also had value for Zn 2p_{3/2} and 2p_{1/2} states were 1021.3 and 1044.3 eV respectively. These values correspond to Zn²⁺ found in ZnO. This confirms the presence of ZnO on the surface of all the films.^{202,227}

Zn and Cu have been identified on the surface of all the ZnO:Cu analysed. It has been identified as ZnO and Cu₂O. Quantification using peak areas determined by the Shirley method and empirical sensitivity factors gave a copper to zinc ratio of 1:111 for the 2 mol% Cu, 1:114 for the 4 mol% Cu and 1:129 for the 8 mol% Cu at the surface. This differs from the ratio obtained from EDX measurements that were 1:53, 1:24 and 1:23 for 2, 4 and 8 mol% Cu respectively. This difference can be related to XPS being a surface sensitive technique whereas, EDX can penetrate into the bulk of the material. This indicates that there may be more copper present in the bulk of the films rather than the surface and it is also seen that the % mol Cu increases, there is less Cu on the surface and more in the bulk.

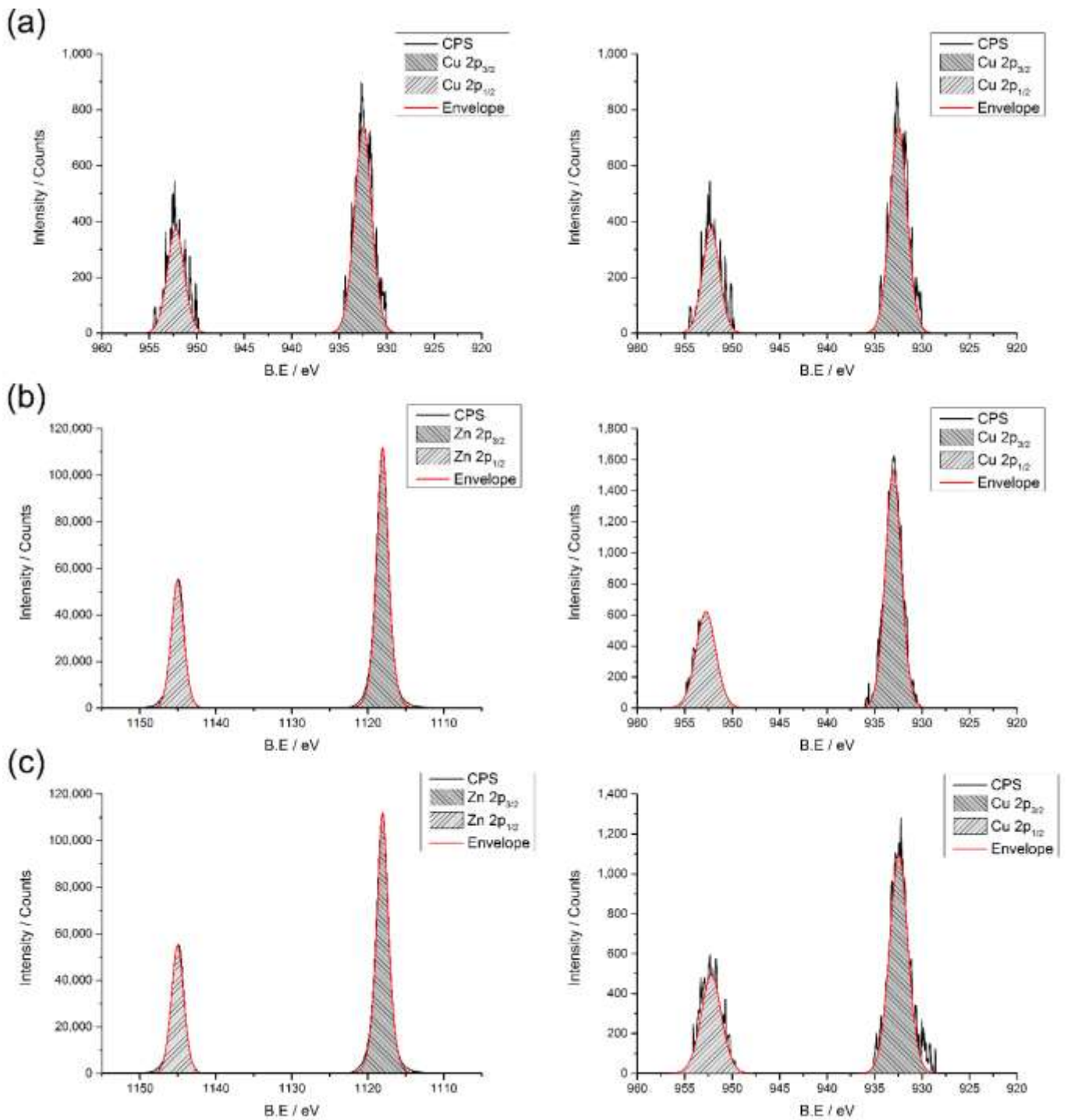


Figure 5-15: XPS for ZnO:Cu thin films of Zn 2p and Cu 2p for a) 2 mol%, b) 4 mol% and c) 8 mol%.

5.3.8 Raman Analysis

Raman spectroscopy was used to further characterise the resulting films and characteristic Raman peaks were observed for all films with the strongest band appearing $\sim 440 \text{ cm}^{-1}$ with a weaker band at $\sim 570 \text{ cm}^{-1}$. These two weak peaks correspond to characteristic wurtzite E_2 (high) mode and A_1 longitudinal optical (LO) mode for ZnO.²³⁵

5.3.7 X-ray absorption spectroscopy

X-ray absorption near edge structure (XANES) were performed on the ZnO thin films. Cu k-edge XANES data for the samples are shown in Fig. 5-16 along with the corresponding data for metal powders: Cu, Cu₂O and CuO. The energy scales of all the spectra have been consistently normalised. The local environment of the Cu can have an effect on the shape of the XANES spectra making it easier to identify the local environment of the Cu present in the ZnO:Cu films. In this case, the XANES spectra for the 8 mol% ZnO:Cu films match that of Cu and Cu₂O standards indicating that both are present in the film. This is comparable to the XPS data indicating the presence of Cu¹⁺ on the surface of 8 mol% Cu film.

The XANES spectra for 2 and 4 mol% ZnO:Cu films data is noisy and roughly match that of CuO standard indicating that copper is present in the film in the form of Cu²⁺. This does not match with the XPS data analysed indicating that there is a need to redo these XANES experiments to be able to fully characterise the local environment of the copper incorporated into the ZnO.

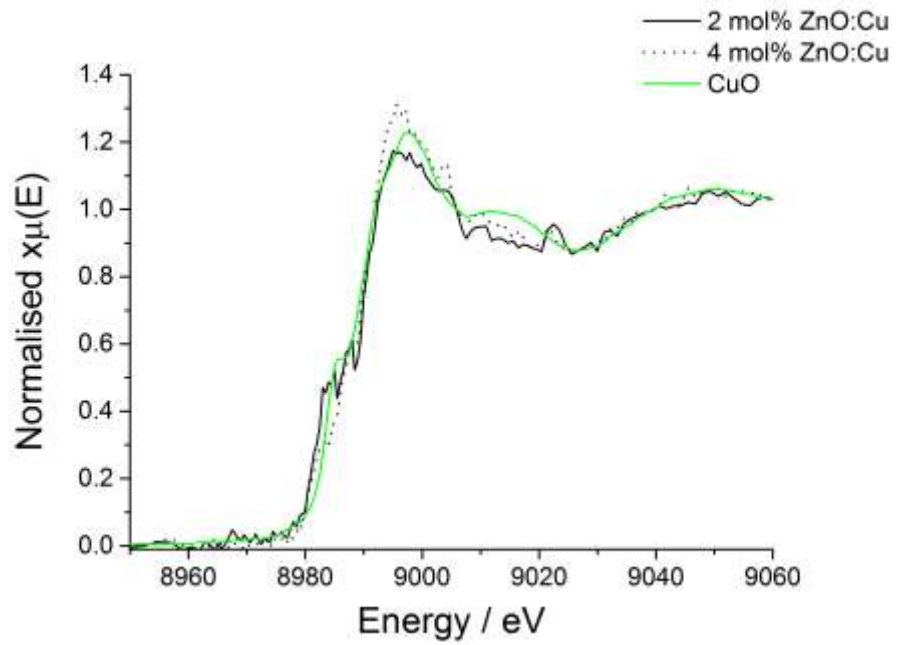
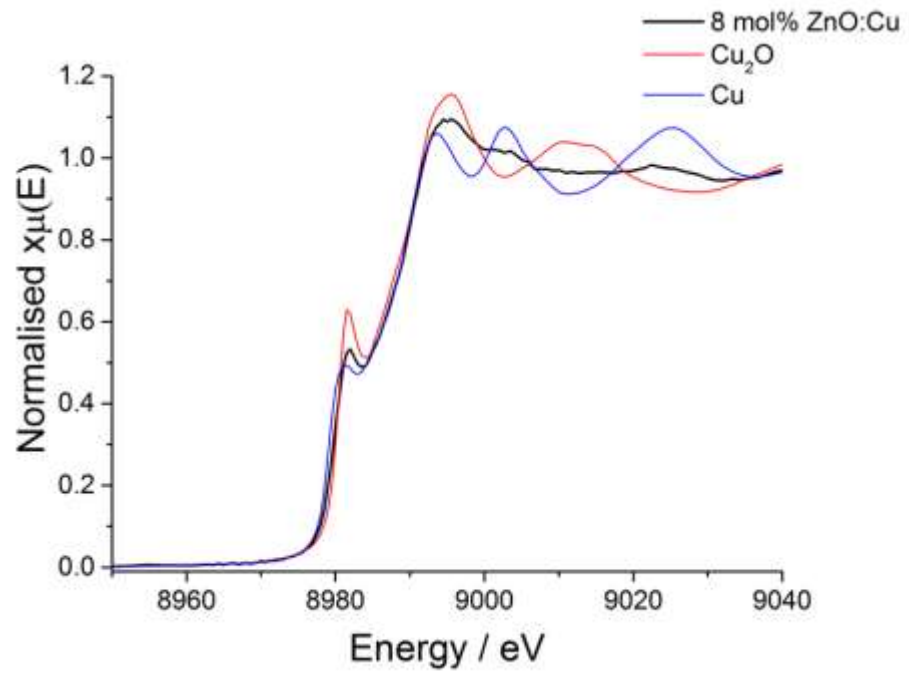


Figure 5-16: Normalised copper K-edge XANES spectra for Cu, Cu₂O, CuO and the ZnO:Cu thin film sample.

5.4 Antimicrobial Activity of ZnO and ZnO:Cu

The antimicrobial activity of a series of copper doped zinc oxide thin films deposited onto microscope slides were determined using a gram-negative organisms that is commonly found in hospital environments, *E. coli*. Samples were cut into 1 x 1 cm sections and were covered with 25 μL of bacterial suspension containing approximately 10^5 cfu. For each experiment, a set of samples were illuminated with a white light source (28 W), emitting an average light intensity of 3750 lux at a distance of 30 cm from the sample. In all experiments, a control sample set was maintained in parallel and were stored under dark conditions for the same exposure times. This fluorescent lamp emits light across the visible region of the spectrum similar to those commonly found in UK hospitals. The white light intensity used in this is more intense (3x times larger) than what is found in A&E wards. However, the microbial loads used in these experiments are greater than those found on touch surfaces in healthcare institutions. Serial dilution and viable colony counts on agar with subsequent overnight incubation at 37 °C was performed. The resultant viable counts of bacteria for each sample section was determined. The results for ZnO and ZnO:Cu films are shown in Fig. 5-17, demonstrate that the films have antimicrobial activity against *E. coli* with glass controls. Each point represents the \log_{10} of the mean number of viable bacteria from three samples and error bars represent the calculated standard error.

The light-activated and bactericidal activities of pure ZnO and doping ratio (to copper) of ZnO:Cu were tested. A range of samples were tested to deduce whether ZnO had antimicrobial activity and how the incorporation of copper affected the efficacy. At 3 hour exposure time (Fig 5-17a), all the films had an increase in activity in the light (L+) rather than the dark (L-) except for the 8% ZnO:Cu which had the same bacterial reduction rate for both conditions ($1.3 \log_{10}$, $P < 0.01$). After 6 hours, the 2 and 4% ZnO:Cu had a bacterial reduction of $4 \log_{10}$ only when illuminated with white light. This is the same reduction observed for 8 mol% ZnO in light and dark (Fig. 5-17b). The exposure time was extended to 18 hours, all the

ZnO:Cu had a 4- \log_{10} ($P < 0.001$) reduction as well as the pure ZnO but only when illuminated.

The antimicrobial activity of the copper doped ZnO thin films were significantly better than the pure ZnO. Pure ZnO did possess a reduction rate that was significant but only when illuminated with white light. The most effective antimicrobial surface was the green 8 mol% ZnO:Cu thin film that showed high effectiveness in the light as well as in the dark. This can be due to the increase in copper doped into the thin films. The increase in activity of the ZnO films in the light corresponds with the studies showing the increase in the production of ROS when illuminated. The increase in ROS can cause the increase in microbial death. With the incorporation of copper, the ZnO:Cu have a number of mechanisms that can cause the death of the bacteria cells.^{209,218}

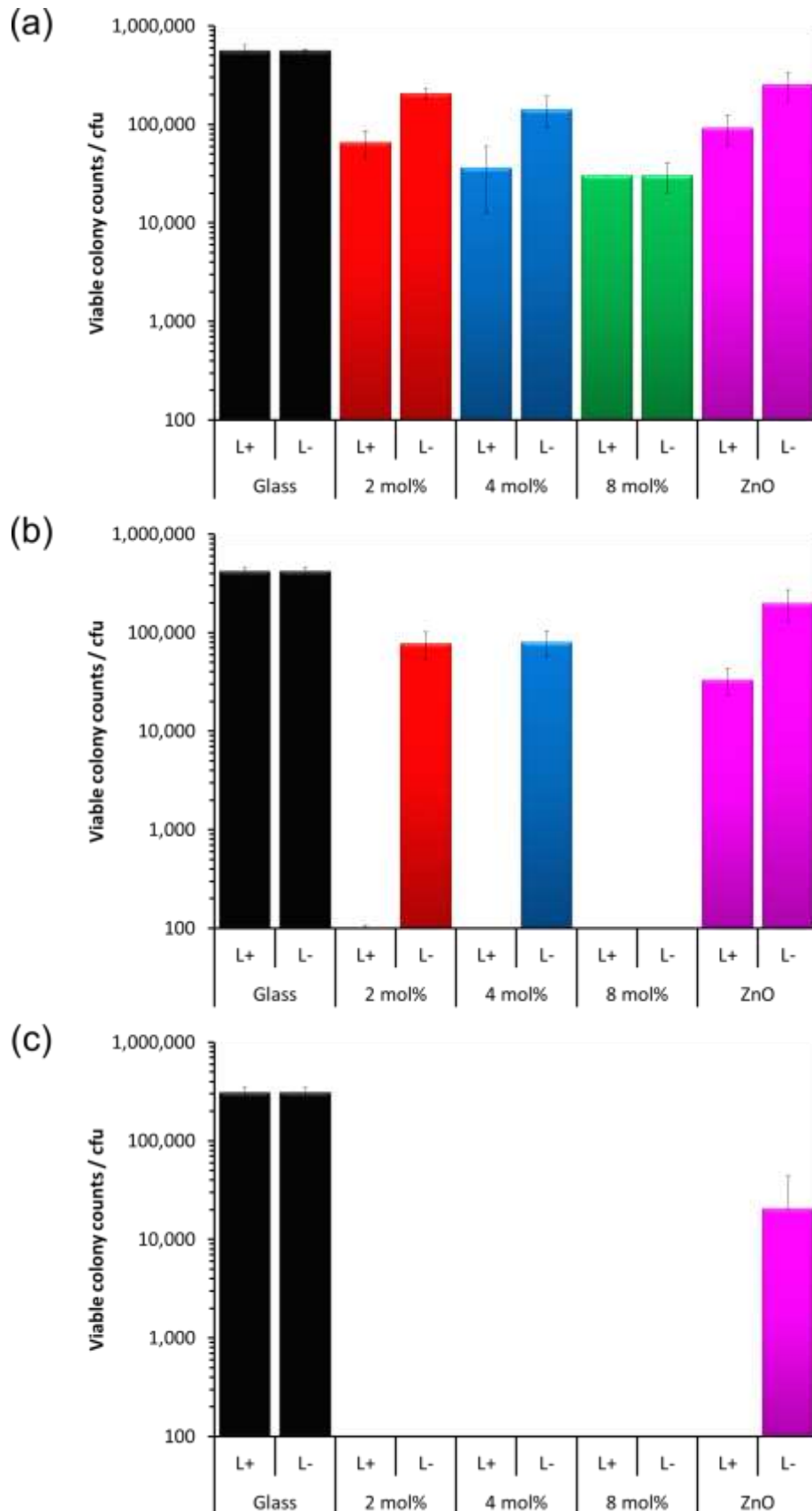


Figure 5-17: Viable counts of bacteria after incubation on ZnO, ZnO:Cu thin films and glass control tested against *E. coli* for a) 3 hours, b) 6 hours and c) 18 hours. (L+ = illuminated and L- = not illuminated (in the dark)).

5.5 Conclusion

This investigation showed $[\text{Zn}(\text{OAc})_2 \cdot 2\text{H}_2\text{O}]$ and $[\text{Cu}(\text{NO}_3)_2 \cdot 3\text{H}_2\text{O}]$ as the precursors that produced adhesive, reproducible thin films with complete coverage. Dual source AACVD uses two separate AACVD bubblers with their own humidifier. The aerosol droplets join at the Y-junction for more effective mixing. The molar concentration, deposition temperature were varied and saw that the appearance, crystallinity and preferred orientation changed.

The antimicrobial effectiveness of ZnO and ZnO:Cu (2, 4 and 8 mol%) thin films deposited via AACVD was investigated. Microbiological analysis saw that ZnO possess antibacterial properties and are increased in the presence of white light. The bactericidal activity of the films significantly increased with the incorporation of copper. As the copper atomic percentage increased (0.31, 0.99 and 1.23 at% Cu), the microbial reduction increased. It was also seen that illumination of the films increased the antimicrobial effectiveness of the ZnO:Cu apart from the 8 mol% films, which had the same microbial reduction in the light and dark.

6

Conclusion and Future Work

The abundance and prevalence of nosocomial infections caused by MDR bacteria has emphasized the need for new strategies to combat the spread of infections. One approach is the utilisation of antibacterial surfaces. This thesis describes the development of potential antimicrobial coatings deposited via AACVD.

6. Conclusion

Hospital acquired infections (HAI) remain a significant problem in healthcare institutions where touch surfaces are known to harbour bacteria. These microbes can be transmitted from the hospital environments to patients and healthcare workers via the most common vehicle of transmission, unwashed hands. If the bacterial load on these touch surfaces can be reduced, the acquisition and onwards transmission of nosocomial infections can also be decreased. The use of self-cleaning coatings applied to touch surfaces, along with strict hospital hygiene measures can potentially reduce infection rates.

The coatings investigated in this thesis are 1) copper, 2) copper(I) oxide, 3) gallium oxide, 4) copper gallium oxide, 5) zinc oxide and 6) copper doped zinc oxide. To produce these films, a technique known as aerosol assisted chemical vapour deposition (AACVD) was used. This technique involves the formation of an aerosol through the dissolution of a precursor in a solvent. AACVD depends on solubility rather than the volatility of the precursors. AACVD is a useful method for depositing antimicrobial coatings because it is an industrially scalable process. A major advantage for AACVD is the ability to deposit on a wide range of substrates including the commonly used materials on touch surfaces in hospitals such as stainless steel. A wide range of analytical techniques were performed on the thin films that included powder XRD, SEM, XPS, and XAS.

In order to test the bactericidal properties of these coatings, they were tested against *E. coli* and *S. aureus* that are bacteria which commonly cause HAIs. A standard technique in microbiology was performed known as serial dilution and viable colony counting on to agar medium. All testing was duplicated and Mann Whitney analysis was performed to determine the statistical significance of the data. The results obtained from the different antimicrobial thin films tested are summarised in Table 6-1.

Table 6-1: Antimicrobial activity results of thin films deposited discussed in this thesis.

Thin Film	AACVD deposition conditions	Species	Bacterial reduction (log ₁₀)		Time
Cu	Cu(NO ₃) ₂ .3H ₂ O/MeOH cool in N ₂	<i>E. coli</i>	4		30 min
		<i>S. aureus</i>	4		60 min
Cu₂O	Cu(NO ₃) ₂ .3H ₂ O/MeOH cool in air	<i>E. coli</i>	2.7		60 min
		<i>S. aureus</i>	4.7		60 min
Ga₂O₃	GaMe ₃ /MeOH	<i>E. coli</i>	0.9		24 h
		<i>S. aureus</i>	1.2		24 h
Ga₂O₃- Cu₂O	GaMe ₃ / Cu(NO ₃) ₂ .3H ₂ O/MeOH	<i>E. coli</i>	4		24 h
		<i>S. aureus</i>	4		24 h
ZnO	Zn(OAc) ₂ .2H ₂ O/MeOH	<i>E. coli</i>	L+	4	18 h
			L-	1.4	18 h
2 mol% ZnO:Cu	Dual AACVD 1. Zn(OAc) ₂ .2H ₂ O/MeOH 2. Cu(OAc) ₂ .H ₂ O/MeOH	<i>E. coli</i>	L+	4	6 h
			L-	4	18 h
4 mol% ZnO:Cu		<i>E. coli</i>	L+	4	6 h
			L-	4	18 h
8 mol% ZnO:Cu		<i>E. coli</i>	L+	4	6 h
			L-	4	6 h

The copper and copper(I) oxide thin films exhibited highly significant microbial reduction in a short time period. When compared to other thin films discussed in this thesis, these Cu and Cu₂O films were the most effective, the closest coatings to these are ZnO:Cu film illuminated in white light at 6 hours. The inclusion of the copper increased the antibacterial efficacy by 12 hours. This increase was also observed with the Ga₂O₃-Cu₂O films. Pure ZnO (not illuminated, L-) was a more effective antimicrobial material when compared to Ga₂O₃. There is more potential in the ZnO thin films due to the transparency and the observed increase in activity in the light. Whereas, Ga₂O₃ gain significant microbial reduction with the incorporation of copper.

From this thesis investigation, it is obvious that copper is a candidate that should be further explored for antimicrobial materials. The incorporation of this natural antibacterial agent into metal oxide thin films can potentially produce highly effective coating as well as maintaining transparency. Films can be used for a wide range of applications and be coated on different types of substrates using AACVD.

6.1 Future Work

In the future to further this work quantification and an analysis of ions produced in solution and possible formation of radicals via techniques such as ICP-ES and EPR would be helpful. Other studies have carried out similar testing on films but were not attempted for this thesis. It would be of interest to analyse the mechanism of kill on microbes from these thin films.

Some differences in bacterial reduction rate were observed between gram positive and gram negative strains. Increasing the number of bacteria types could help identify a pattern due to the difference in microbial cell walls.

Silver is another natural antimicrobial metal and could be deposited along with silver oxide to see how the antimicrobial activity compares to the copper films investigated in this thesis. Doping silver into metal oxide such as ZnO could be used to further investigate the potential of ZnO.

References

- 1 L. Nicolle, G. Ducloux and J. Fabry, *World Heal. Organ.*, 2002, 1–64.
- 2 J. S. Garner, W. R. Jarvis, T. G. Emori, T. C. Horan and J. M. Hughes, *Am. J. Infect. Control*, 1988, **16**, 128–140.
- 3 H. P. Agency, *Network*, 2009, 2008–2009.
- 4 D. Reed and S. A. Kemmerly, *Ochsner J.*, 2009, **9**, 27–31.
- 5 R. D. Scott, *The direct medical costs of healthcare-associated infections in U.S. hospitals and the benefits of prevention*, 2009.
- 6 E. Tikhomirov, *Chemioterapia*, 1987, **6**, 148–151.
- 7 R. T. Mayon-White, G. Ducloux, T. Kereselidze and E. Tikhomirov, *J. Hosp. Infect.*, 1988, **11**, 43–48.
- 8 R. P. Gaynes, D. H. Culver, T. C. Horan, J. R. Edwards, C. Richards and J. S. Tolson, *Clin. Infect. Dis.*, 2001, **33**, 69–77.
- 9 S. Noimark, C. W. Dunnill, M. Wilson and I. P. Parkin, *Chem. Soc. Rev.*, 2009, **38**, 3435–3448.
- 10 L. Nazarko, *Br. J. Nurs.*, 2009, **18**, 597–598.
- 11 B. W. Trautner, *Curr. Opin. Infect. Dis.*, 2010, **23**, 76–82.
- 12 S. Mölstad, *Scand. J. Prim. Health Care*, 2003, **21**, 196–198.
- 13 S. C. Ranganathan and S. Sonnappa, *Pediatr. Clin. North Am.*, 2009, **56**, 135–156.
- 14 D. J. Diekema, S. E. Beekmann, K. C. Chapin, K. A. Morel, E. Munson and G. V. Doern, *J. Clin. Microbiol.*, 2003, **41**, 3655–3660.
- 15 A. W. Karchmer, *Clin. Infect. Dis.*, 2000, **31**, 139–143.
- 16 H. Wisplinghoff, T. Bischoff, S. M. Tallent, H. Seifert, R. P. Wenzel and M. B. Edmond, *Clin. Infect. Dis.*, 2004, **39**, 309–317.
- 17 P. Zanger, D. Nurjadi, B. Vath and P. G. Kremsner, *Infect. Immun.*, 2011, **79**, 2658–2662.
- 18 J. Nouwen, H. Boelens, A. Van Belkum and H. Verbrugh, *Infect. Immun.*, 2004, **72**, 6685–6688.
- 19 G. R. Corey, *Clin. Infect. Dis.*, 2009, **48**, 4, 254–259.
- 20 S. Wu, C. Piscitelli, H. de Lencastre and A. Tomasz, *Microb. Drug Resist.*, 1996, **2**, 435–441.
- 21 B. G. Spratt, *Science*, 1994, **264**, 388–393.
- 22 K. Poole, *Cell. Mol. Life Sci.*, 2004, **61**, 2200–2223.
- 23 J. Rodríguez-Baño, E. Picón, P. Gijón, J. R. Hernández, J. M. Cisneros, C. Peña, M. Almela, B. Almirante, F. Grill, J. Colomina, S. Molinos, A. Oliver, C.

- Fernández-Mazarrasa, G. Navarro, A. Coloma, L. López-Cerero and A. Pascual, *J. Clin. Microbiol.*, 2010, **48**, 1726–1731.
- 24 B. K. Chandra, G. Singh, N. Taneja, S. Pahil, S. Singhi and M. Sharma, *J. Med. Microbiol.*, 2012, **61**, 830–836.
- 25 G. J. M. Hersbach, *Antonie Van Leeuwenhoek*, 1983, **49**, 93–94.
- 26 N. Kardos and A. L. Demain, *Appl. Microbiol. Biotechnol.*, 2011, **92**, 677–687.
- 27 H. B. Woodruff, *Appl. Environ. Microbiol.*, 2014, **80**, 2–8.
- 28 A. Fleming, *Nobelprize.org*, 1945,
http://www.nobelprize.org/nobel_prizes/medicine/la.
- 29 E. C. Bragginton and L. J. V Piddock, *Lancet Infect. Dis.*, 2014, **14**, 857–868.
- 30 J. Davies, *Canadian Journal of Infectious Diseases and Medical Microbiology*, 2006, **17**, 287–290.
- 31 J. Clardy, M. A. Fischbach and C. R. Currie, *Curr. Biol.*, 2009, **19**, R437–R441.
- 32 I. M. Gould, *J. Antimicrob. Chemother.*, 2008, **62**, 3–6.
- 33 M. G. Head, J. R. Fitchett, M. K. Cooke, F. B. Wurie, A. C. Hayward and R. Atun, *Lancet Infect. Dis.*, 2013, **13**, 55–64.
- 34 J. Davies and D. Davies, *Microbiol. Mol. Biol. Rev.*, 2010, **74**, 417–433.
- 35 B. Henriques Normark and S. Normark, *J. Intern. Med.*, 2002, 252, 91–106.
- 36 J. O’Neill, *amr-review.org*, 2014.
- 37 World Health Organization, *WHO Publ.*, 2014, 1–119.
- 38 E. Shorter, *Med. Hist.*, 1984, **28**, 334.
- 39 I. M. Gould, *Lancet Infect. Dis.*, 2010, 10, 275–278.
- 40 M. Best and D. Neuhauser, *Qual. Saf. Health Care*, 2004, **13**, 233–234.
- 41 C. H. Tigre, I. Semmelweis and K. C. Carter, *J. Public Health Policy*, 1987, **8**, 582–584.
- 42 S. P. Stone, C. Fuller, J. Savage, B. Cookson, A. Hayward, B. Cooper, G. Duckworth, S. Michie, M. Murray, A. Jeanes, J. Roberts, L. Teare and A. Charlett, *BMJ*, 2012, **344**, 3005–3005.
- 43 D. Pittet, S. S. Panesar, K. Wilson, Y. Longtin, T. Morris, V. Allan, J. Storr, K. Cleary and L. Donaldson, *J. Hosp. Infect.*, 2011, **77**, 299–303.
- 44 H. Sax, B. Allegranzi, M. N. Chraïti, J. Boyce, E. Larson and D. Pittet, *Am. J. Infect. Control*, 2009, **37**, 827–834.
- 45 H. Sax, B. Allegranzi, I. Uçkay, E. Larson, J. Boyce and D. Pittet, *J. Hosp. Infect.*, 2007, **67**, 9–21.
- 46 A. Barton, *AORN J.*, 2009, **90**, 601–602.
- 47 J. Blanchard, *AORN J.*, 2007, **86**, 82–84.

- 48 D. Pittet, *Infect. Control Hosp. Epidemiol.*, 2000, **21**, 381–386.
- 49 S. J. Dancer, *J. Hosp. Infect.*, 2009, **73**, 378–385.
- 50 B. Allegranzi and D. Pittet, *J. Hosp. Infect.*, 2009, **73**, 305–315.
- 51 R. J. Pratt, C. Pellowe, H. P. Loveday, N. Robinson, G. W. Smith, S. Barrett, P. Davey, P. Harper, C. Loveday, C. McDougall, A. Mulhall, S. Privett, C. Smales, L. Taylor, B. Weller and M. Wilcox, *J. Hosp. Infect.*, 2001, **47**, 3–82.
- 52 W. A. Rutala and D. J. Weber, *Am. J. Infect. Control*, 2013, **41**, 2–5.
- 53 W. Picheansathian, *Int. J. Nurs. Pract.*, 2004, **10**, 3–9.
- 54 S. A. Creedon, *J. Adv. Nurs.*, 2005, **51**, 208–216.
- 55 C. R. Kokare, S. Chakraborty, A. N. Khopade and K. R. Mahadik, *Indian J. Biotechnol.*, 2009, **8**, 159–168.
- 56 R. M. Donlan, *Clin. Infect. Dis.*, 2001, **33**, 1387–1392.
- 57 M. Nemati, G. E. Jenneman and G. Voordouw, *Biotechnol. Bioeng.*, 2001, **74**, 424–434.
- 58 I. Davidova, M. S. Hicks, P. M. Fedorak and J. M. Suflita, *J. Ind. Microbiol. Biotechnol.*, 2001, **27**, 80–86.
- 59 N. B. Hallam, J. R. West, C. F. Forster and J. Simms, *Water Res.*, 2001, **35**, 4063–4071.
- 60 L. F. Melo and T. R. Bott, *Exp. Therm. Fluid Sci.*, 1997, **14**, 375–381.
- 61 R. M. Donlan and J. W. Costerton, *Clin. Microbiol. Rev.*, 2002, **15**, 167–193.
- 62 H. Gest, *Notes Rec. R. Soc. Lond.*, 2004, **58**, 187–201.
- 63 R. M. Donlan, *Emerg. Infect. Dis.*, 2002, **8**, 881–890.
- 64 T. R. Garrett, M. Bhakoo and Z. Zhang, *Prog. Nat. Sci.*, 2008, **18**, 1049–1056.
- 65 M. Hermansson, *Colloids Surfaces B Biointerfaces*, 1999, **14**, 105–119.
- 66 M. T. Madigan, J. M. Martinko, P. V. Dunlap and D. P. Clark, *Brock Biology of Microorganisms (12th Edition)*, 2008, vol. 2.
- 67 M. E. Davey, A. O. George and G. A. O. Toole, *Microbiol. Mol. Biol. Rev.*, 2000, **64**, 847–867.
- 68 M. B. Miller and B. L. Bassler, *Annu. Rev. Microbiol.*, 2001, **55**, 165–199.
- 69 C. R. Crick, S. Ismail, J. Pratten and I. P. Parkin, *Thin Solid Films*, 2011, **519**, 3722–3727.
- 70 K. Koch and W. Barthlott, *Philos. Trans. A. Math. Phys. Eng. Sci.*, 2009, **367**, 1487–1509.
- 71 I. I. Raad, X. Fang, X. M. Keutgen, Y. Jiang, R. Sherertz and R. Hachem, *Curr. Opin. Infect. Dis.*, 2008, **21**, 385–392.
- 72 K. Page, M. Wilson and I. P. Parkin, *J. Mater. Chem.*, 2009, **19**, 3819–3831.
- 73 M. L. W. Knetsch and L. H. Koole, *Polymers (Basel)*, 2011, **3**, 340–366.

- 74 D. Campoccia, L. Montanaro and C. R. Arciola, *Biomaterials*, 2013, **34**, 8533–8554.
- 75 B. S. Atiyeh, M. Costagliola, S. N. Hayek and S. A. Dibo, *Burns*, 2007, **33**, 139–148.
- 76 C. Molteni, H. K. Abicht and M. Solioz, *Appl. Environ. Microbiol.*, 2010, **76**, 4099–101.
- 77 F. Furno, K. S. Morley, B. Wong, B. L. Sharp, P. L. Arnold, S. M. Howdle, R. Bayston, P. D. Brown, P. D. Winship and H. J. Reid, *J. Antimicrob. Chemother.*, 2004, **54**, 1019–1024.
- 78 Q. Feng, J. Wu and G. Chen, *J Biomed Mater Rev*, 2000, **52**, 662–8.
- 79 D. R. Monteiro, L. F. Gorup, A. S. Takamiya, A. C. Ruvollo-Filho, E. R. De Camargo and D. B. Barbosa, *Int. J. Antimicrob. Agents*, 2009, **34**, 103–110.
- 80 Jones, Anthony C, Hitchman, Michael L, *Chemical Vapour Deposition: Precursors, Processes and Applications*, RSC Publishing, 2009.
- 81 K. L. Choy, *Prog. Mater. Sci.*, 2003, **48**, 57–170.
- 82 A. Mubarak, E. Hamzah and M. R. M. Toff, *Mater. Res.*, 2005, 42–51.
- 83 B. S. Lim, A. Rahtu and R. G. Gordon, *Nat. Mater.*, 2003, **2**, 749–754.
- 84 J. R. Creighton and P. Ho, *Chem. Vap. Depos.*, 1967, 11–13.
- 85 X. Hou and K. L. Choy, *Chem. Vap. Depos.*, 2006, **12**, 583–596.
- 86 C. Gutfinger, *Int. J. Multiph. Flow*, 1996, **22**, 807–808.
- 87 R. G. Palgrave and I. P. Parkin, *Society*, 2007, 4639–4647.
- 88 S. Basharat, C. J. Carmalt, R. Binions, R. Palgrave and I. P. Parkin, *Dalton Trans.*, 2008, **9226**, 591–595.
- 89 J. Akhtar, M. A. Malik, P. O'Brien and M. Helliwell, *J. Mater. Chem.*, 2010, **20**, 6116–6124.
- 90 T. Trindade and P. O. Brien, *Chem. Mater.*, 1997, **9**, 523–530.
- 91 C. Edusi, G. Sankar and I. P. Parkin, *Chem. Vap. Depos.*, 2012, **18**, 126–132.
- 92 D. Pugh, P. Marchand, I. P. Parkin and C. J. Carmalt, *Inorg. Chem.*, 2012, **51**, 6385–95.
- 93 C. E. Knapp, L. Pemberton, C. J. Carmalt, D. Pugh, P. F. McMillan, S. A. Barnett and D. A. Tocher, *Main Gr. Chem.*, 2010, **9**, 31–40.
- 94 D. P. Adams, T. M. Mayer, E. Chason, B. K. Kellerman and B. S. Swartzentruber, *Surf. Sci.*, 1997, **371**, 445–454.
- 95 Y. Liu, C. R. Gorla, S. Liang, N. Emanetoglu, Y. Lu, H. Shen and M. Wraback, *J. Electron. Mater.*, 2000, **29**, 69–74.
- 96 A. G. Thompson, *Mater. Lett.*, 1997, **30**, 255–263.
- 97 M. Meyyappan, L. Delzeit, A. Cassell and D. Hash, *Plasma Sources Sci. Technol.*, 2003, **12**, 205–216.

- 98 S. Fay, J. Steinhauser, S. Nicolay and C. Ballif, *Thin Solid Films*, 2010, **518**, 2961–2966.
- 99 C. Drosos and D. Vernardou, *Sol. Energy Mater. Sol. Cells*, 2015, **140**, 1–8.
- 100 B. Xia, F. Chen, S. A. Campbell, J. T. Roberts and W. L. Gladfelter, *Chem. Vap. Depos.*, 2004, **10**, 195–200.
- 101 R. Strobel and S. E. Pratsinis, *J. Mater. Chem.*, 2007, **17**, 4743.
- 102 J. Tauc, *Mater. Res. bulletin*, 1968, **3**, 37–46.
- 103 D. P. Madigan, M. T. Martinko, John M, Dunlap, Paul V, Clark, *Biology of Microorganisms*, Pearson Benjamin Cummings, 2009.
- 104 M. R. Hamblin and T. Hasan, *Photochem. Photobiol. Sci.*, 2004, **3**, 436–450.
- 105 I. Wiegand, K. Hilpert and R. E. W. Hancock, *Nat. Protoc.*, 2008, **3**, 163–175.
- 106 J. H. Jorgensen and M. J. Ferraro, *Clin. Infect. Dis.*, 2009, **49**, 1749–1755.
- 107 N. Nachar, *Tutor. Quant. Methods Psychol.*, 2008, **4**, 13–20.
- 108 J. Elguindi, X. Hao, Y. Lin, H. a Alwathnani, G. Wei and C. Rensing, *Appl. Microbiol. Biotechnol.*, 2011, **91**, 237–49.
- 109 J. O’Gorman and H. Humphreys, *J. Hosp. Infect.*, 2012, **81**, 217–223.
- 110 G. Grass, C. Rensing and M. Solioz, *Appl. Environ. Microbiol.*, 2011, **77**, 1541–1547.
- 111 J. A. Lemire, J. J. Harrison and R. J. Turner, *Nat. Rev. Microbiol.*, 2013, **11**, 371–384.
- 112 J. O’Gorman and H. Humphreys, *J. Hosp. Infect.*, 2012, **81**, 217–223.
- 113 P. J. Kuhn, *Diagnostic. Med.*, 1983.
- 114 S. A. Wilks, H. Michels and C. W. Keevil, *Int. J. Food Microbiol.*, 2005, **105**, 445–454.
- 115 T. J. Karpanen, A. L. Casey, P. a. Lambert, B. D. Cookson, P. Nightingale, L. Miruszenko and T. S. J. Elliott, *Infect. Control Hosp. Epidemiol.*, 2012, **33**, 3–9.
- 116 A. L. Casey, D. Adams, T. J. Karpanen, P. A. Lambert, B. D. Cookson, P. Nightingale, L. Miruszenko, R. Shillam, P. Christian and T. S. J. Elliott, *J. Hosp. Infect.*, 2010, **74**, 72–77.
- 117 J. O. Noyce, H. Michels and C. W. Keevil, *Appl. Environ. Microbiol.*, 2007, **73**, 2748–2750.
- 118 C. D. Salgado, K. A. Sepkowitz, J. F. John, J. R. Cantey, H. H. Attaway, K. D. Freeman, P. A. Sharpe, H. T. Michels and M. G. Schmidt, *Infect. Control Hosp. Epidemiol.*, 2013, **34**, 479–486.
- 119 M. S. V Prado, C Durán, M Crestto, A Gutierrez, P Sapiain, G Flores, H Fabres, C Tardito, in *Poster 56.044, presented at the 14th International Conference on Infectious Diseases.*

- 120 P. A. Efstathiou, *Eur. Infect. Dis.*, 2011, **5**, 125–128.
- 121 F. Marais, S. Mehtar and L. Chalkley, *J. Hosp. Infect.*, 2010, **74**, 80–82.
- 122 C. E. Santo, P. V. Morais and G. Grass, *Appl. Environ. Microbiol.*, 2010, **76**, 1341–1348.
- 123 L. Macomber and J. A. Imlay, *Proc. Natl. Acad. Sci. U. S. A.*, 2009, **106**, 8344–8349.
- 124 S. W. J. Gould, M. D. Fielder, A. F. Kelly, M. Morgan, J. Kenny and D. P. Naughton, *Ann. Microbiol.*, 2009, **59**, 151–156.
- 125 R. M. Sterritt and J. N. Lester, *Sci. Total Environ.*, 1980, **14**, 5–17.
- 126 C. E. Santo, E. W. Lam, C. G. Elowsky, D. Quaranta, D. W. Domaille, C. J. Chang and G. Grass, *Appl. Environ. Microbiol.*, 2011, **77**, 794–802.
- 127 M. Rai, A. Yadav and A. Gade, *Biotechnol. Adv.*, 2009, **27**, 76–83.
- 128 G. Ren, D. Hu, E. W. C. Cheng, M. a Vargas-Reus, P. Reip and R. P. Allaker, *Int. J. Antimicrob. Agents*, 2009, **33**, 587–590.
- 129 R. Becker, A. Devi, J. Weiß, U. Weckenmann, M. Winter, C. Kiener, H. W. Becker and R. a. Fischer, *Chem. Vap. Depos.*, 2003, **9**, 149–156.
- 130 K. K. Choi and S. W. Rhee, *Thin Solid Films*, 2001, **397**, 70–77.
- 131 S. T. Barry, *Coord. Chem. Rev.*, 2013, **257**, 3192–3201.
- 132 P. Piszczek, I. B. Szymańska, E. Talik and J. Heimann, *Chem. Vap. Depos.*, 2013, **19**, 251–259.
- 133 V. Krisyuk, L. Aloui, N. Prud'homme, S. Sysoev, F. Senocq, D. Samélor and C. Vahlas, *Electrochem. Solid-State Lett.*, 2011, **14**, 26–29.
- 134 M. Hans, A. Erbe, S. Mathews, Y. Chen, M. Solioz and F. Mücklich, *Langmuir*, 2013, **29**, 16160–16166.
- 135 G. A. Ozin, C. Arsenault and L. Cademartiri, *Mater. Today*, 2009, **12**, 46.
- 136 K. Kelly and E. Coronado, *J. Phys. Chem. B*, 2003, **107**, 668–677.
- 137 W. J. Stark, *Angew. Chemie - Int. Ed.*, 2011, **50**, 1242–1258.
- 138 S. Prabhu and E. K. Poulouse, *Int. Nano Lett.*, 2012, **2**, 32.
- 139 M. D. Rolfe, C. J. Rice, S. Lucchini, C. Pin, A. Thompson, A. D. S. Cameron, M. Alston, M. F. Stringer, R. P. Betts, J. Baranyi, M. W. Peck and J. C. D. Hinton, *J. Bacteriol.*, 2012, **194**, 686–701.
- 140 I. A. M. Swinnen, K. Bernaerts, E. J. J. Dens, A. H. Geeraerd and J. F. Van Impe, *Int. J. Food Microbiol.*, 2004, **94**, 137–159.
- 141 C. R. Crick and I. P. Parkin, *J. Mater. Chem.*, 2011, **21**, 14712.
- 142 L. L. Hench and D. E. Clark, *J. Non-Cryst. Solids*, 1978, **28**, 83–105.
- 143 D. J. Semin and K. L. Rowlen, *Anal. Chem.*, 1994, **66**, 4324–4331.
- 144 R. Ghosh, D. Basak and S. Fujihara, *J. Appl. Phys.*, 2004, **96**, 2689–2692.

- 145 M. E. Straumanis and L. S. Yu, *Acta Crystallogr. Sect. A*, 1969, **25**, 676–682.
- 146 S. Poulston, P. M. Parlett, P. Stone and M. Bowker, *Surf. Interface Anal.*, 1996, **24**, 811–820.
- 147 S. L. Warnes, V. Caves and C. W. Keevil, *Environ. Microbiol.*, 2012, **14**, 1730–1743.
- 148 S. L. Warnes and C. W. Keevil, *Appl. Environ. Microbiol.*, 2011, **77**, 6049–59.
- 149 H. T. Michels, J. O. Noyce and C. W. Keevil, *Lett. Appl. Microbiol.*, 2009, **49**, 191–195.
- 150 H. M. Yates, L. A. Brook, D. W. Sheel, I. B. Ditta, A. Steele and H. A. Foster, *Thin Solid Films*, 2008, **517**, 517–521.
- 151 G. A. Pankey and L. D. Sabath, *Clin. Infect. Dis.*, 2004, **38**, 864–870.
- 152 J. P. Ruparelia, A. K. Chatterjee, S. P. Duttagupta and S. Mukherji, *Acta Biomater.*, 2008, **4**, 707–716.
- 153 V. V. T. Padil and M. Černík, *Int. J. Nanomedicine*, 2013, **8**, 889–898.
- 154 A. Azam, A. S. Ahmed, M. Oves, M. S. Khan and A. Memic, *Int. J. Nanomedicine*, 2012, **7**, 3527–3535.
- 155 T. Minami, *MRS Bull.*, 2000, **25**, 38–44.
- 156 G. Kiriakidis and N. Katsarakis, *J. Phys. Condens. Matter*, 2004, **16**, 3757–3768.
- 157 C. G. Granqvist and A. Hultåker, *Thin Solid Films*, 2002, **411**, 1–5.
- 158 E. L. Ratcliff, J. L. Jenkins, K. Nebesny and N. R. Armstrong, *Society*, 2008, **11**, 414–420.
- 159 S. Lany and A. Zunger, *Phys. Rev. Lett.*, 2007, **98**, 045501.
- 160 H. Kim, C. M. Gilmore, A. Piqué, J. S. Horwitz, H. Mattoussi, H. Murata, Z. H. Kafafi and D. B. Chrisey, *J. Appl. Phys.*, 1999, **86**, 6451.
- 161 P. P. Edwards, A. Porch, M. O. Jones, D. V Morgan and R. M. Perks, *Dalton Trans.*, 2004, **19**, 2995–3002.
- 162 W. Beyer, J. Hüpkes and H. Stiebig, *Thin Solid Films*, 2007, **516**, 147–154.
- 163 T. J. Coutts, D. L. Young and X. Li, *MRS Bull.*, 2000, **25**, 58–65.
- 164 A. Stadler, *Materials (Basel)*, 2012, **5**, 661–683.
- 165 B. J. Ingram, G. B. Gonzalez, D. R. Kammler, M. I. Bertoni and T. O. Mason, in *Journal of Electroceramics*, 2004, **13**, 167–175.
- 166 P. Erhart, A. Klein, R. G. Egdell and K. Albe, *Phys. Rev. B*, 2007, **75**, 153205.
- 167 P. D. C. King, T. D. Veal, F. Fuchs, C. Y. Wang, D. J. Payne, A. Bourlange, H. Zhang, G. R. Bell, V. Cimalla, O. Ambacher, R. G. Egdell, F. Bechstedt and C. F. McConville, *Phys. Rev. B - Condens. Matter Mater. Phys.*, 2009, **79**, 205211.
- 168 S. Basharat, C. J. Carmalt, S. a Barnett, D. a Tocher and H. O. Davies, *Inorg.*

- Chem.*, 2007, **46**, 9473–80.
- 169 S. Basharat, W. Betchley, C. J. Carmalt, S. Barnett, D. A. Tocher and H. O. Davies, *Organometallics*, 2007, **26**, 403–407.
- 170 L. G. Bloor, C. J. Carmalt and D. Pugh, *Coord. Chem. Rev.*, 2011, **255**, 1293–1318.
- 171 M. Ogita, S. Yuasa, K. Kobayashi, Y. Yamada, Y. Nakanishi and Y. Hatanaka, in *Applied Surface Science*, 2003, **212**, 397–401.
- 172 M. Fleischer and H. Meixner, *Sensors Actuators B Chem.*, 1991, **4**, 437–441.
- 173 H. S. Oon and K. Y. Cheong, *Mater. Sci. Semicond. Process.*, 2013, **16**, 1217–1231.
- 174 F. Minandri, C. Bonchi, E. Frangipani, F. Imperi and P. Visca, *Future Microbiol.*, 2014, **9**, 379–97.
- 175 O. Olakanmi, B. E. Britigan and L. S. Schlesinger, *Infect. Immun.*, 2000, **68**, 5619–5627.
- 176 K. O. Konhauser, A. Kappler and E. E. Roden, *Elements*, 2011, **7**, 89–93.
- 177 J. B. Neilands, *J. Biol. Chem.*, 1995, **270**, 26723–26726.
- 178 C. Wandersman and P. Delepelaire, *Annu. Rev. Microbiol.*, 2004, **58**, 611–647.
- 179 H. Fones and G. M. Preston, *FEMS Microbiol. Rev.*, 2013, **37**, 495–519.
- 180 C. R. Chitambar, *Int. J. Environ. Res. Public Health*, 2010, **7**, 2337–2361.
- 181 S. C. King, R. J. Reiman and L. R. Prosnitz, *J. Clin. Oncol.*, 1994, **12**, 306–311.
- 182 J. A. van Amsterdam, J. C. Kluin-Nelemans, B. L. van Eck-Smit and E. K. Pauwels, *Ann. Hematol.*, 1996, **72**, 202–207.
- 183 P. Collery, B. Keppler, C. Madoulet and B. Desoize, *Crit. Rev. Oncol. Hematol.*, 2002, **42**, 283–296.
- 184 B. J. Foster, K. Clagett-Carr, D. Hoth and B. Leyland-Jones, *Cancer Treat. Rep.*, 1986, **70**, 11, 1311–1319
- 185 J. K. Weick, R. L. Stephens, L. H. Baker and S. E. Jones, *Cancer Treat. Rep.*, 1983, **67**, 823–825.
- 186 J. Keller, A. Bartolucci, J. T. Carpenter and J. Feagler, *Cancer Treat. Rep.*, 1986, **70**, 10, 1221–1223.
- 187 R. P. Warrell, C. J. Coonley, D. J. Straus and C. W. Young, *Cancer*, 1983, **51**, 1982–1987.
- 188 C. E. Arnold, A. Bordin, S. D. Lawhon, M. C. Libal, L. R. Bernstein and N. D. Cohen, *Vet. Microbiol.*, 2012, **155**, 389–394.
- 189 M. Coleman, K. Kuskie, M. Liu, K. Chaffin, M. Libal, S. Giguère, L. Bernstein and N. Cohen, *Vet. Microbiol.*, 2010, **146**, 175–178.
- 190 C. R. Chitambar, *Future Med. Chem.*, 2012, **4**, 1257–1272.

- 191 C. R. Chitambar, D. P. Purpi, J. Woodliff, M. Yang and J. P. Wereley, *J. Pharmacol. Exp. Ther.*, 2007, **322**, 1228–1236.
- 192 M. Frezza, C. N. Verani, D. Chen and Q. P. Dou, *Lett. Drug Des. Discov.*, 2007, **4**, 311–317.
- 193 S. P. Valappil, D. Ready, E. A. Abou Neel, D. M. Pickup, L. A. O'Dell, W. Chrzanowski, J. Pratten, R. J. Newport, M. E. Smith, M. Wilson and J. C. Knowles, *Acta Biomater.*, 2009, **5**, 1198–1210.
- 194 S. P. Valappil, D. Ready, E. A. Abou Neel, D. M. Pickup, W. Chrzanowski, L. A. O'Dell, R. J. Newport, M. E. Smith, M. Wilson and J. C. Knowles, *Adv. Funct. Mater.*, 2008, **18**, 732–741.
- 195 S. Y. Lee, N. Mettlach, N. Nguyen, Y. M. Sun and J. M. White, *Appl. Surf. Sci.*, 2003, **206**, 102–109.
- 196 A. Chen, H. Long, X. Li, Y. Li, G. Yang and P. Lu, *Vacuum*, 2009, **83**, 927–930.
- 197 K. Akimoto, S. Ishizuka, M. Yanagita, Y. Nawa, G. K. Paul and T. Sakurai, *Sol. Energy*, 2006, **80**, 715–722.
- 198 O. M. Berengue, A. D. Rodrigues, C. J. Dalmaschio, A. J. C. Lanfredi, E. R. Leite and A. J. Chiquito, *J. Phys. D. Appl. Phys.*, 2010, **43**, 045401.
- 199 D. P. Joseph, P. Renugambal, M. Saravanan, S. P. Raja and C. Venkateswaran, *Thin Solid Films*, 2009, **517**, 6129–6136.
- 200 C. G. Granqvist, *Sol. Energy Mater. Sol. Cells*, 2007, **91**, 1529–1598.
- 201 N. Noor and I. P. Parkin, *J. Mater. Chem. C*, 2013, **1**, 984–996.
- 202 D. S. Bhachu, G. Sankar and I. P. Parkin, *Chem. Mater.*, 2012, **24**, 4704–4710.
- 203 N. Noor and I. P. Parkin, *Thin Solid Films*, 2013, **532**, 26–30.
- 204 S. Lany, A. Zakutayev, T. O. Mason, J. F. Wager, K. R. Poeppelmeier, J. D. Perkins, J. J. Berry, D. S. Ginley and A. Zunger, *Phys. Rev. Lett.*, 2012, **108**, 016802.
- 205 H. Agura, A. Suzuki, T. Matsushita, T. Aoki and M. Okuda, in *Thin Solid Films*, 2003, **445**, 263–267.
- 206 V. Musat, B. Teixeira, E. Fortunato, R. C. . Monteiro and P. Vilarinho, *Surf. Coatings Technol.*, 2004, 180–181, 659–662.
- 207 K. Matsubara, P. Fons, K. Iwata, A. Yamada, K. Sakurai, H. Tampo and S. Niki, in *Thin Solid Films*, 2003, **431**, 369–372.
- 208 S. Ripa and R. Ripa, *Minerva Med.*, 1995, **86**, 315–318.
- 209 J. Pasquet, Y. Chevalier, J. Pelletier, E. Couval, D. Bouvier and M.-A. Bolzinger, *Colloids Surfaces A Physicochem. Eng. Asp.*, 2014, **457**, 263–274.
- 210 W. Jiang, H. Mashayekhi and B. Xing, *Environ. Pollut.*, 2009, **157**, 1619–1625.
- 211 R. Brayner, R. Ferrari-Iliou, N. Brivois, S. Djediat, M. F. Benedetti and F.

- Fiévet, *Nano Lett.*, 2006, **6**, 866–870.
- 212 L. C. Ann, S. Mahmud, S. K. M. Bakhori, A. Sirelkhatim, D. Mohamad, H. Hasan, A. Seeni and R. A. Rahman, *Ceram. Int.*, 2014, **40**, 2993–3001.
- 213 S. D. Gittard, J. R. Perfect, N. A. Monteiro-Riviere, W. Wei, C. Jin and R. J. Narayan, *Appl. Surf. Sci.*, 2009, **255**, 5806–5811.
- 214 P. Carvalho, P. Sampaio, S. Azevedo, C. Vaz, J. P. Espinós, V. Teixeira and J. O. Carneiro, *Appl. Surf. Sci.*, 2014, **307**, 548–557.
- 215 A. G. Cuevas, K. Balangcod, T. Balangcod and A. Jasmin, *Procedia Eng.*, 2013, **68**, 537–543.
- 216 E. Ozkan, F. T. Ozkan, E. Allan and I. P. Parkin, *RSC Adv.*, 2015, **5**, 8806–8813.
- 217 M.-L. Kääriäinen, C. K. Weiss, S. Ritz, S. Pütz, D. C. Cameron, V. Mailänder and K. Landfester, *Appl. Surf. Sci.*, 2013, **287**, 375–380.
- 218 L. C. Ann, S. Mahmud, S. K. M. Bakhori, A. Sirelkhatim, D. Mohamad, H. Hasan, A. Seeni and R. A. Rahman, *Appl. Surf. Sci.*, 2014, **292**, 405–412.
- 219 M. R. Waugh, G. Hyett and I. P. Parkin, *Chem. Vap. Depos.*, 2008, **14**, 369–372.
- 220 S. Fay and A. Shah, *Transparent Conduct. Zinc Oxide*, 2008, **104**, 235–302.
- 221 Y. Natsume and H. Sakata, *Thin Solid Films*, 2000, **372**, 30–36.
- 222 K. Ellmer, *J. Phys. D. Appl. Phys.*, 2000, **33**, 17–32.
- 223 Y. H. Ni, X. W. Wei, X. Ma and J. M. Hong, *J. Cryst. Growth*, 2005, **283**, 48–56.
- 224 X. M. Sun, X. Chen, Z. X. Deng and Y. D. Li, *Mater. Chem. Phys.*, 2003, **78**, 99–104.
- 225 K. Kaye, D. Turner, D. McKenn, A. Cackett and G. Hyett, in *Physics Procedia*, 2013, **46**, 21–26.
- 226 H. J. Zhai, W. H. Wu, F. Lu, H. S. Wang and C. Wang, *Mater. Chem. Phys.*, 2008, **112**, 1024–1028.
- 227 A. R. Babar, P. R. Deshamukh, R. J. Deokate, D. Haranath, C. H. Bhosale and K. Y. Rajpure, *J. Phys. D. Appl. Phys.*, 2008, **41**, 135404.
- 228 G. Walters and I. P. Parkin, *Appl. Surf. Sci.*, 2009, **255**, 6555–6560.
- 229 M. G. Nolan, J. A. Hamilton, S. Obrien, G. Bruno, L. Pereira, E. Fortunato, R. Martins, I. M. Povey and M. E. Pemble, *J. Photochem. Photobiol. A Chem.*, 2011, **219**, 10–15.
- 230 A. Douayar, R. Diaz, F. Cherkaoui El Moursli, G. Schmerber, A. Dinia and M. Abd-Lefdil, *Eur. Phys. J. Appl. Phys.*, 2011, **53**, 20501.
- 231 S. Zhao, Y. Bai, J. Chen, A. Bai and W. Gao, 2014, **19**, 68–71.
- 232 V. Srikant and D. R. Clarke, *J. Appl. Phys.*, 1998, **83**, 5447.
- 233 G. K. Mani and J. B. B. Rayappan, *J. Alloys Compd.*, 2014, **582**, 414–419.

- 234 M. Y. Ghotbi, N. Bagheri and S. K. Sadrnezhad, *Adv. Powder Technol.*, 2012, **23**, 279–283.
- 235 C. X. Xu, X. W. Sun, X. H. Zhang, L. Ke and S. J. Chua, *Nanotechnology*, 2004, **15**, 856–861.
- 236 M. P. Muller, C. MacDougall and M. Lim, *J. Hosp. Infect.*, 2015, **92**, 7–13.